2015

Study of transport properties and defect density profile in nanocrystalline silicon germanium devices

Siva Konduri
Iowa State University

Study of transport properties and defect density profile in nanocrystalline silicon germanium devices

by

Siva Konduri

A thesis submitted to the graduate faculty

in partial fulfillment of the requirements for the degree of

DOCTOR OF PHILOSOPHY

Major: Electrical Engineering

Program of Study Committee:
Vikram Dalal, Major Professor
Rana Biswas
Sumit Chaudhary
Joseph Shinar
Mani Mina

Iowa State University

Ames, Iowa

2015

TABLE OF CONTENTS

LIST OF FIGURES

LIST OF TABLES

ACKNOWLEDGEMENTS

I would like to thank my major professor Dr. Vikram Dalal for his support and faith in me for the last five years. It was his encouragement and inspiration which drive me in tough times. He was always there to help in any kind of situation. It was great honor to work under his guidance. I would like to extend my thanks to committee members Dr. Rana Biswas, Dr. Sumit Chaudhary, Dr. Joseph Shinar and Dr. Mani Mina for their efforts and contributions.

I sincerely thank Max Noack for various discussions and helpful insight into various experiments. I would like to thank Kequin Han and Wai Leung for their help. I also thank Dr. Nayan Chakravarty, Dr. Sambit Pattnaik and Dr. Ashutosh Shyam for training me on the reactor. I extend my thanks to Dr. John Carr for helping me with CF measurements. I would like to acknowledge the help of Dr. Shantan Kajjam, Dr. Dipak Paramanik and Watson Mulder for helping me in fabrication. Special thanks to Mehran Samiee and Pranav Joshi for constant support and help.

I would like to thank Balaji, Ranjit, Hisham, Liang, Andrew[2], Spencer, Preston, Moniem, Tanvir all the MRC former and current graduate & undergraduate students who have always been helpful. I would like to take this opportunity to express my thanks again to those who helped me with various aspects of conducting research and the writing of this thesis.

I am thankful to Sudani, Prasad, Rakesh, Reddy, Viksit, Neelam, Ardhendu, Priyanka, Niranjana, Priyam, JP and all my other friends in Ames for their support and companionship and wish them all success in their life. Last, but not the least, it is the moral support, motivation and encouragement from my lovely wife and the affection of my parents and in-laws that made it possible to reach this stage in my life.

ABSTRACT

Nanocrystalline Silicon-Germanium (nc-SiGe:H) is a useful material for photovoltaic devices and photo-detectors. Its bandgap can be tuned between Si (~1.1 eV) and Ge (~0.7 eV) by changing the alloy composition during growth. The material exhibits a good absorption extending to the infrared region even with thin layers. However previous work has shown that devices with higher Ge content have poor device performance. Also, very little work has been done previously to measure and understand the defect spectrum of nanocrystalline (Si,Ge). Defects control recombination, and hence, the performance of solar cell devices.

This work deals with studying the fundamental device physics of nc-SiGe:H including defect density, lifetime and mobility and their relationship with impurities, grain size and Hydrogen bonding. Capacitance-Frequency measurements at different temperatures are used to estimate the trap density profile within the bandgap of nc-SiGe:H.

We also study device performance and how to maintain uniform crystallinity in intrinsic layers of devices so as to obtain the best device performance. We show that one can use hydrogen grading or power grading to produce films with uniform crystallinity.

We will report on a systematic study of the varying Germanium content in nc-SiGe:H the relationship between Ge content and transport properties. It is found that upon adding Ge to Si during growth, the intrinsic layer changes from n-type to p-type. This can be reversed back by using ppm levels of phosphorus doping, and devices of reasonable quality can then be obtained. Measurement of defect densities showed that adding ppm levels of phosphine reduced the midgap defect densities.

CHAPTER 1. INTRODUCTION

1.1 Solar Energy

Solar energy is becoming an important green energy resource as we rely less on fossil fuels and turn to renewable energy sources for our daily power needs. Other green energy resources like wind and tidal powers are highly location dependent. In contrast, solar energy is widely dispersed and can be harvested globally using many different technologies. Photovoltaic (PV) energy conversion is a technology for converting solar energy directly into electricity. It relies on using p-n junctions in semiconducting materials. The semiconducting material absorbs photons and converts them into electrons and holes, and the junction separates the carriers, producing a voltage and a current. The main challenge is to get efficient energy conversion while keeping the cost low. The advancement in technology and high scale manufacturing have helped in lowering the cost of photovoltaics, but the cost still need to be reduced to make solar-electricity comparable in cost to fossil fuel generated electricity. It is useful to note that the amount of solar energy incident on the earth every year is equivalent to a continuous insolation of ~69000 Terawatts. The power equivalent of annual global energy consumption is only around 20 Terawatts. Thus, solar energy has an excellent potential to fulfill all of the human energy needs with a clean environment friendly energy source. In the last decade, photovoltaic global capacity increased exponentially and reached 139 GW in 2013 (Figure 1.1). Solar industry is one of the fastest growing industries globally and attracting researchers and students all over the world.

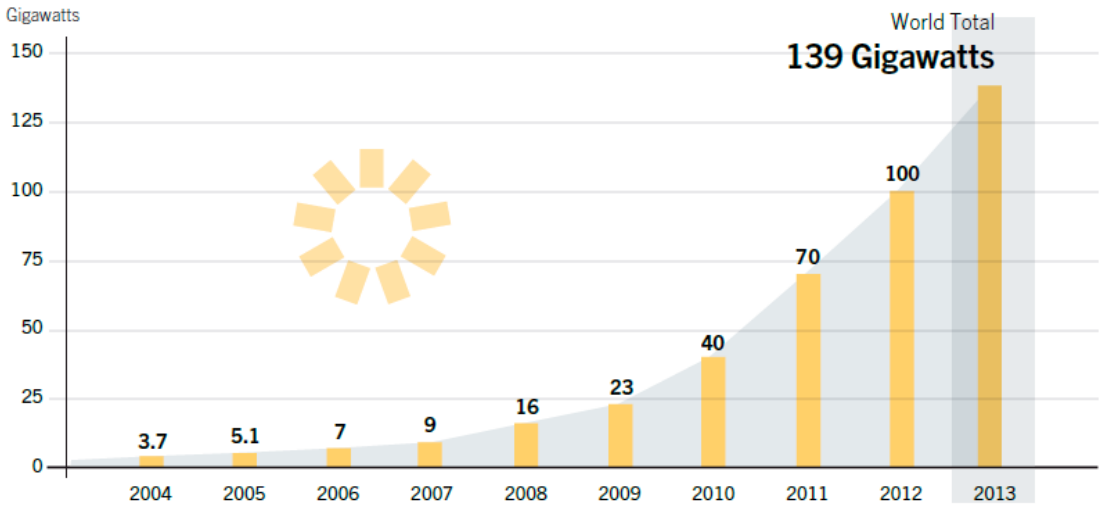

Figure 1.1 Solar photovoltaic global capacity in the last decade [1]

1.2 Thin Film Technologies

A thin film solar cell is made by depositing thin layers of photovoltaic material on a substrate and the active layer thickness varies from hundreds of nm to few µm [2]. As it is cheaper to make these cells compared to conventional crystalline silicon solar cells, they are acquiring a significant market share in renewable energy. The main advantages of thin film solar cells are lower material cost, cheaper processing techniques, easier fabrication and high volume manufacturing. Thin film technologies which are widely used are alloys of amorphous and nanocrystalline Silicon, Copper Indium Gallium Selenide and Cadmium Telluride. Some of the newer technologies are organic photovoltaics and perovksites. Different forms of Silicon based on the material phase are schematically shown in Figure 1.2.

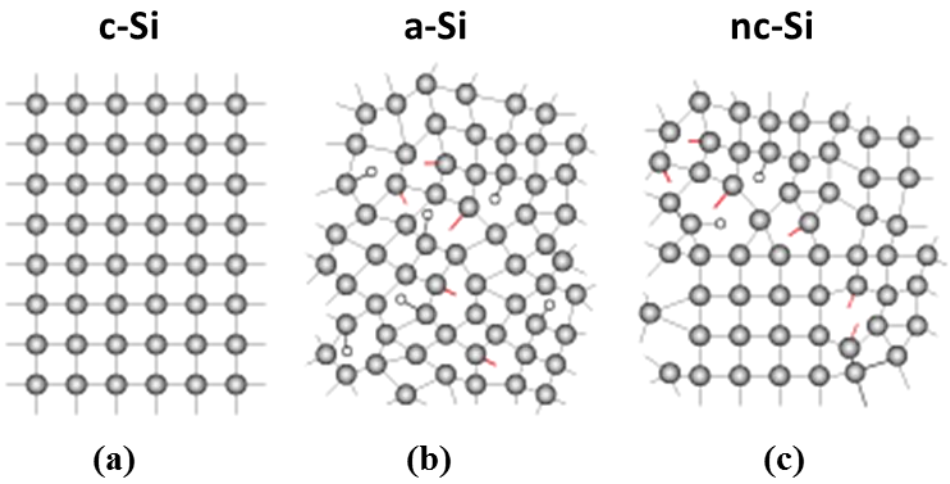

Figure 1.2 Schematic illustration of different forms of Silicon [3]

1.2.1 Amorphous Silicon Alloys

Crystalline silicon (c-Si) is the most widely used material in silicon solar cells because of its relative high efficiency and the prevalence of the Si industry. Amorphous Si (a-Si) is the next widely used solar cell technology, due to its easy production process (roll-to-roll deposition) and ease of deposition. There are various alloys of a-Si such as a-SiC, a-SiGe, and a-SiN. Amorphous films have very little crystalline order in the structure and generally highly defective because of broken Si-Si bonds which introduce defects within the bandgap. However, passivating this material with H results in many of the broken Si bonds becoming covalently bonded with H, resulting in a reduction in defect density by many orders of magnitude [4]. Therefore, a-Si is often referred as a-Si:H, the 'H' indicating its hydrogenated. The material offers a variety of advantages, such as a bandgap around 1.7eV which is not too far from the bandgap where maximum solar energy efficiencies are expected, and also a high absorption coefficient because of the amorphous nature of the material [5]. The material can also be doped n and p type. While H helps in reducing the defect density, the defect density is still high

(~10^{15}/cm3) and the material has a low mobility (≤1 cm^2/V-s). The combination of high defect density and low mobility leads to a small minority carrier lifetime (<1 microsecond) and a small minority carrier mobility-lifetime product (≤ 4 x 10^{-8} cm^2/V). The minority carrier diffusion lengths are very small ~0.3 micrometer. Hence, the device works on a principle of drift based carrier transport [6]. The main drawback of a-Si is a relatively low solar-conversion efficiency, of the order of ~10%. Another major problem is instability under light soaking (Staebler-Wronski effect). The performance of a-Si solar cells degrades between 10 - 20% in efficiency upon prolonged exposure to sunlight [7]. Chemical annealing by Helium can lower the light degradation in amorphous solar cells [8]. These problems have prevented widespread application of this technology, and the technology is slowly becoming obsolete, except for use in tandem cells [9].

1.2.2 Nanocrystalline Silicon Alloys

Nanocrystalline silicon (nc-Si) is also a promising material with fewer number of defects compared to a-Si solar cells [11]. It consists of small grains (10-20 nm) surrounded by amorphous tissue. Nanocrystalline name comes from the nano scale grain size, though in the literature many people refer to it as microcrystalline. Generally, in the standard Si technology field, microcrystalline Si term is reserved for polycrystalline materials with larger grains (μm). Hydrogen bonds play a vital role in passivating dangling bonds in nano Si and a-Si tissue ensures that the carriers are moving from one grain to another without recombining. The grain boundaries have to be well passivated with a-Si in order to achieve good transport properties and high efficiencies [12]. The absorption coefficient of nc-Si is higher than c-Si at higher energies, as shown in Figure 1.3.

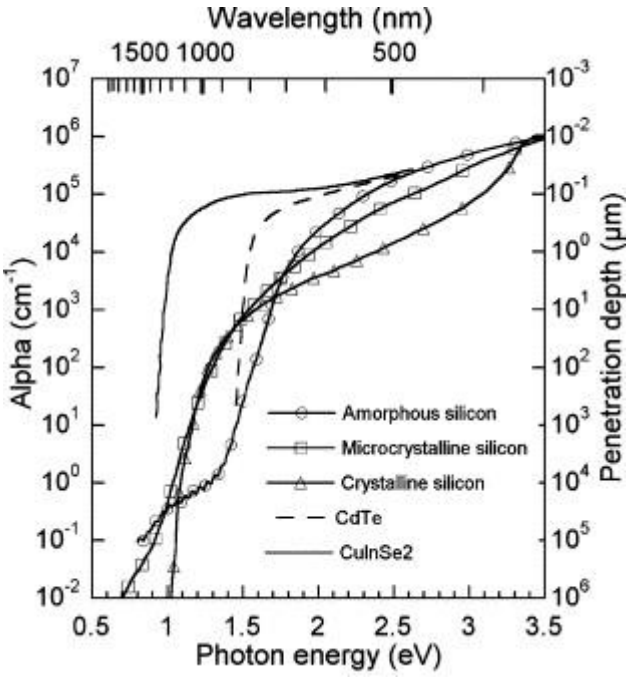

Figure 1.3 Absorption spectra for various thin-film materials used in solar cells [10]

The growth of nanocrystalline material is mainly dependent on incubation layer and nucleation sites. Incubation layer is amorphous material and crystallites growing in conical fashion from the nucleation sites as shown in Figure 1.4 [13]. Initial nucleation depends on Hydrogen dilution, defined as the ratio of Hydrogen gas flow rate to Silane gas flow rate. As the nucleation site formation is governed by the dilution of the gas, more nucleation sites can be formed with higher dilution [14]. This nucleation process decides the crystallite sites for the growth and material quality and it will be explained further in the next chapter.

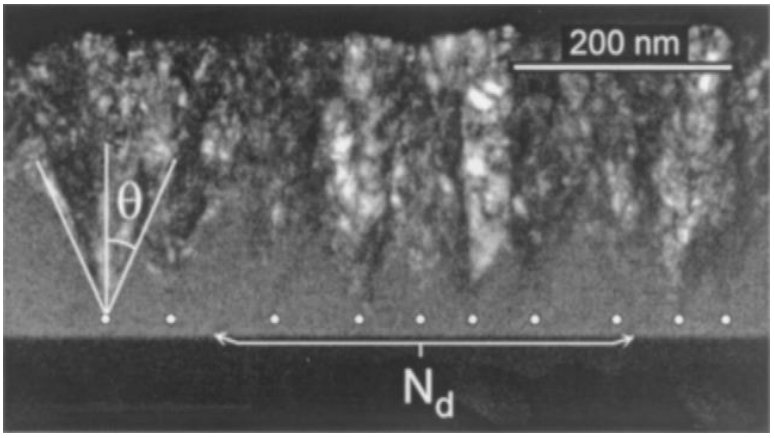

Figure 1.4 TEM image of growth of nc-Si:H showing conical growth [13]

Nanocrystalline Silicon Germanium alloys are also promising materials because of the ability to tune the bandgap which is useful in many microelectronic devices. As the Nanocrystalline Silicon Germanium is the heart of this thesis it will be discussed in much more detail in the subsequent chapters.

1.2.3 Emerging Technologies

Organic semiconductors photovoltaic devices (OPV devices) are light and flexible, employing simple processing techniques such as spin coating, roll to roll fabrication, spray coating and inkjet printing [15-20]. The main advantage of OPV is the tailoring capability of organic polymers. By changing certain elements and side groups in the organic polymer, it is possible to tune the fundamental properties such as band gap, electron density, electron affinity and ionization potential [21]. Two major problems for organic solar cells are the low efficiency (~9% maximum) and the lack of stability under illumination and under environmental exposure [22-27].

A new material which has recently emerged are a class of hybrid organic-inorganic materials called perovskites [28-33]. This material field is witnessing a high growth in the last

two years, with high conversion efficiencies ~19% having been reported [34]. The Investment risk with maturity of different solar cell technologies is shown in Figure 1.5.

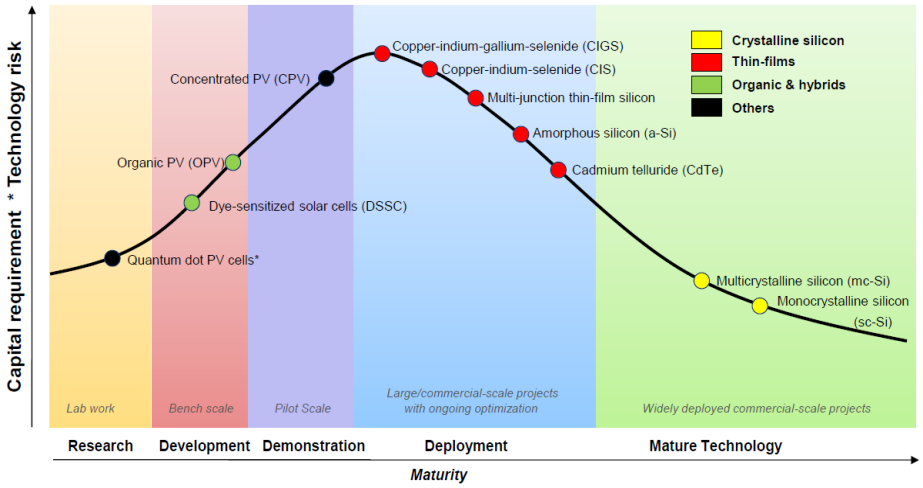

Figure 1.5 Investment risk vs. maturity for different solar cell technologies [35]

1.3 Structure of the Thesis

The main objective of this work is to understand the fundamental properties of nc-SiGe and study the relationship between the material and transport properties. Chapter 1 gives the introduction to solar energy and briefly discuss the thin film science and technology. Chapter 2 discusses the previous work on nc-Si defects and nc-SiGe devices. Chapter 2 also details the challenging problems from previous work in both the fields and how the present work advanced the science by answering these questions. Discussion of various experimental techniques, material growth, device fabrication, material and device measurements are documented in Chapter 3. Chapter 4 includes results from nc-Si, nc-SiGe films and devices. The main focus is on device properties of nc-SiGe and defect metrology in both the devices. Fundamental defects in Perovskite based solar cells also reported as an appendix. Finally, the work is summarized in Chapter 5 followed by ideas for future work.

CHAPTER 2. LITERATURE SURVEY

The review of the previous work done by various research groups in the area of nc-Si and its defect metrology are discussed in this chapter. As nc-SiGe is the main material studied in this work, literature on nc-SiGe research is also reviewed. The challenges encountered by other research groups to fabricate high Ge content nc-SiGe devices is presented and thus it laid pathway to the work presented in this thesis.

2.1 Nanocrystalline Silicon

Thin film technologies became popular over time over crystalline photovoltaics because of the potential for cost effective fabrication. In thin film technology nc-Si is a propitious material for semiconductor applications such as sensors [36, 37], solar cells [38, 39] and thin film transistors [40, 41]. Nanocrystalline silicon combines the advantages of large area deposition with improved stability under light illumination and passivated grain boundaries. In 1968, Veprek and Marecek described the deposition of nc-Si:H using chemical transport method [42]. Because of the inherent n-type nature due to oxygen contamination [43] and low deposition rates of 1 Å/sec [44], it didn't gain the attention for solar applications. IMT Neuchatel's group was one of the first groups to fabricate better quality nc-Si by counter doping with ppm levels of Diborane and demonstrated a solar cell with an efficiency of 7.7% [45-47].

2.1.1 Growth Mechanism

The growth of nc-Si:H depends on two parameters that are nucleating density and heterophase thickness density. Heterophase means the mixed phase material consisting of amorphous layer with crystallites growing in conical fashion and inverse of nucleating density

is referred to the mean distance between two nuclei from which crystallites starts growing [13]. The crystalline growth starts at nucleation centers and continues to grow into columnar manner. The space between these crystalline grains is filled with amorphous silicon which passivate the grain boundaries. This crystalline vs. amorphous volume fractions is an important factor for transport properties. In order to achieve better solar cell performance the material should be near the transition to the amorphous growth regime [48]. The change in microstructure of nc-Si:H as a function of crystalline volume fraction is shown in Figure 2.1.

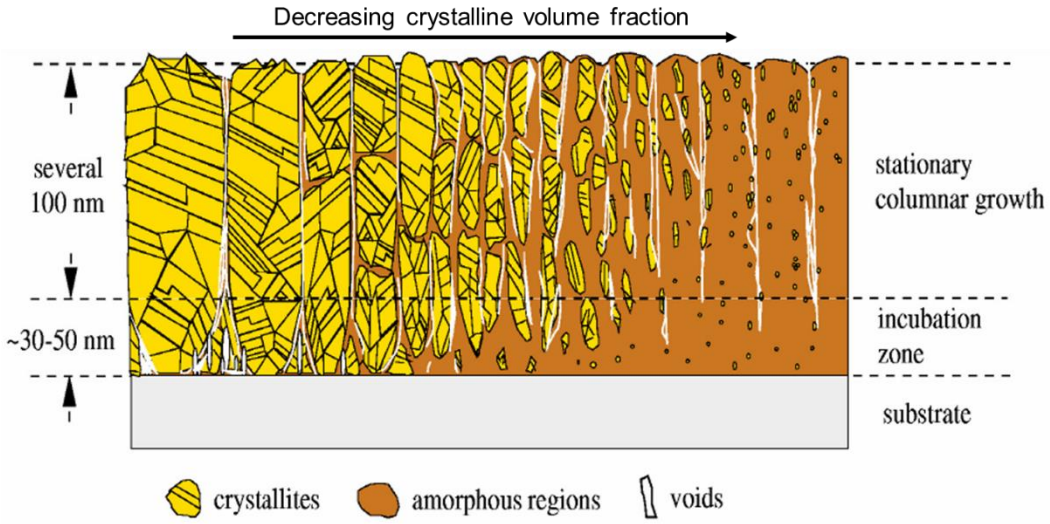

Figure 2.1 The microstructure of nc-Si:H at different crystalline volume fractions [13]

The growth kinetics of ncSi:H depends on type of fabrication and the substrate. The primary focus in this work involves growth using VHF-PECVD, so the growth mechanism of nc-Si:H using VHF-PECVD system is discussed here. The primary reaction of the growth process starts with the dissociation of SiH_4 and H_2 molecule with energetic electrons produced from the glow discharge of the plasma [49]. Figure 2.2 shows the dissociation process of H_2 and SiH_4 plasma to form different chemical species. Mai et. al suggested that formation of ncSi:H film depends heavily on SiH_3 precursor, atomic hydrogen which plays a vital role on

the surface of the forming film substrate temperature and power of the ions which are interacting with the film surface [50].

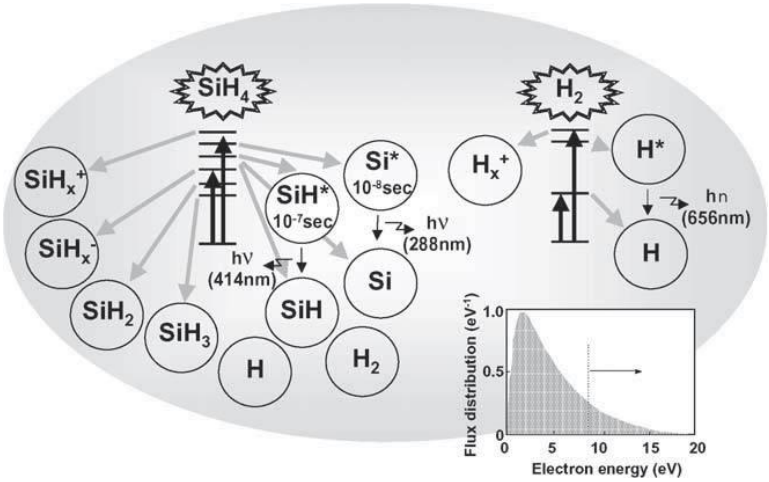

Figure 2.2 Schematic concept for the dissociation processes of SiH4 and H2 molecules in the plasma [49]

There are various models which explains the growth mechanism of ncSi:H material in a PECVD environment, such as surface diffusion model [44], etching model [51] and chemical annealing model [52].

Matsuda et. al proposed surface diffusion model [44]. The model describes the increase in crystallinity with increasing dilution ratio and temperature assuming that the surface diffusion length of the precursors across the Hydrogen covered surface increase with temperature. It further explains that the local heating caused by two Hydrogen atoms bond with each other to produce more stable molecule helps SiH_3 radical to diffuse on the film surface to get adsorbed on the substrate. Local heating process in a surface diffusion model is shown in Figure 2.3. The nucleation is started by systematic breaking of SiH_3 radical on Hydrogen covered surface and nucleation will be followed by epitaxial growth. Dalal proposed that the excess Hydrogen atoms are mainly abstracted by incoming plasma ions and also will assist in breaking Si-H bond from two adjacent SiH_3 radicals [53].

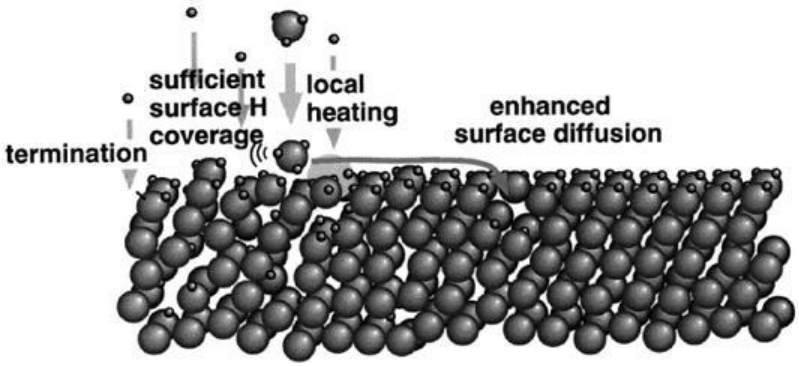

Figure 2.3 Surface diffusion model for the growth of ncSi:H material [54]

The etching model was proposed by Tsai et. al [51]. This model claims to explain the decrease in growth rate by increase in Hydrogen dilution. The atomic Hydrogen impinging on the surface etch away the weak silicon bonds and reduce SiH_3 flux density depicted in Figure 2.4. Consequently, Si* intensity reduces which is a measure of growth rate.

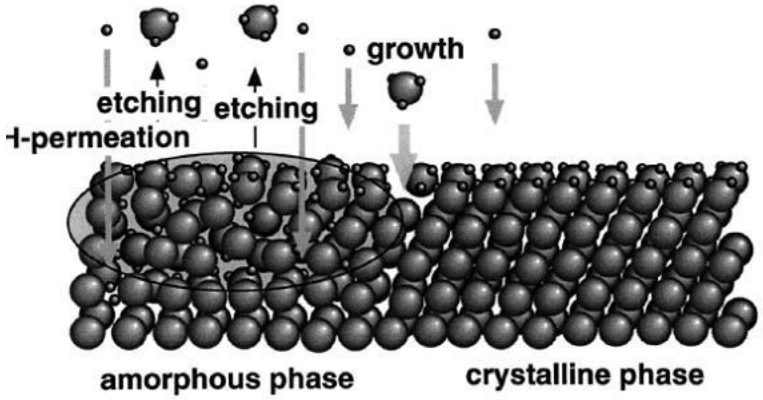

Figure 2.4 Etching model for the growth of ncSi:H material [54]

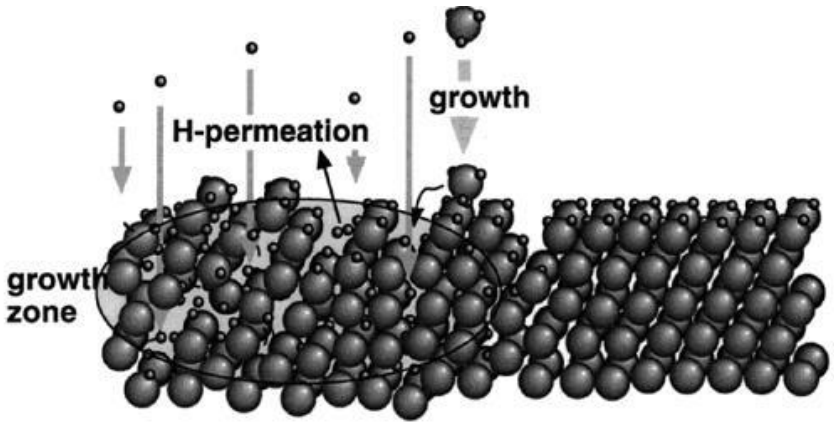

Figure 2.5 Chemical anneal model for the growth of ncSi:H material [54]

Nakamura et. al proposed the chemical annealing model [52]. It is also referred to as layer by layer technique. It's observed that in layer by layer growth followed by annealing with hydrogen the layers will be free of dangling bonds and produce better quality films. Figure 2.5 shows the chemical anneal technique where impinging H atom penetrates deep inside the layer breaking the weaker Si-Si bonds and promoting crystal formation.

2.1.2 Material Properties

Charge transport in nc-Si is strongly influenced by its heterogeneous microstructure composed of crystalline grains and amorphous tissue. The grain boundaries are rich in hydrogen content, shown in molecular dynamic simulations done by Biswas [55-57]. A model developed by Kocka et. al. explains that the conical growth of small crystallites from nucleation sites will eventually coalesce and form grain boundaries. These grain boundaries or grain aggregates results in anisotropy of transport [58]. Figure 2.6 shows the significant increase in defect density due to the collision of two cones forming larger grain boundaries. These large grain boundaries creates a barrier for band like transport and also form recombination centers. Hence, it is very important to control the growth parameters such that to reduce the grain boundaries and not turning into amorphous material.

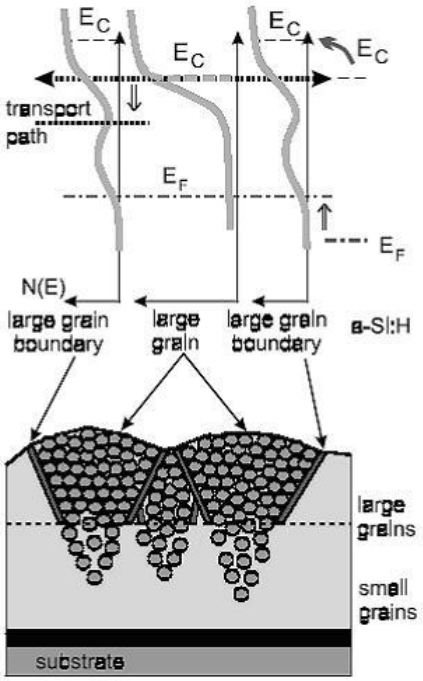

Figure 2.6 Schematic diagram of ncSi:H material with density of states [58]

As discussed earlier, the structure of nc-Si:H solar cell starts with nucleation and continues to grow into columnar manner. This may lead to more crystalline nature as the thickness increases, thus forming larger grain boundaries. There are various methods to control the crystallinity during the growth. Crystallinity mainly defined by the Hydrogen dilution, RF power and initial nucleation. The nature of the material during the growth can be modified using one of those parameters.

Hydrogen Profile

Hydrogen profile technique reduces the formation of large grain boundaries by controlling the crystallinity in ncSi:H solar cells. Figure 2.7a shows the material phase with thickness and Hydrogen dilution. Yan et. al and Gu et. al demonstrated that by gradually changing the Hydrogen dilution as a function of thickness, crystallite evolution can be

restrained [59, 60]. Figure 2.7b shows the depth profile with constant dilution and profiled dilution. Crystallinity is controlled around 60% in case of Hydrogen profile.

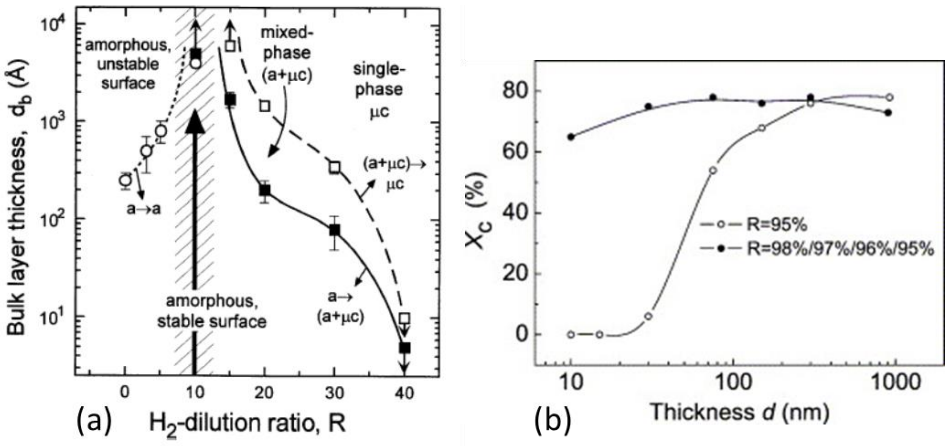

Figure 2.7 (a) Material phase diagram [13] and (b) Depth profile with crystallinity in nc-Si:H films [60]

Power Grading

Han et. al. showed successfully that by grading the power across the thickness crystallinity can be controlled in ncSi:H film [61]. Films become more crystalline with increasing in power, so the crystallinity can be reduced by decreasing the power (Figure 2.8a). This method also helps in reducing ion-bombardment then by improving the quality of the film. Figure 2.8b shows the enhancement in the device performance with power grading.

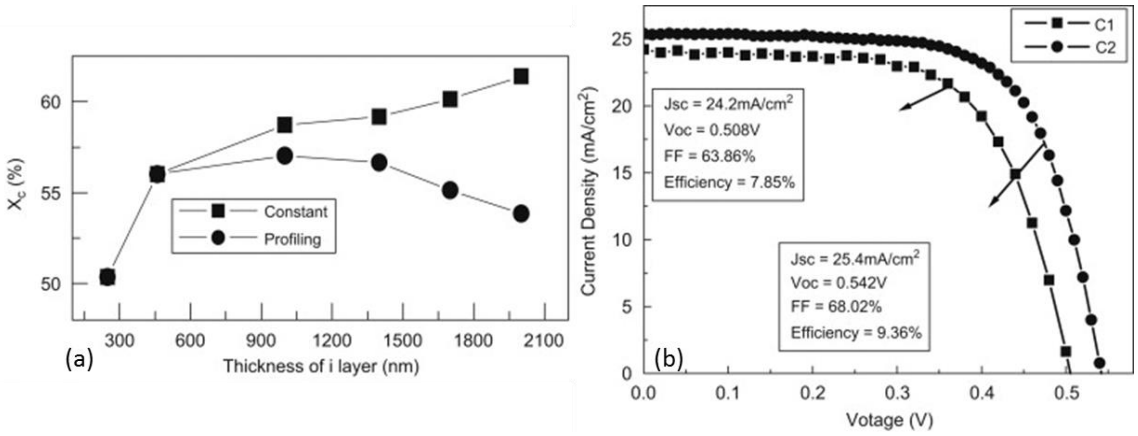

Figure 2.8 (a) Crystallinity with thickness of the film, (b) Enhancement in the device performance of cell with power grading technique [61]

Superlattice Design

Dalal and Madhavan et. al. proposed that by using thin aSi:H film to inhibit the growth of ncSi:H film should help to prevent the large grain boundary formation. The principle behind the superlattice structure is to fabricate layer by layer structure where 5-10 nm of a-Si:H layer is grown after every 50-100 nm of ncSi:H layer. Thin layer of aSi:H will act as a new incubation layer for the next ncSi:H layer. Figure 2.9 is the typical superlattice structure with alternating amorphous and nanocrystalline layers. Thicker aSi:H layer may lead to bad quality films due to poor collection of carriers which is shown in Figure 2.10 and it is vital to optimize the aSi:H thickness [62].

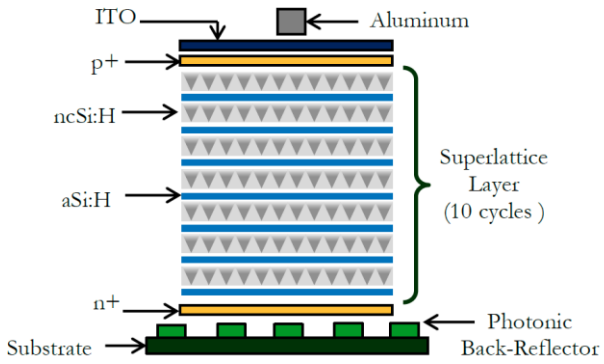

Figure 2.9 Schematic diagram of the superlattice structure showing the layer by layer growth of the film [62]

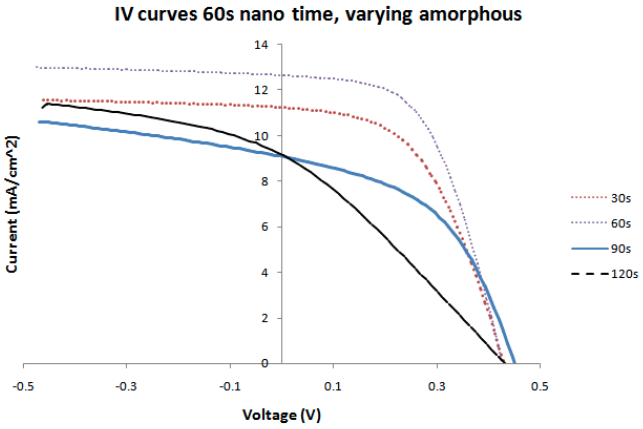

Figure 2.10 Device performance with different a-Si:H thickness for a fixed nc-Si:H layer in a superlattice [62]

2.1.3 Defects in nc-Si:H

One of the requirements to fabricate high efficiency nc-Si:H solar cell is to maintain low defect density in the i-layer [46]. This can be attained by reducing the unintentional contamination due to impurities. Oxygen, Nitrogen and Carbon are the main impurities that might be introduced at the time of deposition. Another source of contamination might be from leaks or outgassing in the reactor chamber.

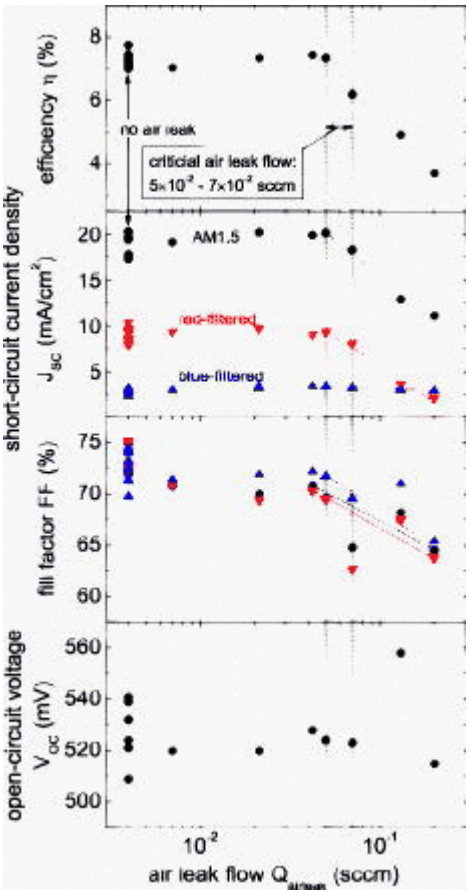

Figure 2.11 Degradation of device performance due to air leak [63]

The effect of oxygen and nitrogen on the performance of nc-Si:H solar cells was thoroughly studied by Kipler et. al [63]. Oxygen and Nitrogen are introduced into reactor chamber intentionally during the deposition process. Using SIMS (Secondary Ion Mass

spectroscopy), critical impurity concentration levels for both nitrogen and oxygen were measured and found out that they both initiate the degradation of the material. Figure 2.11 shows the degradation in device performance due to intentional air leak. It shows that beyond 0.07 sccm of air leak, the device starts to degrade. Figure 2.12 shows the QE degradation with various amounts of Oxygen and Nitrogen concentrations and maximum deterioration is observed at higher wavelengths suggesting the formation of recombination centers. It is also reported that even minimal Oxygen has a strong effect on the device performance compared to Nitrogen. This is a key observation as the reactor chambers are prone to air leaks and outgassing, so it is necessary to achieve a good base pressure for fabricating high efficiency solar cells.

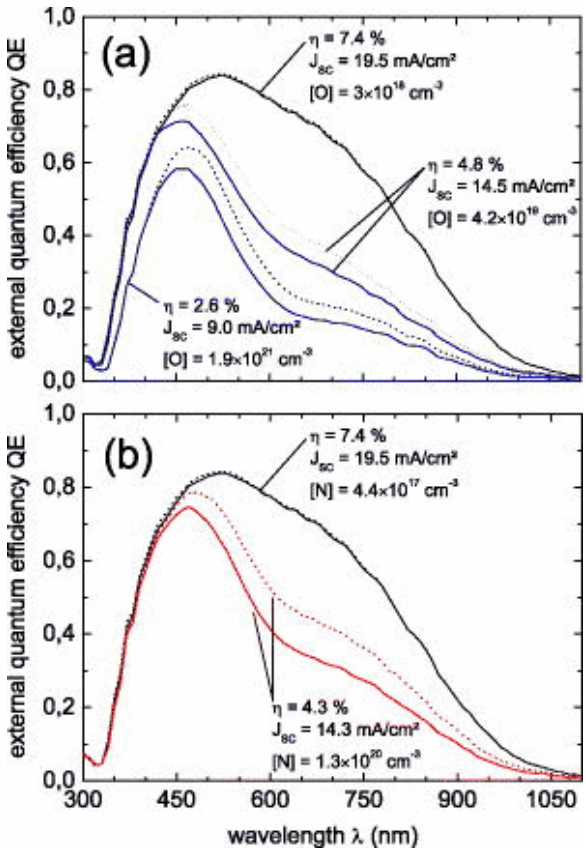

Figure 2.12 Degradation in QE fo nc-Si:H solar cells with various oxygen (a) and nitrogen (b) contents [63]

The defect density measurements in nc-Si:H with different Oxygen content was discussed by Hugger et. al [64]. The variation in deep defect density with crystallinity of the material is also studied. Drive level capacitance profiling (DLCP) method was used to estimate the defect density by Heath et. al [65]. Figure 2.13 shows the increase in deep defect density with crystallinity and Oxygen content. It was concluded that Oxygen could be creating the deep defect states in the grain boundaries near the crystalline/amorphous phase.

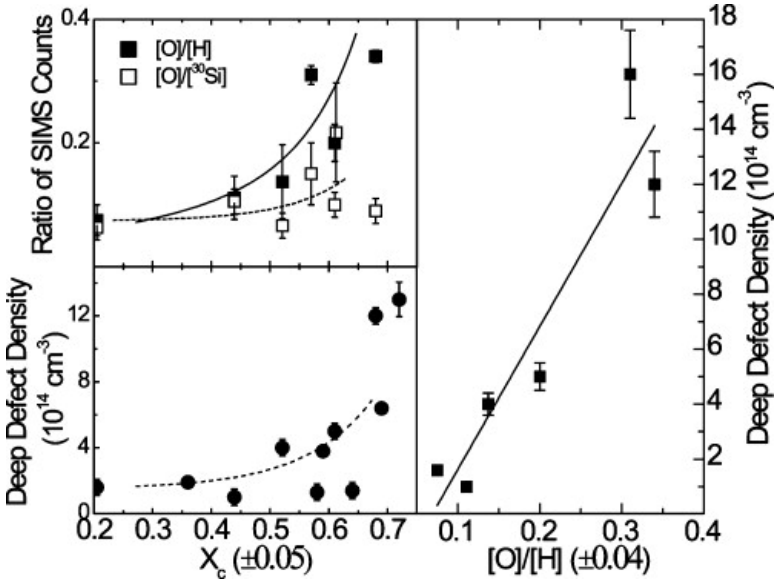

Figure 2.13 Deep defect density vs. crystallinity & Oxygen content [64]

Detailed study of minority carrier life time, defect densities, midgap and tail state distribution in nc-Si:H solar cells was done by several researches at Iowa State University. Sharma [66] worked on evaluation of defects in nc-Si:H by deliberate doping with PH_3 and it is observed that both deep defects and the shallow defects increase due to the incorporation of P which is shown in Figure 2.14. Saripalli [67] has evaluated minority carrier lifetime and it was found to be linearly correlated with the inverse of defect density (Figure 2.15) in nc-Si:H solar cells.

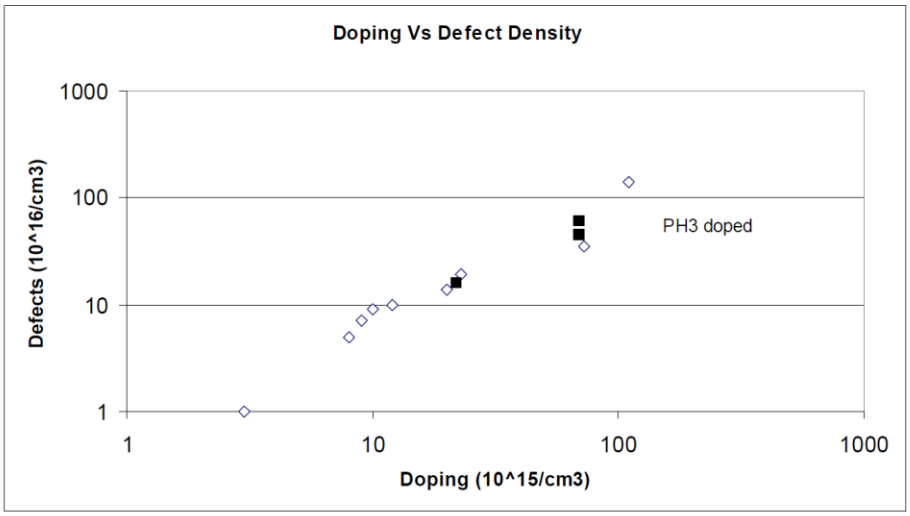

Figure 2.14 Effect of PH3 doping on defects in nc-Si:H solar cell [66]

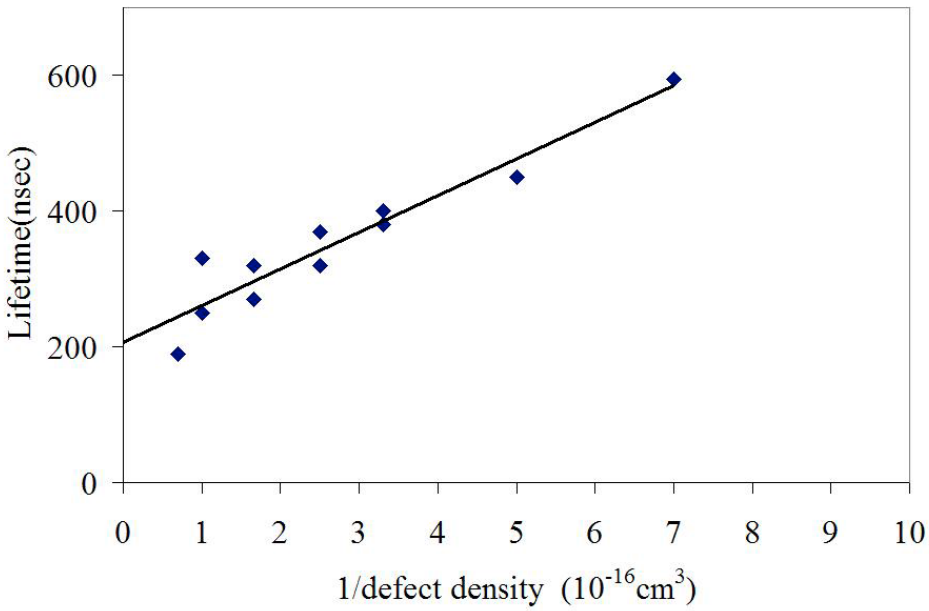

Figure 2.15 Minority carrier lifetime vs. Defect density in nc-Si:H soalr cell [67]

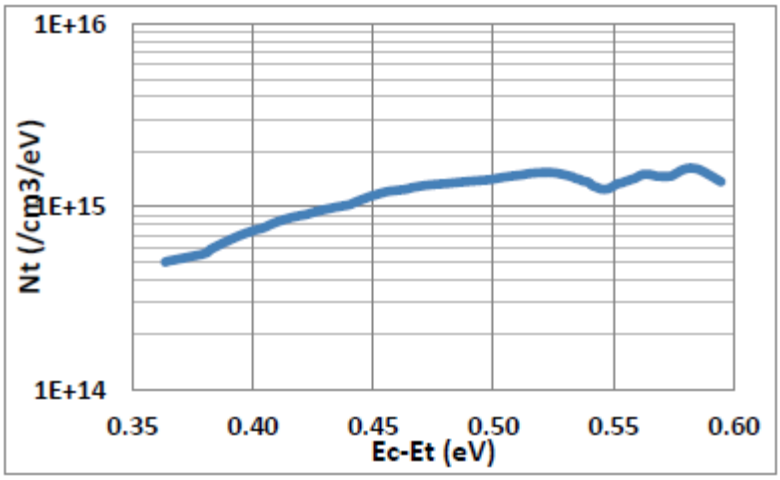

Figure 2.16 Defect Profile for nc-Si:H sample calculated from CF data [68]

Kajjam [68] reported systematic analysis of defect density profile in nc-Si:H solar cell and the effect of Oxygen doping. Capacitance-frequency measurements were used to estimate the defect density in nc-Si:H solar cell (Figure 2.16) and wavelet denoising technique was developed to effectively remove the noise [69]. Figure 2.17a shows the steady increase in both dopant and defect densities with deliberate Oxygen doping. The increase in defect density at 0.38eV and 0.51eV below the conduction band was explained by trap energy levels created by Oxygen in c-Si and oxygen incorporation into the crystal grains of the material. It is reported that Boron can be used to compensate the defects due to Oxygen and Figure 2.17b shows the reduction of defect densities with ppm level Boron doping. This phenomena was explained by the fact that Boron readily forms BO complex which in turn does not create any electrically active defects in nc-Si:H material.

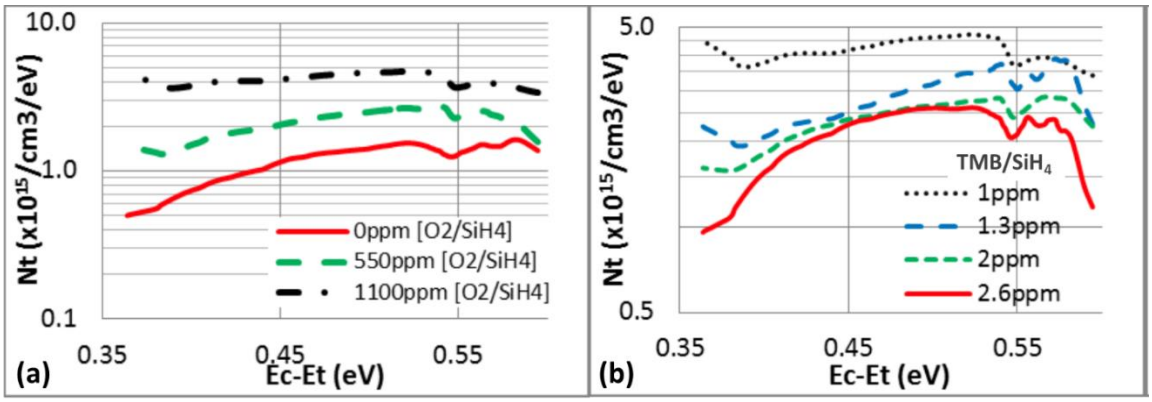

Figure 2.17 (a) Defect density profiles as a function of Oxygen content in nc-Si:H solar cell, (b) Defect density profile with varying Boron doping in nc-Si:H soalr cell containing 1100ppm [O_2/SiH_4] [68]

2.2 Nanocrystalline Silicon Germanium

Multiple junction solar cells with a-Si:H/nc-Si:H were successfully implemented by many research groups with efficiencies reaching 15% [70-73]. In tandem solar cells, a-Si:H absorbs short wavelengths and nc-Si:H absorbs red to infrared lights that penetrate through the top a-Si:H cell. Thicker nc-Si:H layer is needed to increase the infrared absorption; however it degrades carrier collection, hence the need of stronger infrared absorber to improve the efficiencies. Hydrogenated nanocrystalline silicon germanium (nc-SiGe:H) is a suitable material with good absorption extending it to infrared region even with thin layers. By varying the Ge content in nc-SiGe:H, the bandgap can be tuned from Si (~1.1 eV) to Ge (~0.7 eV). The absorption spectra of nc-$Si_{1-X}Ge_X$ for various Ge content is shown in Figure 2.18. There is a redshift in the absorption spectra as the Ge content increases. In the main solar absorption range nc-SiGe with X_{Ge}>0.5 has significant increase in the absorption. So this material is theoretically capable of achieving higher current densities than nc-Si:H in the infrared region. The variable bandgap nature of nc-SiGe:H make it an attractive material for TFTs as well [74].

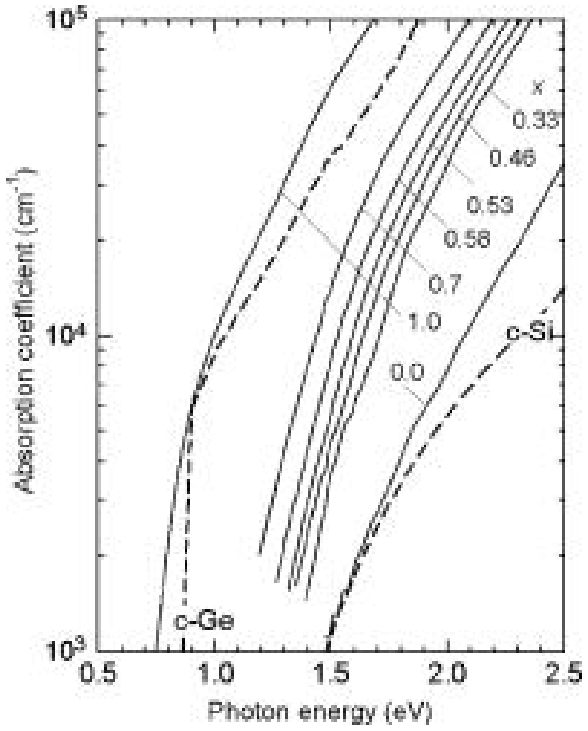

Figure 2.18 Absorption spectra of nc-$Si_{1-x}Ge_x$ films for different Ge concentrations [75]

2.2.1 Material Growth

Ganguly et.al [76] reported a systematic study of nc-SiGe:H growth with varying PECVD parameters such as Hydrogen dilution, power, pressure and temperature. It was found that for every temperature there is an optimum Hydrogen dilution for attaining maximum grain size as shown in Figure 2.19. The optimum Hydrogen dilution suggests that Hydrogen participates in crystallites formation and also in ion bombardment which disrupts crystal growth. The balance between these two reactions leads to the largest crystallite formation at a particular temperature. It is also observed that optimum hydrogen dilution decreases with temperature suggesting that Hydrogen is providing the necessary energy at low temperatures for crystal formation. The detrimental effect of Hydrogen at higher temperature is explained by the fact that rate of dissociation of Si-Si bond by H ion is more than thermal desorption of H from Si-H bond.

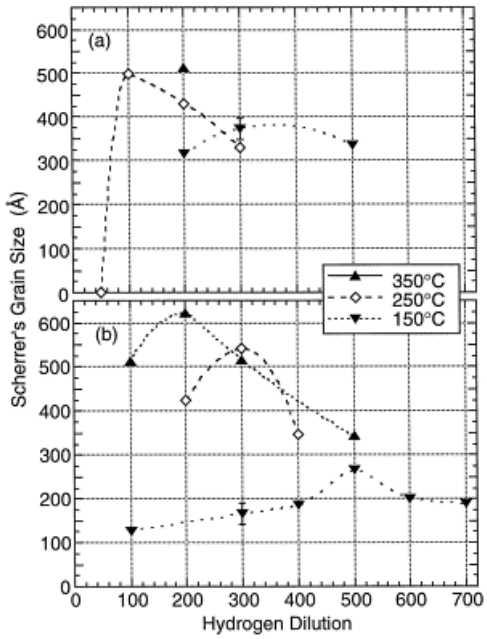

Figure 2.19 Grain sizes versus hydrogen dilution for nc-SiGe:H samples deposited at (a) 0.5mT, 89mW/cm^2 and (b) 0.9mT, 637mW/cm^2 at different temperatures [76]

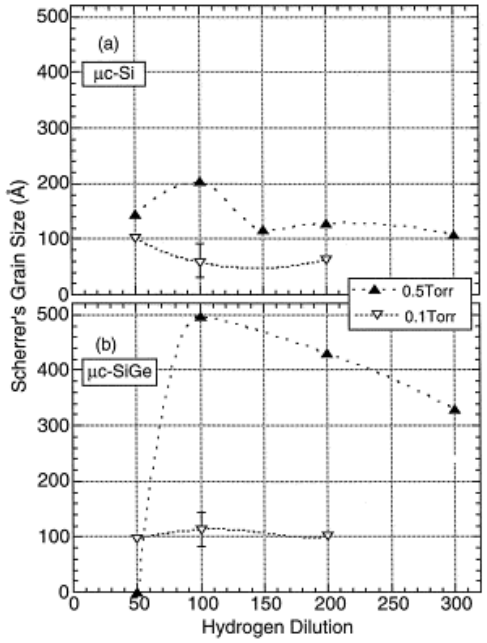

Figure 2.20 Grain sizes versus hydrogen dilution for (a) nc-Si:H and (b) nc-SiGe:H deposited at 250C [76]

Figure 2.20 shows the study of grain size versus hydrogen dilution at different pressures for nc-SiGe:H and nc-Si:H. It was observed that the formation of crystallites in nc-Si:H appeared even at lower Hydrogen dilution, but at higher Hydrogen dilution nc-SiGe:H shown

larger grain size compared to nc-Si:H. Dalal [77] explained this phenomena in nc-Ge:H films. It is because Ge-H bond is weaker compared to Si-H bond; therefore surface desorption of H_2 from Ge-H bond is easier and leads to higher grain size in nc-Ge:H.

The Raman spectra of nc-SiGe:H grown by PECVD for various Ge content was reported by Houben et. al [78]. Raman spectra is shown in Figure 2.21, it was concluded high Ge contents results in good crystallinity of Ge-Ge crystals. It was also reported that nc-SiGe:H films shows cone-like crystals embedded in an amorphous matrix in the early stages of growth and fine-grain structure consisting of faulted single-crystal columns.

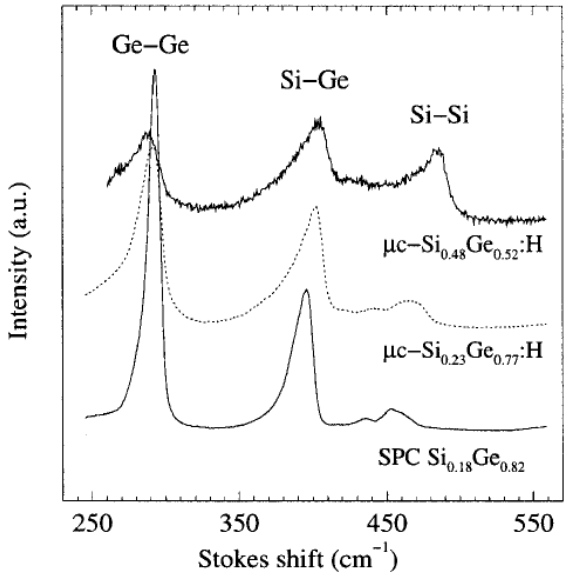

Figure 2.21 Raman spectra of the nc-SiGe:H films with varying Ge content [78]

Miyazaki et. al [79] reported Raman and TEM studies with varying Ge content. From TEM image, highly crystallized and structurally relaxed Si-Ge network was demonstrated in the temperature range 200-300°C. It was also described using Raman spectra that the necessary amorphous-incubation layer thickness was 25nm as compared to 5nm in nc-Si:H.

Electrical properties of nc-SiGe:H solar cells have been reported by Matsui et. al [75]. Measured electrical properties as a function of Ge content is shown in Figure 2.22. At X_{Ge}=0.75 fraction, mobility reaches maximum and the film changes from n-type to p-type. It was also found that the conductivity does not depend on the growth conditions like power and hydrogen dilution, but only depends on the Ge fraction. This observation is in contradiction to earlier studies [76].

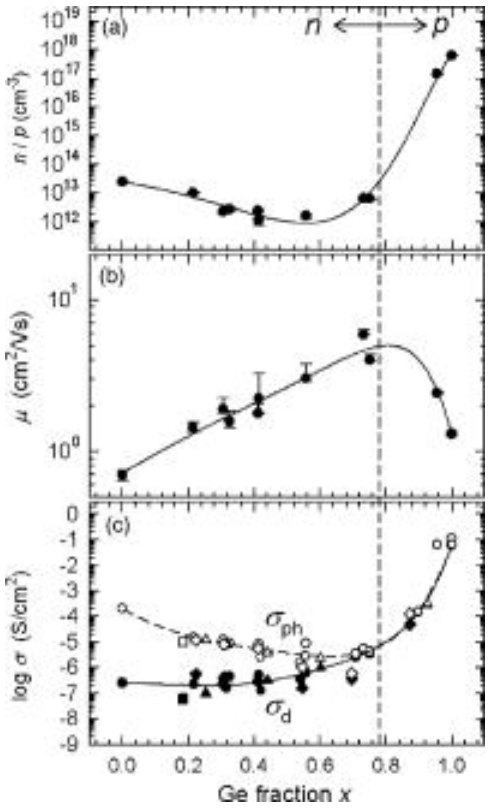

Figure 2.22 Electrical transport properties of nc-SiGe:H as a function of Ge concentration (a) carrier concentration, (b) Hall mobility μ and (c) coplanar conductivity σ [75]

Matsui et. al [80] also studied the atomic fraction of Ge in solid as a function of GeH_4 concentration in the gas phase, $[GeH_4]/[GeH_4]+[SiH_4]$. Figure 2.23 shows solid versus gas phase and the Ge fraction increases drastically to 0.8 and slowly increases to 1. It was proposed that Ge incorporation efficiency from GeH_4 is five times higher that Si from SiH_4 by using a

mathematical fit. This can also be explained by the lower dissociation energy and lesser thermal stability of Ge-H bond compared to Si-H bond. It was also claimed that the film growth of nc-SiGe:H is the sum of the individual growth rates of nc-Ge:H and nc-Si:H. This model indicates film growth is dominated by Si-Si and Ge-Ge crystallites rather than Si-Ge crystallites. There was no Raman data to support this argument.

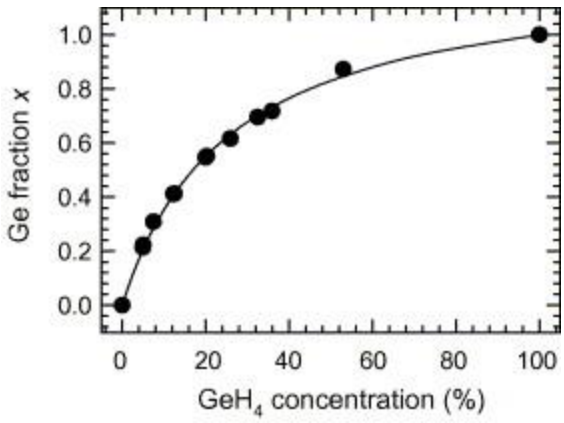

Figure 2.23 Ge fraction in the solid phase as a function of GeH_4 concentration in the gas-phase [80]

2.2.2 Device Performance

Preliminary n-i-p solar cells with nc-SiGe:H as the intrinsic layer deposited on statinless steel was reported by Rath et. al [81]. The promising result was a current density of 9.44 mA/cm^2 with base layer as thin as 150 nm without any back-reflector and V_{oc} of 0.43V for Ge Content of 60%. The explanation for better quality films was moderately high deposition rates. The device structure is shown in Figure 2.24. There were no IV curves to support their results.

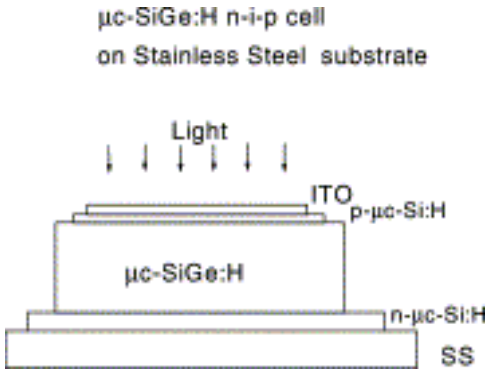

Figure 2.24 Device structure of the nc-SiGe:H n–i–p solar cell [81]

Isomura et. al [82, 83] achieved 5.6% of conversion efficiency in a nc-SiGe:H solar cell with Ge fraction of 20% and 500nm base layer. Figure 2.25 shows the illuminated IV curves and the device structure. Jsc of 28m/cm^2 was reported for a Ge fraction of 27%, but with a lower efficiency. Even with thinner devices, higher Jsc was explained by higher absorption in infrared region with a collection efficiency of 20% at 1200nm.

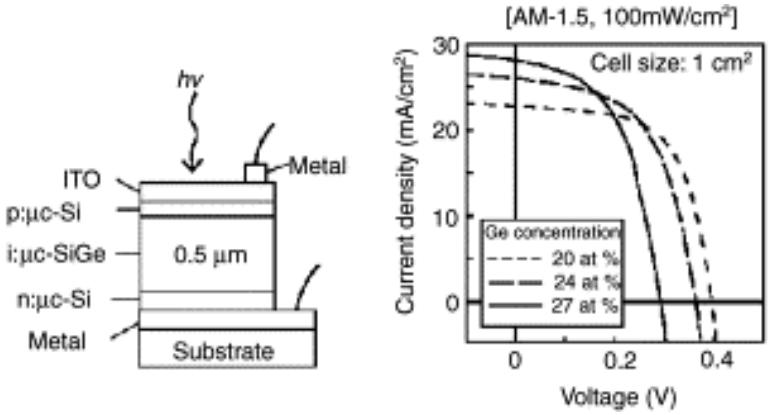

Figure 2.25 Device structure and illuminated JV curves for nc-SiGe:H solar cell with varying Ge content [83]

AIST Japan is one of the very active research group in the field of nc-SiGe:H solar cell applications [75, 80, 84-86]. Initial solar cells were reported with a strong infrared response and a photocurrent of 27.4 mA/cm^2 using 900nm base layer (X_{Ge}=0.4) under reverse bias voltage. As Ge content increased beyond 30%, there is drastic decrease in the photocurrent. Figure 2.26a shows the QE of nc-SiGe:H solar cell with varying Ge content; it is clearly seen

from the figure that for higher Ge content devices, there is a significant loss of low wavelength QE. Because of that, the efficiency drops from 3.4% for X_{Ge}=0.21 to 0.3% for X_{Ge}=0.55.

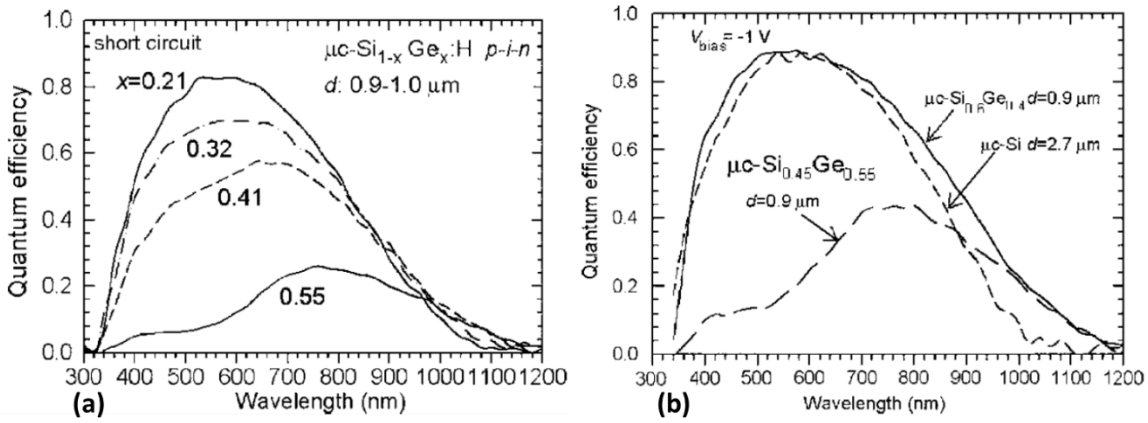

Figure 2.26 QE spectra of nc-SiGe:H solar cells with different Ge concentrations (a) under short circuit and (b) under reverse bias (-1V) [75]

It was claimed that the poor short wavelength response in higher Ge content devices is due to reduced carrier lifetime and the shallow absorption length. QE spectra of the nc-SiGe:H solar cell (X_{Ge}=0.4,0.55) measured under a reverse bias is shown in Figure 2.26b. It shows a strong bias-voltage dependence for X_{Ge}=0.4, explained as the field assisted drift transport of electrons. However for X_{Ge}>0.5, the field is opposed by the negatively ionized acceptors. It is suggested that band-gap engineering and material optimization is required to achieve high Ge content devices.

Recently, the same group reported high hole concentration in undoped nc-Ge:H films at higher crystalline volume fraction [85]. It was claimed that ESR and Hall measurements showed that the acceptor states increased due to Ge dangling bonds at the grain boundaries in highly crystalline films. Figure 2.27 shows ESR and carrier concentration of nc-Ge:H films as a function of crystallinity factor, defined as $I_R=I_{crystalline}/I_{amorphous}$. It was explained that the drop in the spin density with higher I_R is due to dangling bond defects created in crystalline Ge.

Theoretical study suggested that the defect state is below valence band for higher Ge content [87]. The explanation is ambiguous as the spin density should increase with dangling bond defects. It was also shown that intentionally introducing CO_2 gas during nc-Ge:H growth, decreases the hole concentration (Figure 2.27c) by two orders of magnitude.

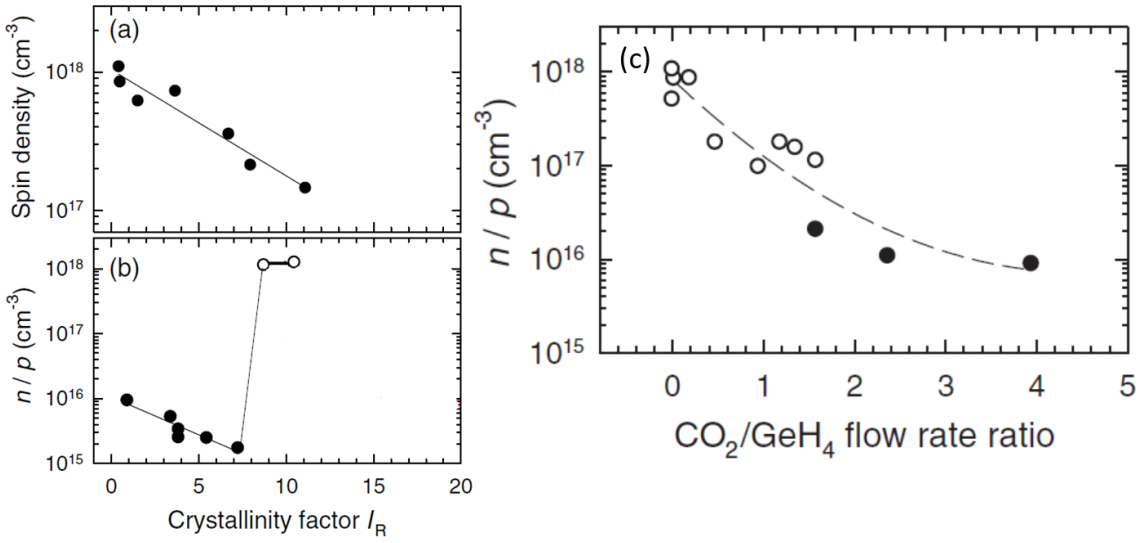

Figure 2.27 (a) ESR spin density, (b) carrier concentration as a function of I_R in nc-Ge:H film and (c) carrier concentration as a function of CO_2 gas flow during deposition. n (closed symbols)/p (open symbols) [85]

The same concept was applied in nc-SiGe:H devices with higher Ge content. Better device performance was demonstrated with appropriately doping nc-SiGe:H with oxygen. The improvement in lower wavelength QE for nc-SiGe (X_{Ge}=0.3) with CO_2 incorporation is shown in Figure 2.28. It was also observed that higher concentration of Oxygen doping reduces the QE at higher wavelength, which may be due to n-type nature of Oxygen. The conclusion was that Ge creates dangling bond defects at higher concentrations; however it can be compensated by Oxygen donors.

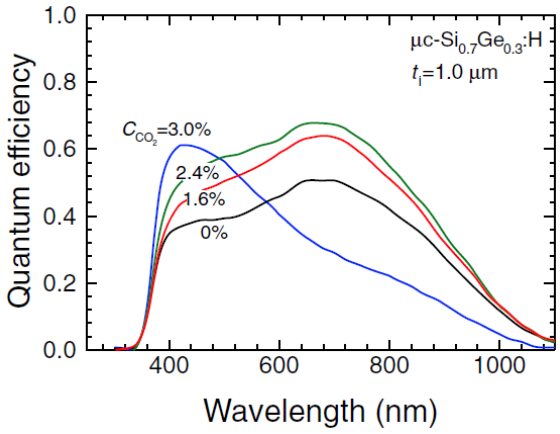

Figure 2.28 QE of nc-SiGe:H solar cells for different CO2 concentrations during the deposition [85]

Various other groups also reported nc-(Si,Ge):H solar cells with potential for tandem junction devices [88-91]. However only a few groups addressed the challenge with photo-carrier response at higher Ge content (X_{Ge}>0.3) for lower wavelengths (λ < 700nm).

2.3 Motivation

Though several groups have reported nc-(Si,Ge):H solar cells with higher absorption in infrared region, the reason for significant QE drop in lower wavelength region is not clear. It has been observed that with higher Ge content the absorption coefficient increases, but it deteriorates the transport properties like diffusion length and minority carrier lifetime. There is no supporting defect density data to support the claim that Ge is creating acceptor like defects Another important challenge is to correlate the transport properties with material quality, especially grain size, crystallinity and grain boundary passivation.

These results indicate a need for a systematic study of the fundamental properties such as carrier mobility, mid-gap defect densities, tail state densities and diffusion lengths in nc-SiGe:H and their relationship to grain size and Ge content. Further, it is important to understand the correlation between grain growth and mobility with impurities and Hydrogen bonding.

CHAPTER 3. GROWTH AND CHARACTERIZATION

3.1 Fabrication Process

In this chapter, the methods employed in the fabrication of nc-Si and nc-SiGe based solar cells is explained. It also contains the various measurement techniques used to characterize the fundamental properties of solar cells.

3.1.1 Plasma Enhanced Chemical Vapor Deposition (PECVD)

PECVD is the most commonly used method for thin film deposition for silicon based solar cells. The main benefit of PECVD is the ability to deposit thin film at relatively lower temperatures compared to conventional CVD systems. The advantages of high frequency over DC discharge was first demonstrated by Robertson et.al [92]. The main advantages of higher frequency plasma are lower ion energy and higher electron density. Ion energy reduces with increase in frequency which helps to fabricate better quality films and electron density increases with frequency results in higher deposition rates. As shown in Figure 3.1, threshold for defect formation is around 50MHz and higher electron density can be achieved at this frequency.

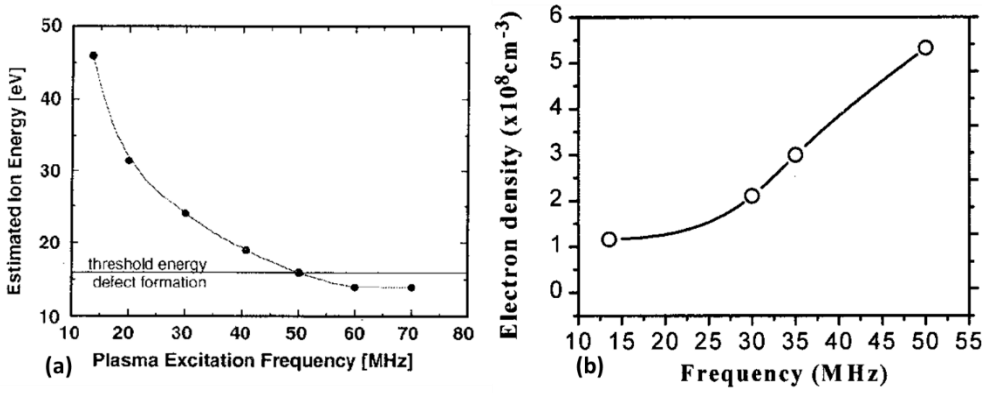

Figure 3.1Variation of plasma parameters with increase in plasma frequency (a) Ion energy vs. Frequency [93] (b) Electron density vs. Frequency [94]

There are four major components in a PECVD system, reaction chamber, vacuum pump, power supply and monitoring networks. The reaction chamber consists of an electrode and substrate holder which will act as a parallel plate capacitor. This chamber is hooked up to a gas manifold, power generator, plasma monitoring equipment and vacuum system. All the gases are connected to gas manifold through series of valves and mass flow controllers which regulate the gas flow into the chamber. Turbo pump in the vacuum system helps to achieve lower pressure i.e. $1x10^{-7}$ Torr. The plasma is generated using RF power from a function generator in combination with a power amplifier and a matching box to achieve maximum forward power. Oscilloscope and multi-meter are used to measure plasma characteristics inside the chamber. Pressure and temperature are continuously monitored using the baratron and thermocouple respectively. Schematic of a typical PECVD system is shown in Figure 3.2.

Amorphous and nanocrystalline layers are grown using high frequency (~45MHZ) capacitively coupled RF plasma. In this process Si and Ge are deposited from gaseous state to solid state on to a substrate. Chemical reactions occur in plasma among the created radicals. Two different PECVD reactors are used for thin film deposition namely Reactor 1 (R1) and Reactor 2 (R2). R1 is primarily used to deposit the intrinsic layer to avoid contamination from dopant gases, whereas all the doping layers are done in R2. Figure 3.3 shows both the reactors R1 and R2 available at Iowa State University.

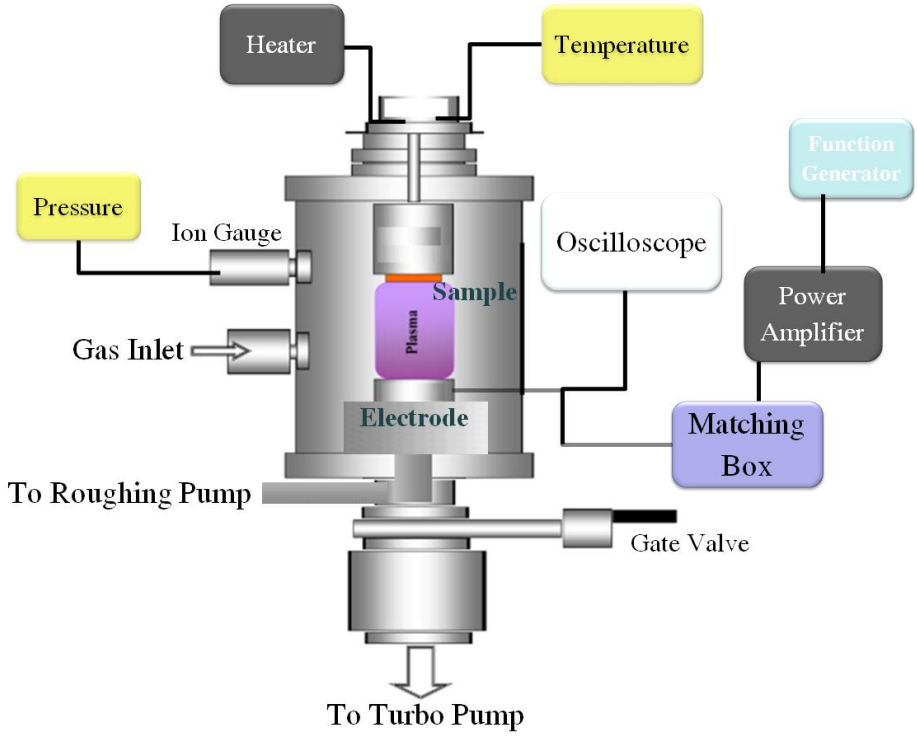

Figure 3.2 Schematic of PECVD reactor

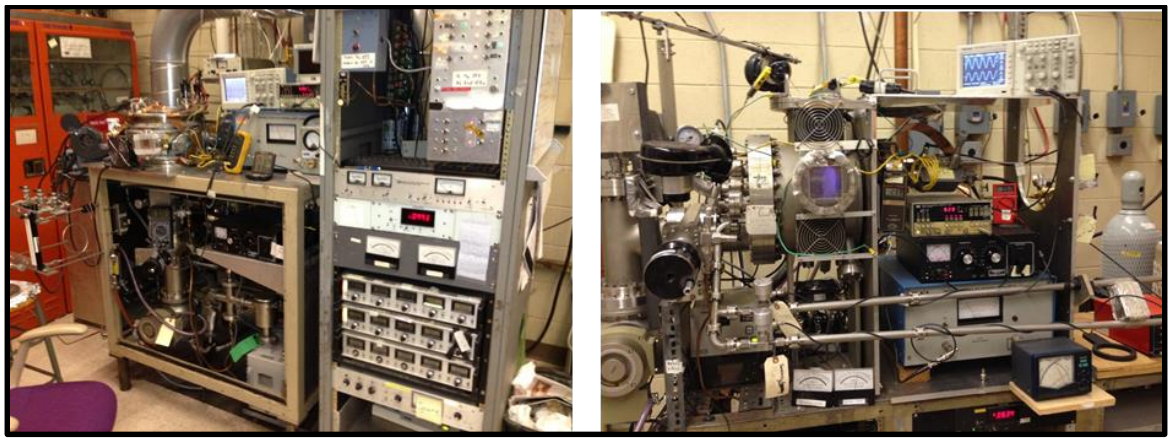

Figure 3.3 PECVD reactors (R1 and R2) at Iowa State University

3.1.2 Sample Preparation

Devices are generally grown on electropolished stainless steel (SS) substrates. These substrates are pre cleaned in boiling acetone, followed by boiling in mixture of Ammonium Hydroxide and Hydrogen Peroxide (NH_4OH and H_2O_2) solution and finally ultrasonicated in

methanol to remove any unwanted impurities on the surface. After loading the substrates into the chamber, several Nitrogen purges are given followed by Hydrogen and Silane purges to ensure the system is free of any oxygen and moisture. Once the chamber reaches lower 10^{-6} Torr, a dummy plasma layer with shutter closed is done to coat the inside of chamber and also to achieve stable plasma with required substrate temperature. Temperatures are generally ramped to 50°C higher than required temperatures and allowed to cool back to required temperature.

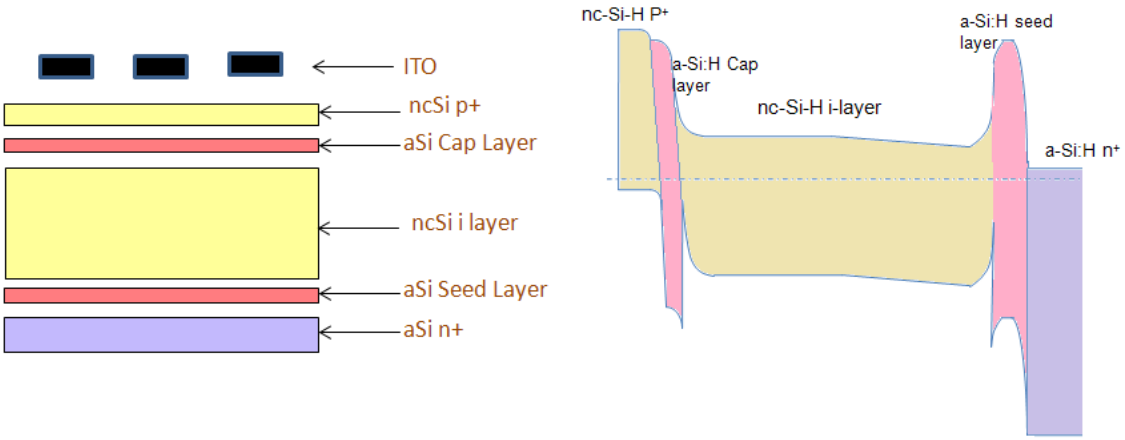

Figure 3.4. Device structure and band diagram of p-i-n nc-Si:H solar cell

The first layer deposited is 0.3µm thick a-Si n+ layer using 0.5% PH_3 and acts as a back contact. A thin layer of a-Si lightly doped with PH_3 is deposited as seed layer for nc-Si. The main function of seed layer is to provide the nucleation sites and prevent P diffusion into the main intrinsic layer [95]. Initially, high hydrogen dilution is used to help form nucleation centers and quickly start onset of crystallization. The initial dilution ratio is gradually reduced as the film grows which helps in maintaining the optimum crystallinity of intrinsic layer to produce best devices. There are other methods for controlling crystallinity like power grading and superlattice structures, discussed in detail in Chapter 4. Intrinsic layer is followed by a thin

layer of nc-Si:H p+. Figure 3.4 shows the device structure of typical nc-Si device and the band diagram. To improve the range of carriers, intrinsic layer is graded using ppm levels of PH_3 and Trimethyl Boron (TMB) which also helps in reducing oxygen going into i-layer. A thin layer of amorphous silicon cap layer is deposited on main i-layer to prevent post deposition oxidation through grain boundaries and also improves open circuit voltage by reducing reverse saturation current. Final p+ layer consists of an amorphous seed layer, nanocrystalline layer and an amorphous cap layer. The p+ layer is highly doped with Diborane to ensure good top ohmic contact. Relatively low temperatures are used to deposit p+ to prevent any kind of boron diffusion into the intrinsic layer. Finally, the top contact made of transparent conductive oxide is deposited in a sputtering system.

3.1.3 Sputtering

In semiconductor industry sputtering widely used as it is a faster deposition process than thermal evaporation it is used to deposit transparent conducting oxides. Indium Tin Oxide (ITO) is used as the top contact for the nc-Si solar cells. The basic principal of sputtering is to bombard the target material with high energy Ar ions which knocks off the material from target and get deposited on the substrate. RF plasma is used to get better quality films at higher deposition rates and avoid charging on the film. RF Sputtering system is in-house built and shown in Figure 3.5.

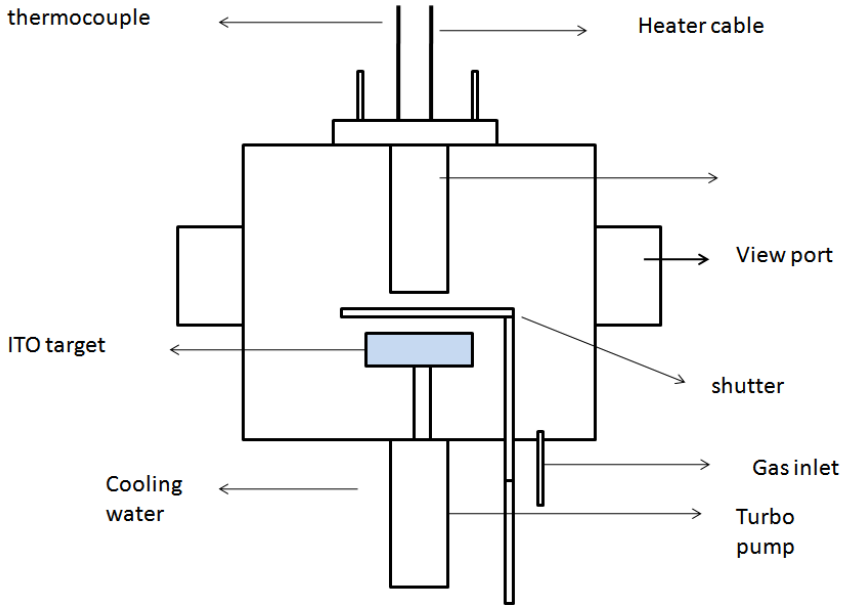

Figure 3.5 RF Sputtering system

For ITO calibration, thick films are deposited on Corning 7059 glass which are used to calculate the growth rate and resistivity. ITO is deposited at 225^0C and 5mT, and the resistivity is $3x10^{-4}$ ohm-cm. Transmission of more than 80% is observed for working wavelengths. In order to achieve anti reflection coating, the thickness is calculated from the wavelength where maximum absorption occurs and the thickness is 70nm for Silicon.

3.2 Measurement Techniques

Fundamental properties of solar cells can be determined by using various electrical and optical characterization techniques. Measurement of parameters is an important part of research as it helps in proceeding in right direction. It is important to understand the structural properties of the films before making devices. Once the desired film properties are achieved, devices are made for extensive study of device properties. In this section different characterization techniques for solar cells are discussed in detail.

3.2.1 Optical Spectroscopy

Optical spectroscopy of thin films can be used to estimate the thickness and understand the absorption properties. Thin film structures have a series of interferences due to reflection from two different surfaces, and distance between the peaks or valleys is a direct representation of the thickness of the film as shown in Figure 3.6. Thickness of thin film can be estimated using following equation [96].

$$t = \frac{\lambda_1 \times \lambda_2}{2(n_1 \times \lambda_2 - n_2 \times \lambda_1)}$$

where λ_1 and λ_2 are two adjacent peaks or valleys having refractive index n_1 and n_2 respectively.

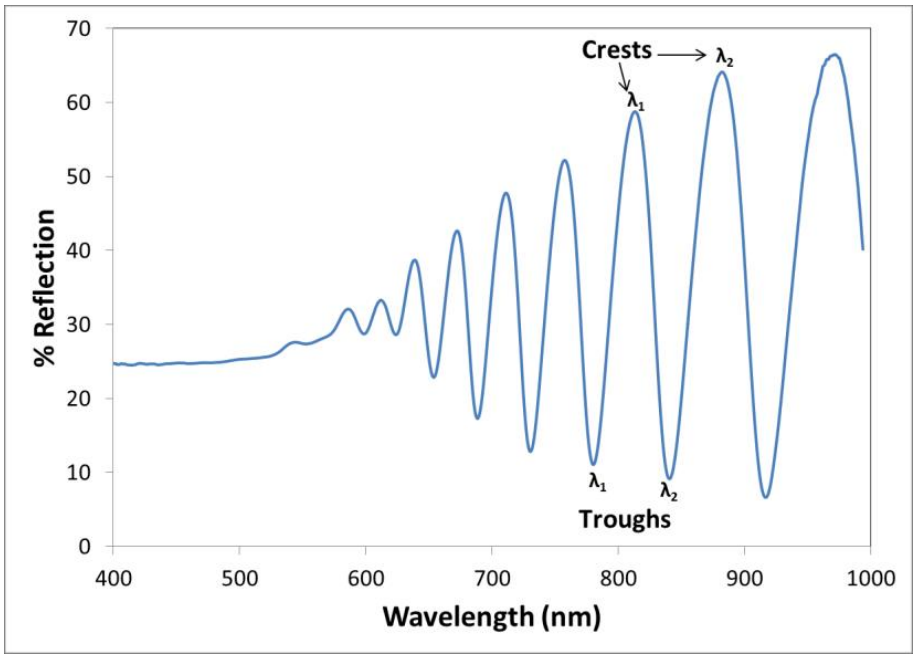

Figure 3.6 Typical Reflection data for a thin film sample

3.2.2 Raman Spectroscopy

Raman spectroscopy is used to measure crystallinity of a material. When light is incident on a solid, photons scatter elastically and inelastically; majority will be elastic scattering which is referred as Raleigh scattering as shown in Figure 3.7. Important

phenomenon here is in-elastic scattering, which causes lattice vibrations and produce phonons which cause a shift in energy of incident photon which is called Raman shift [97].

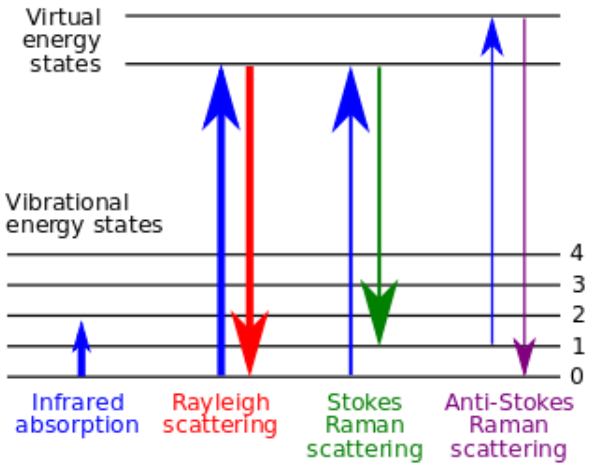

Figure 3.7 Scattering phenomena in a material due to incident light

In crystalline silicon only the optical phonon with 64meV energy has zero momentum and results in a sharp peak at 520cm^{-1}, where as in amorphous Silicon momentum is conserved over a band of energies which causes a band of small peaks added together for a broad spectrum with peak at 480 cm^{-1}. Different phases in Silicon are shown in Figure 3.8.

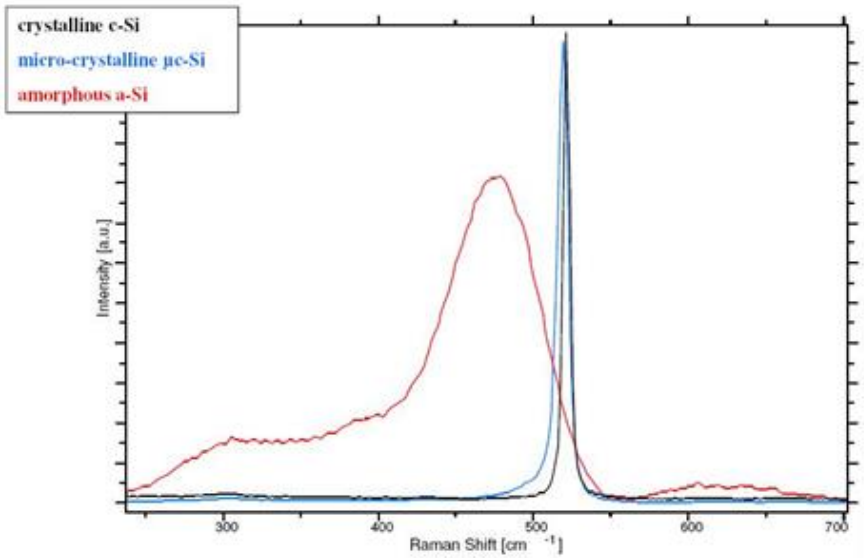

Figure 3.8 Raman spectrum for different phases of Silicon

The peak corresponding to amorphous portion is a broad Gaussian peak due to greater disorder in the bond lengths whereas crystalline peak will be a fine Lorentz fit since the bond length is firm. The analysis involves separating the peaks from the total curve and calculating the heights of the individual peaks. It is a common misconception that the areas of the peaks need to be used to calculate the fractions but since one curve is a Gaussian and the other is Lorentzian, the areas are not comparable. Also the area under ideal Lorentzian diverges, hence the heights of the peaks are considered as a useful indicator to calculate crystallinity fraction in nc-Si [98].

3.2.3 X-ray Diffraction (XRD)

XRD is used to determine the grain sizes in nanocrystalline films. According to Bragg's diffraction, when the incident radiation wavelength is of the order of distance between the planes, the radiation constructively interferes and forms diffraction patterns as shown in Figure 3.9. From the angle at which the diffraction pattern is forming can be used to estimate the distance between the planes. For a crystalline solid with lattice planes separated by a distance d, the reflected waves constructively interfere when the path length between them is an integral multiple of λ [99].

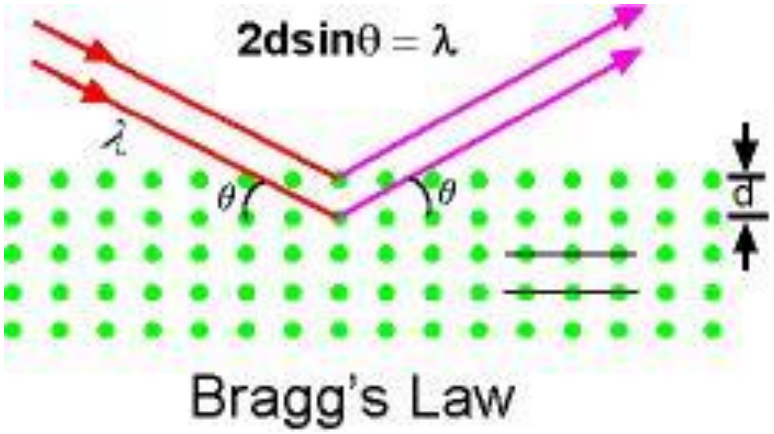

Figure 3.9 Braggs diffraction on lattice planes separated by a distance d

The grain size of a nanocrystalline material can be estimated using Debye-Scherer's formula [100] given below.

$$d = \frac{0.9\lambda}{(\beta \cos\theta)}$$

where λ is the incident wavelength, β the full width and half maximum (FWHM) and θ is the angle of incidence.

In nc-Si and nc-SiGe two kinds of grains are predominant <111> and <220>. In Silicon based films <111> is independent of growth conditions, whereas <220> is dependent on substrate temperature, pressure and Hydrogen content [101]. The most crucial plane is <220> as it determines the transport properties of the carriers. Higher the <220> grain size, better are the device properties due to reduction in grain boundaries [102].

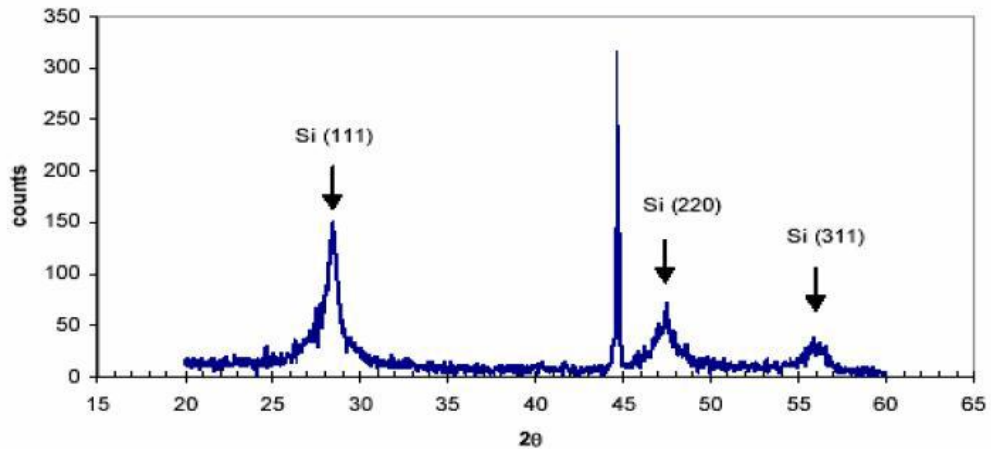

Figure 3.10 XRD plot of intensity vs. angle 2θ for a nc-Si film

Typical XRD curve for nc-Si is shown in Figure 3.10. The peak at 28° corresponds to the < 111 > plane, while the peak at 47° corresponds to the < 220 > plane. Around 56°, < 311 > plane can also be observed in highly crystalline films. The sharp peak around 44 degrees corresponds to the SS substrate.

3.2.4 Energy Dispersive X-ray Spectroscopy (EDS)

EDS is an analytical technique used for elemental analysis of a material. It relies on interaction between X-rays and elements in the sample. Each element has a unique atomic structure producing unique set of peaks in its X-ray spectrum. To stimulate the emission of characteristic X-rays from a sample, high energy X-ray beam is focused on to the sample. The incident beam excites the electron in inner shell and creates a hole; immediately electron from higher energy level jumps into lower level releasing the excess energy as X-ray.

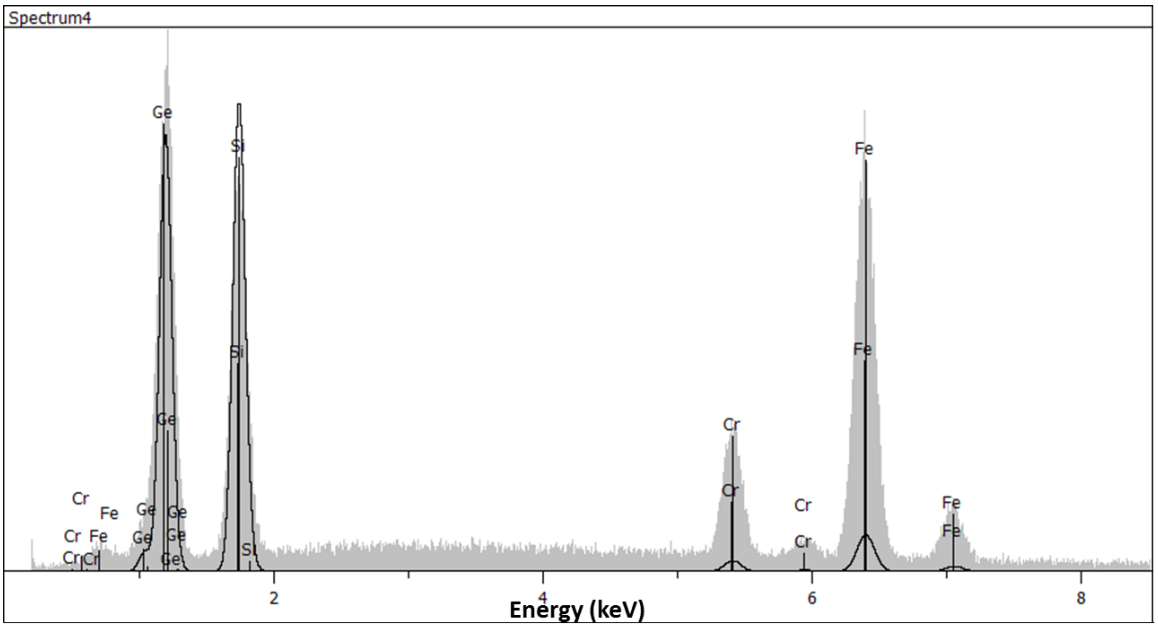

Figure 3.11 Typical EDS spectrum of nc-SiGe:H film grown on Stainless Steel Substrate

The number and energy of that X-ray can be measured using Energy Dispersive Spectrometer. As these X-rays are characteristic of the difference between the two levels and atomic structure of the element, this gives the elemental composition of the sample [103]. Typical EDS spectrum of a nc-SiGe on SS substrate is shown in Figure 3.11.

3.2.5 Space Charge Limited Current (SCLC)

Mobility of the samples is measured using SCLC technique. Insulators and semiconductors exhibits a phenomenon called space charge limited current (SCLC) when number of carriers injected into sample exceeds the resident charge in the sample. The electric field inside the sample become non-uniform when injected carriers exceed the thermal carrier concentration and no longer obeys Ohm's law. The device used to measure SCLC is an n-i-n device. The band diagrams for an n-i-n device, under electrical bias, are shown in Figure 3.12. The intrinsic layer is sandwiched between two heavily doped n+ layers. Heavily doping the layers on both sides of the intrinsic layer allows electrons to easily be injected into the intrinsic layer. To study the mobility of holes, the n+ layers of the device would be replaced by p+ layers [104].

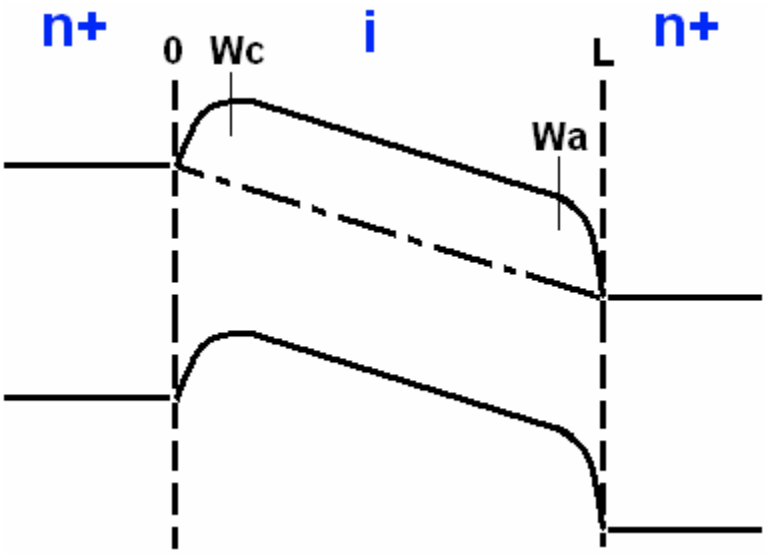

Figure 3.12 Band diagram of an n-i-n device under electrical bias [104]

The detailed theory of SCLC can be found in [105] and can be simplified by neglecting the diffusion current. In order to neglect the diffusion current i-layer thickness should be longer than the diffusion length. The voltage at which all the traps in the material are filled i.e. the

injected carriers are comparable to resident charges is called V_{SCLC}, it can be calculated using equation below. In the equation q is charge of electron, n_0 is the carrier concentration, t is the thickness of i-layer and ε is the permittivity of the material.

$$V_{SCLC} = \frac{q * n_0 * t^2}{\varepsilon}$$

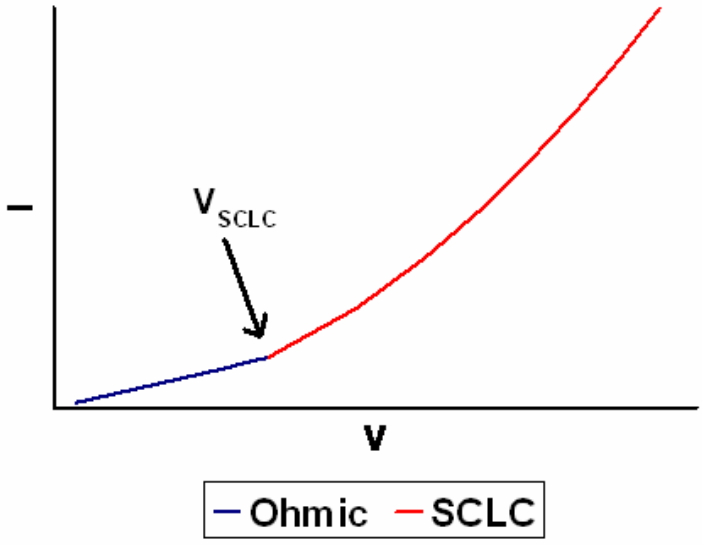

Figure 3.13. Typical current vs. voltage curve in a semiconductor

The current versus voltage curve of semiconductor has two regions; one below V_{SCLC} is Ohmic region and one above is SCLC region (Figure 3.13). The current follows SCLC equation after V_{SCLC}.

$$I = \frac{9 * \varepsilon * A * \mu}{8 * t^3} * V^2$$

where A is the area of contact and μ is the mobility of the material. Using this equation mobility of the material can be estimated.

3.2.6 Current-Voltage (IV) Characteristics

The IV experiment is the most important tool for characterizing a solar cell and it helps in evaluating power conversion efficiency (PCE). Figure 3.14 is the typical IV curve of a solar cell measured under AM 1.5 solar lamp. Open circuit voltage (V_{oc}), short circuit current (J_{sc}) and fill factor (FF) are obtained from an IV curve of a solar cell. V_{oc} is the voltage developed across the cell when no current is flowing. In nanocrystalline solar cells, V_{oc} is mainly depends on crystallinity of i-layer and interfaces present in the device which helps to control the reverse saturation current (J_0) [14]. J_{sc} is the current generated by the solar cell when load across the cell is shorted. Jsc is governed by the thickness, crystallinity and quality of the intrinsic layer.

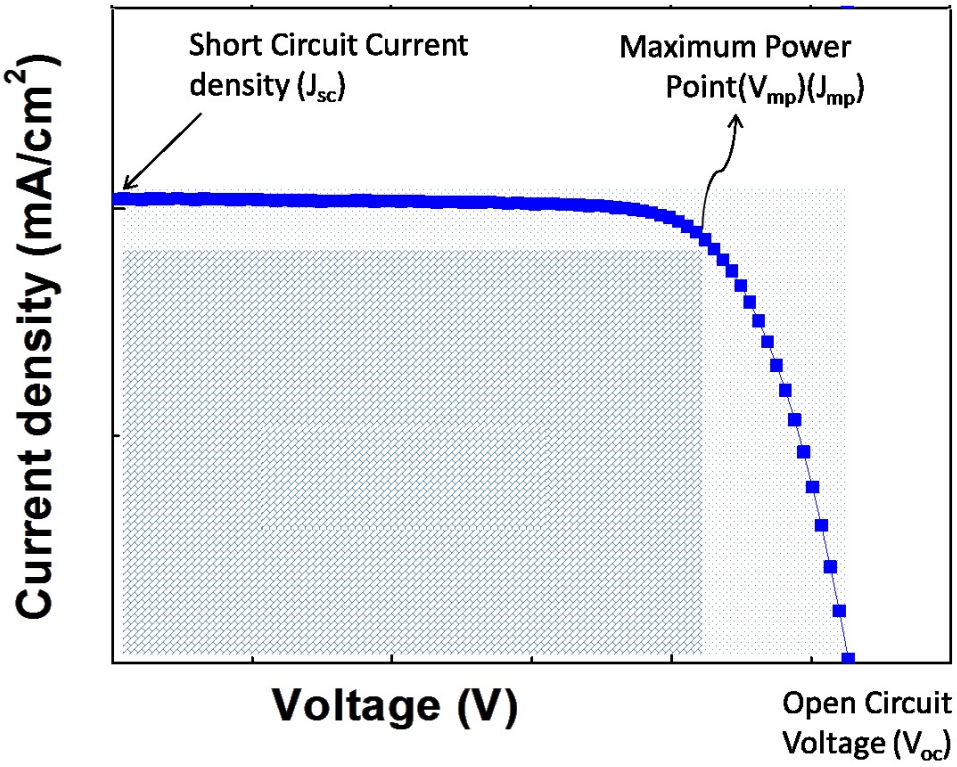

Figure 3.14 A typical IV curve of a solar cell.

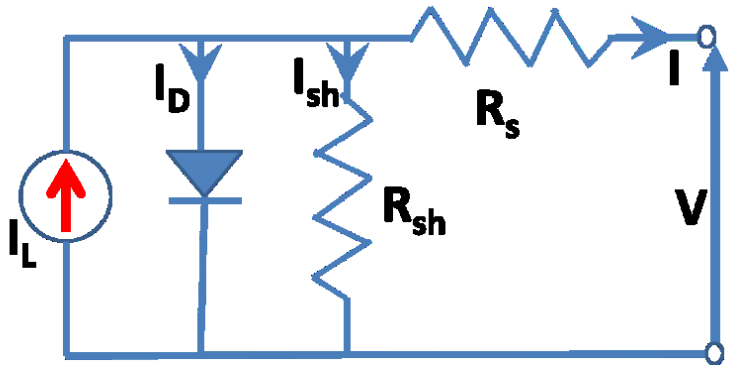

Figure 3.15 Electrical equivalent circuit of a solar cell

FF is defined by the squareness of the IV curve, which is the ratio of maximum power point (V_{mp} . J_{mp}) to (V_{oc} . J_{sc}) where V_{mp} and J_{mp} are the voltage and current at maximum power point. FF depends on series resistance (R_s), shunt resistance (R_{sh}) and collection property. If the series resistance is high there will be power loss (I^2 R_s) and if shunt resistance is low then most of the current will leak which lowers the open circuit voltage. This can be easily understood by looking at the equivalent circuit of a solar cell in Figure 3.15. Collection property is also equally important because poor collection will lead to lower output power. The basic equations that define the functioning of the solar cell are given below.

$$J = J_L - J_0\left[\exp\left(\frac{qV}{nkT}\right) - 1\right]$$

$$V_{oc} = \frac{nkT}{q}\ln\left(\frac{J_{sc}}{J_0} + 1\right)$$

$$FF = \frac{J_{mp}V_{mp}}{J_{sc}V_{oc}}$$

$$Efficiency, PCE = \frac{J_{mp}V_{mp}}{P_{inc}} = \frac{FFJ_{sc}V_{oc}}{P_{inc}}$$

3.2.7 Quantum Efficiency (QE) Measurements

Quantum efficiency (QE) experiment explains the behavior of a solar cell at various wavelengths of the solar spectrum. External quantum efficiency (EQE) is the ratio of number of carriers collected to the number of incident photons per unit area, per unit time, while internal quantum efficiency (IQE) is the ratio of the number of carriers collected to the number of photons absorbed. A typical EQE curve of a solar cell shown in Figure 3.16.

When the light of different wavelengths is incident on a solar cell, shorter wavelengths with higher absorption coefficient get absorbed within the first few 100 nano meters, while the longer wavelengths penetrate deeper and generates carriers throughout the intrinsic layer. This property helps in understanding the interface/bulk problems. For nanocrystalline solar cells the measurement is done at zero bias and at a negative bias of -1 V. Placing the sample under a negative bias improves the electric field which increases the collection of the carriers. If QE ratio is high at lower wavelengths (400-500nm) then it is an indication of a very poor interface property in between p and i-layer. Similarly if QE ratio is high at higher wavelengths (800-900nm) then it is an indication of poor material property throughout the i layer in an n-i-p solar cell [106].

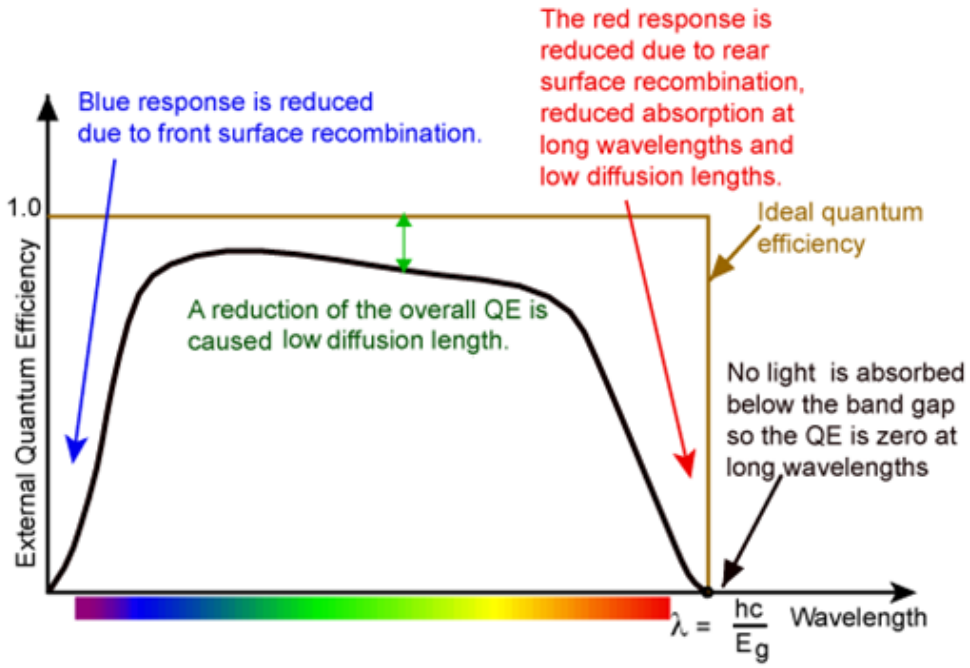

Figure 3.16 EQE curve of a solar cell [107]

Figure 3.17 shows the schematic diagram of the QE setup clearly showing all of the parts. The system consists of monochromator which uses a grating structure to emit a light of particular wavelength. The light from the monochromatic source passes through a chopper rotating at a frequency of 13.56 Hz. This AC beam is focused using a couple of lenses and mirror set-up to fall on either the sample or the reference photodiode. The reference photodiode is a standard silicon photodiode whose QE response is known. The current generated from the sample is converted into a voltage signal, and then detected by a lock-in amplifier, which is programmed to lock in on a frequency of 13.56 Hz. This helps in removing the noise from other electronic instruments in the vicinity. The samples are soaked in a DC light to fill the midgap states with photogenerated carriers, and pin the quasi fermi levels. Filters are used at 580nm, 700nm and 900nm to reduce noise from the lower harmonics. The wavelength emitted by the monochromator is varied and the signal is recorded.

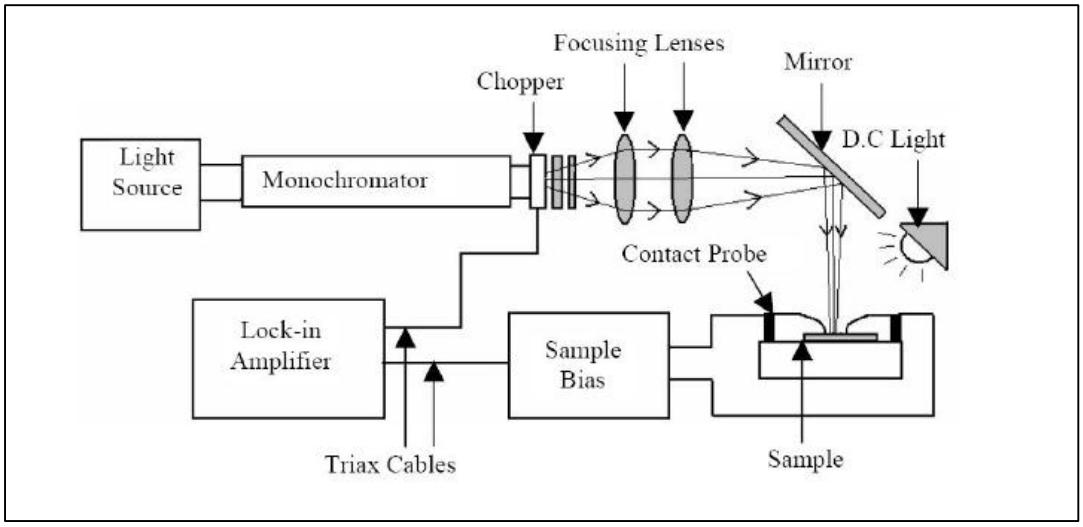

Figure 3.17 Schematic diagram of the Quantum Efficiency setup

To measure QE, spectral response of a reference photodiode is measured first. QE of the solar cell is then measured using the following equation.

$$QE_{cell} = QE_{ref} \frac{A_{ref}}{A_{cell}} \frac{V_{cell}}{V_{ref}}$$

where A_{ref} and A_{cell} refer to the area of the reference cell and solar cell, V_{ref} and V_{cell} refer to the signal measured across the reference cell and solar cell.

QE of a nc-Si:H solar cell is shown in Figure 3.18, and on the right axis is the ratio of the biased(-1V) to the unbiased QE. The ratio will help in detecting any collection problems at the interfaces. The integrated QE current can be calculated from the expression.

$$J_{sc} = \sum q.\phi.QE$$

where q is the basic unit of charge, ϕ is photon flux per unit area per second per unit wavelength interval. The unit wavelength interval used was 20nm. The integrated current should match with the current obtained from the IV setup. After the relative QE is found, the maximum QE is normalized to 0.9 and then plotted.

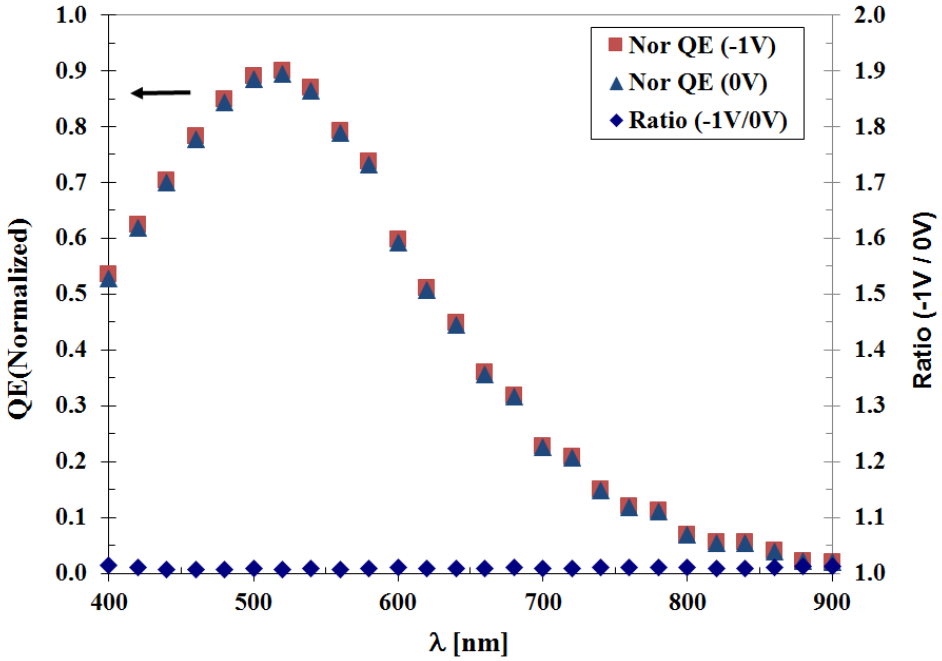

Figure 3.18 Quantum Efficiency of a nc-Si:H solar cell

3.2.8 Capacitance-Voltage (CV) Measurement

The capacitance-voltage (CV) measurement is an important experiment to estimate the defect density of a material. The experiment is first developed and modeled by Kimerling [108]. In a p+-n junction assuming the traps are uniformly distributed across the i-layer, the capacitance can be related to number of trap states by the following formula.

$$\frac{C}{A} = \frac{1}{2}\left[\frac{2q\varepsilon}{V+V_D}N(W)\right]^{\frac{1}{2}}$$

where C is the capacitance, A is the area of contact, V_D is the diffusion voltage and N(W) is the total space charge density at the edge of the depletion width. When $(A/C)^2$ is plotted against V gives a straight line with slope proportional to N(W). The space charge density N(W) comprises of all the traps that are responding to applied conditions such as applied bias, AC

frequency, and measurement temperature. At low reverse bias only the shallow states respond, while at higher reverse biases both the shallow and the deep states respond.

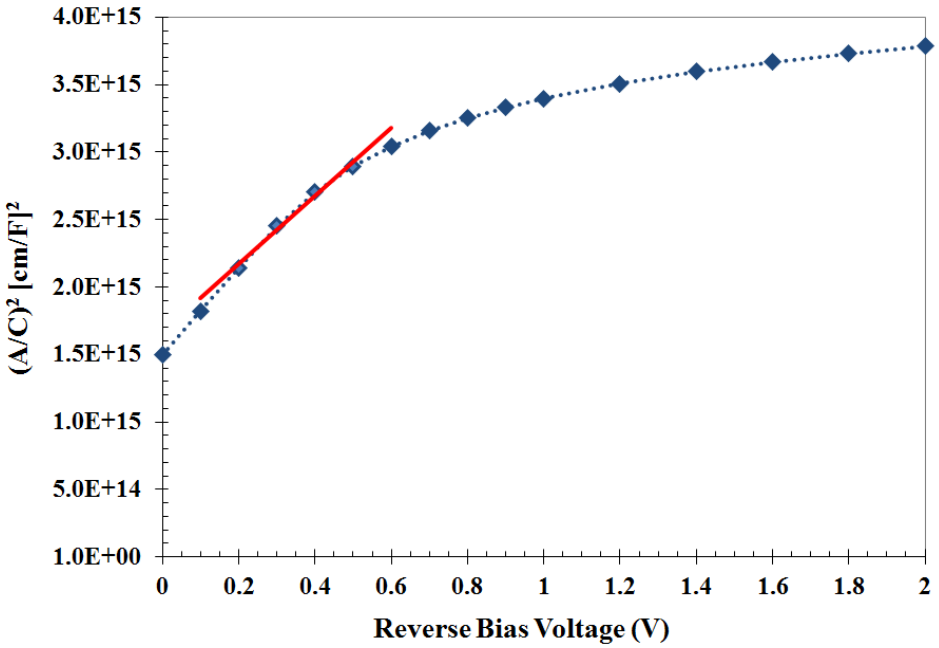

Figure 3.19 Low frequency CV measurement of a nc-Si:H solar cell

By choosing the right frequency, either shallow traps or the deep traps can be estimated. Low frequency CV measured at 100Hz for a nc-Si:H solar cell using Quadtech 1920 LCR meter is shown in Figure 3.19, and the slope is used to measure the defect density of the material. The thickness of the i-layer can be estimated using a high frequency CV measurement at 100KHz. As the reverse bias voltage is increased, the depletion width increases and saturates when the i-layer is completely depleted. This capacitance value after the saturation point can be used to estimate the thickness using the basic parallel plate equation

$$t = \varepsilon A / C$$

where t refers to the thickness of i-layer and ε is the dielectric constant of silicon. Figure 3.20 shows a plot of capacitance vs. applied reverse bias.

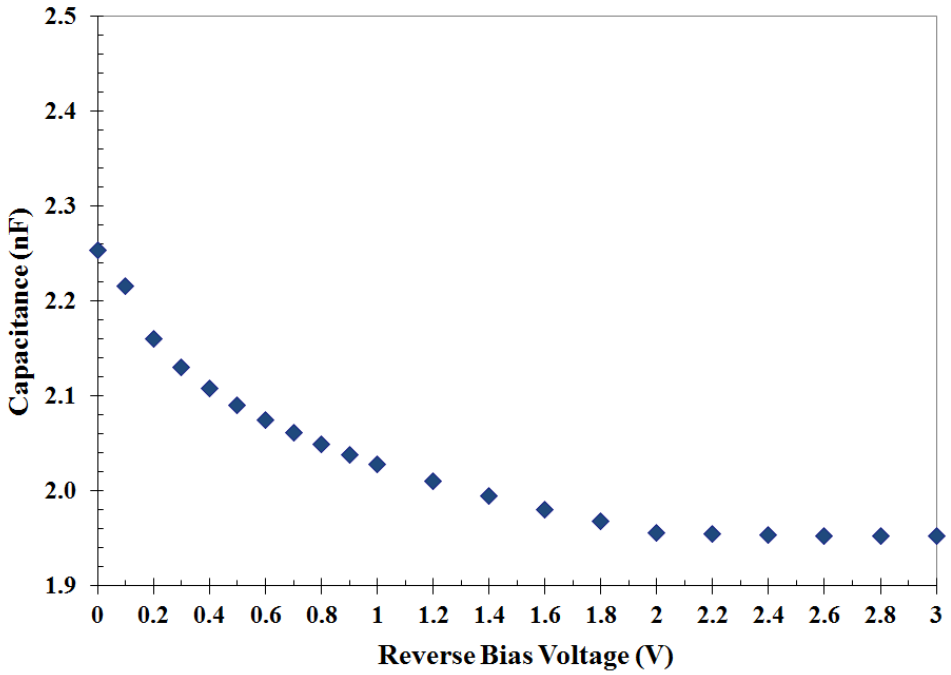

Figure 3.20 High frequency CV measurement of a nc-Si:H solar cell

3.2.9 Capacitance – Frequency (CF) Measurement

Capacitance versus frequency measurements are effective technique to study the defect profiles in thin film solar cells, as explained by Walter [109]. Traps deep in the band gap emit over a longer time than traps near the band edge. This principle is used to measure trap density by differential capacitance techniques. A high frequency capacitance measurement may only detect traps close to band edges and only the fast emitting traps will be detected. A measurement at a lower frequency may be able to reach deep into the bandgap and thus detect both the fast emitting and medium emitting traps. By differentiating the capacitance vs. frequency curve, traps can be profiled corresponding to their respective position from the band edge. The emission phenomenon is shown in Figure 3.21.

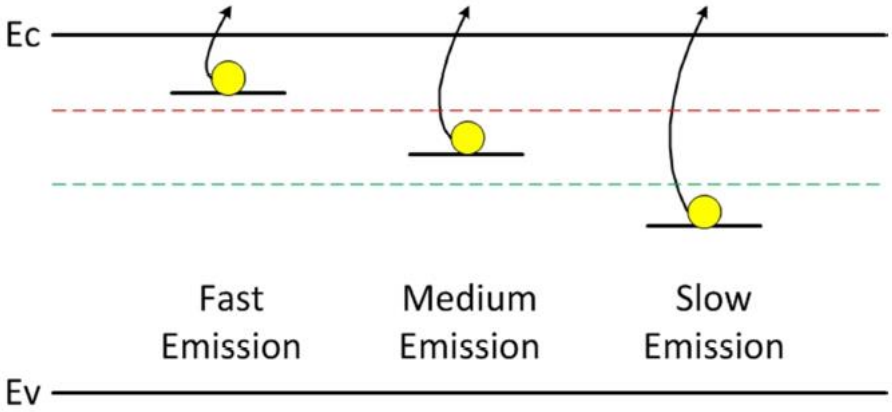

Figure 3.21. Schematic of emission phenomenon inside the bandgap [68]

From basic carrier conservation, the capacitance contribution of a single trap state can be calculated [109]. After integration over energy and space, the number of traps can be solved for

$$N_t(E_\omega) = -\frac{V_{bi}}{qw}\frac{dC}{d\omega}\frac{\omega}{kT}$$

where V_{bi} is the built in voltage, w is the width of the i-layer, k is Boltzmann's constant and T is the temperature. E_ω is the demarcation energy at which traps can respond to a given frequency, defined as

$$E_\omega = kT\ln(\frac{\omega_0}{\omega})$$

where ω_0 is the attempt to escape frequency of the material, is discussed in detail in the following section.

Defect profile of a solar cell can be obtained from CF measurements using the above two equations. CF measurement done on a nc-Si:H solar cell at room temperature and calculated defect profile is shown in Figure 3.22. It is observed that defects are peaking about 0.55eV which is the mid gap energy level of nc-Si with a band gap of 1.1eV [110].

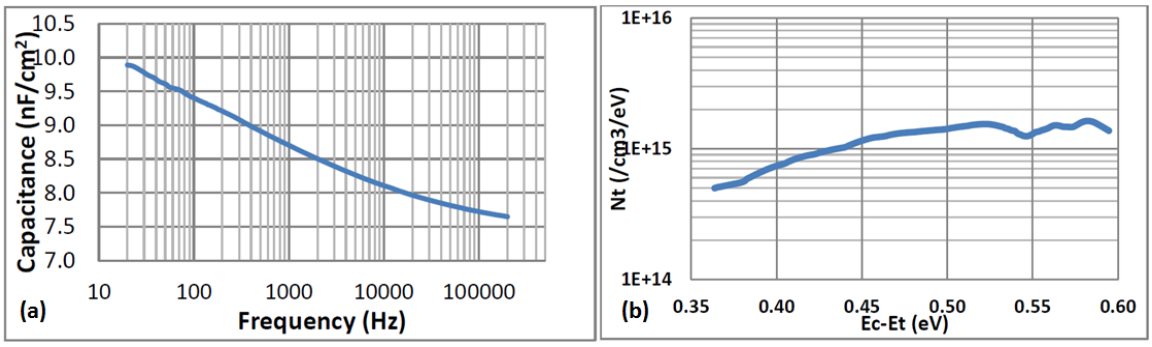

Figure 3.22 (a) Capacitance Vs Freq. (b) Defect Profile for nc-Si sample measured at room temperature [110]

3.2.10 Capacitance-Frequency vs. Temperature (CFT) Measurements

In order to evaluate the total defects in the material traps should be profiled from band edge to beyond midgap. To reach deep into the band gap either low frequency or high temperature is needed. It is shown that at 20Hz and 100C in nc-Si, the traps corresponding to 0.8eV below band edge will respond [111]. As the demarcation energy (E_ω) depends both on frequency and temperature, CFT measurements can be used to model the defects in the bandgap more efficiently.

CFT measurements were carried out on a custom built setup shown in Figure 2.23. Hioki LCR (1mHz – 200kHZ, 0.05% basic accuracy) was used, even though the LCRs have a rated measurement range of 1m to 200k HZ the usable range was often limited by the sample itself. High frequency data where possible inductance effects [112] and very low frequency data where leakage causes high dissipation values [113] were neglected. A continuous flow liquid nitrogen cryostat, controlled by a Lakeshore 331 temperature controller, was used to vary the sample temperature between 100 and 400K. Two platinum resistance temperature detectors (RTDs) contained within the cryostat head and one platinum RTD mounted on the sample surface were used to accurately track the cell temperature. The inset shown in Figure 3.23 shows organic solar cell mounted for testing. The sample sits directly atop the copper

cryostat head. Cryogenic rated grease, which solidifies at low temperatures, was used to improve thermal conductivity between the head and sample substrate. A simple wire probe, which is mimicked by the RTD to ensure an accurate temperature measurement, is connected to the top surface of the sample. Thick copper wire is used to make bottom contact and silver wire clamped to the top contact. The probe wires are wrapped around the side of the cryostat head and varnished in place to ensure they cooled to the set-point temperature.

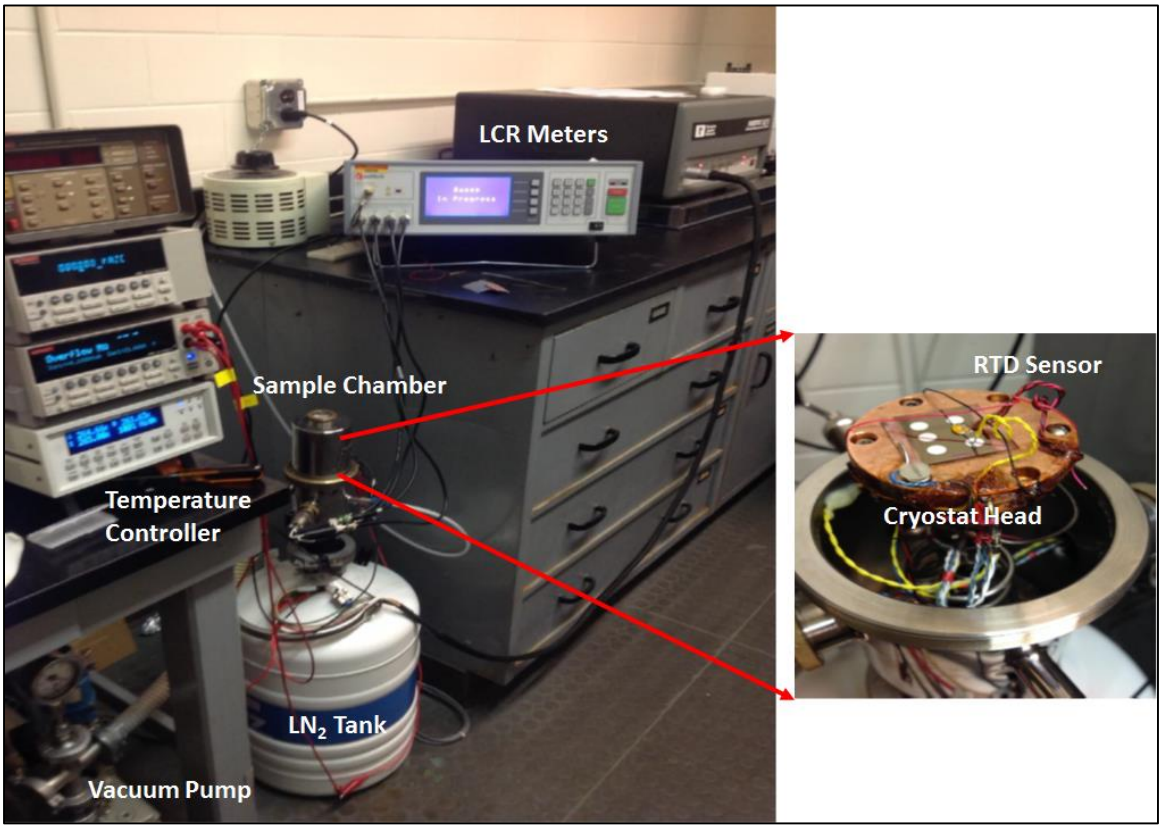

Figure 3.23 Experimental setup for CFT measurement. Stage is shown in inset and parts are labelled in the figure [114]

CFT measurements involve energy levels deep in the bandgap and their response, so carrier capture/emission rates must be considered. Assuming a thermally activated process, the emission rate of electrons trapped via defects within a semiconductor bandgap is given by,

$$e_n = N_c v_{th} \sigma_n \exp\left(-\frac{E_A}{kT}\right)$$

where N_c is the conduction band density of states, v_{th} is the thermal velocity, σ_n is the capture cross-section and E_A is trap activation energy [115, 116]. This is an Arrhenius equation, in which the emission rate is dependent on the activation energy, measurement temperature and the pre-exponential factor – ($N_c v_{th} \sigma_n = \nu_0$) also known as, attempt to escape frequency (ATE) [116]. It is very important to calculate ATE accurately to model the trap energy levels precisely.

Arrhenius plot of ln(e_n) versus *1/T* gives a straight line, with a slope which gives the trap activation energy (E_A) and an intercept gives the ATE (ν_0). This technique assumes that the pre-exponential factor is independent of temperature. However, $N_c \propto T^{3/2}$ and $v_{th} \propto T^{1/2}$ giving an inherent temperature dependence to ATE (ν_0). In that case, the prefactor is written as γT^2 where

$$\gamma = N_c v_{th} \sigma_n T^{-2}$$

and the emission rate is written as

$$e_n = \gamma T^2 \exp\left(-\frac{E_A}{kT}\right)$$

Temperature in square term is dominated by the exponential term and γT^2 value is most of the times very similar to ATE (ν_0) value. Thus, this temperature dependence is often neglected. But, the defect density results are estimated using both ways.

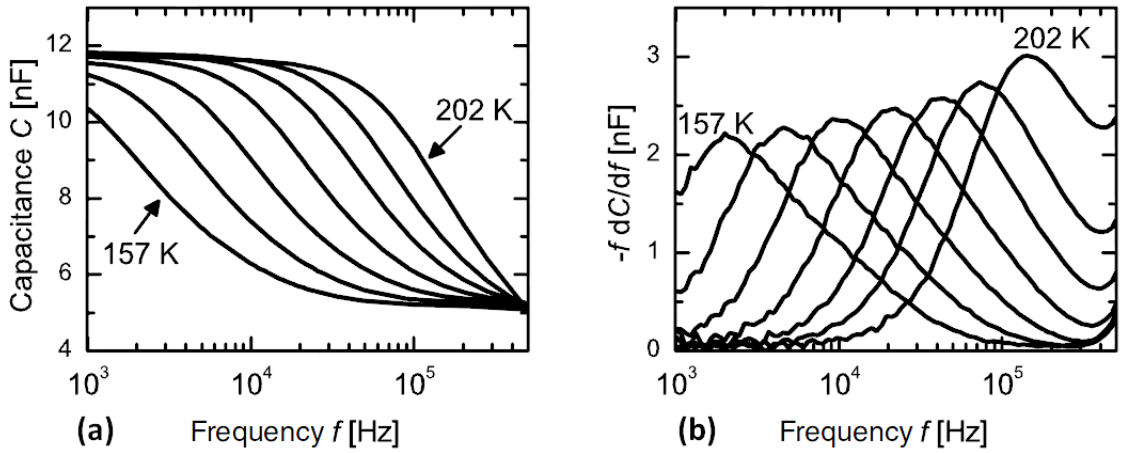

Figure 3.24 (a) Capacitance vs. Frequency, (b) Diffrential Capacitance vs. Frequency for different temperatures in a thin film solar cell [116]

The change in trap emission with a change in measurement temperature can be studied using capacitance measurements. By sweeping from high frequency to low frequency capacitance will increase as more energy states starts responding. Figure 3.24a shows CF curves at different temperatures. The steps in this graph corresponds to peaks in the differential capacitance (*–FdC/dF*) graph shown in Figure 3.24b. As illustrated in Figure 3.25, the plot of frequency at which these peaks occur versus 1/T will follow Arrhenius behavior. The slope of this straight line gives the activation energy (E_A) and intercept gives the capture cross-section σ_n. The ATE (ν_0) value can be calculated from the capture cross-section (σ_n). Finally, using the *–FdC/dF* differential and the calculated ATE (ν_0) value defect profile can be modeled across the band-gap.

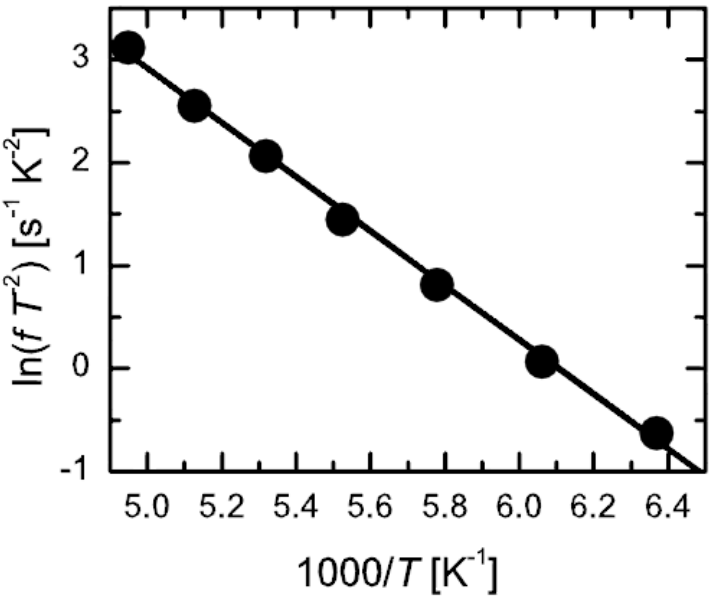

Figure 3.25 Arrhenius plot of the differential capacitance peak frequencies for different temperatures [116]

CHAPTER 4. RESULTS

This chapter gives a detailed discussion on defect density, transport properties and their relationship to impurities and grain size in nc-Si:H and nc-SiGe:H solar cells.

4.1 Film Properties

Nanocrystalline Ge;H and SiGe:H films were grown using PECVD using Hydrogen, Silane and Germane as precursor gases. These depositions were performed at different pressure, temperature and dilution ratio to study the grain growth and mobility. Intrinsic films are grown on stainless steel for measuring crystallinity and grain size, for devices i-layer is sandwiched between n+/p+ layers. The device structure is shown in Figure 4.1. Aluminum contacts were made using thermal evaporation.

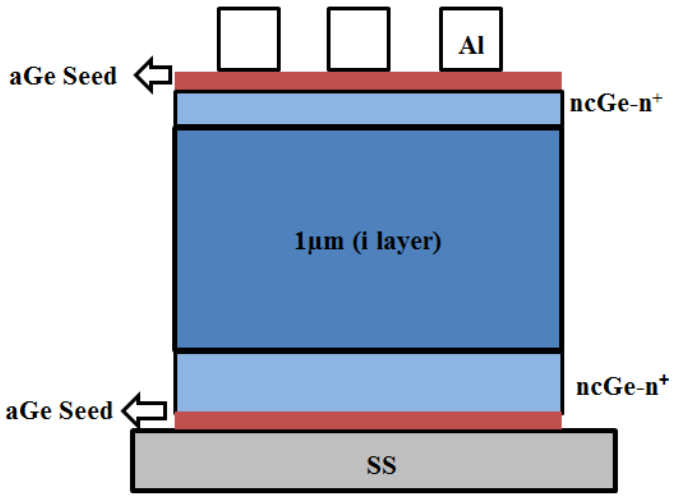

Figure 4.1 Detailed n+-n-n+ device structure

The devices were annealed at 150°C for 45-60 minutes to allow Aluminum to punch through any thin oxide layer formed on the top n^+ layer. Further the samples are electrically

annealed by passing 500mA of current for 10-15 minutes for reducing the contact resistance and thereby improving the Ohmic contact of Aluminum.

4.1.1 Grain Growth

Raman spectroscopy of a typical PECVD nanocrstalline Ge:H film grown at 900mT, 300°C using Hydrogen, Germane mixture is shown in Figure 4.2(a). A sharp crystalline peak at ~300cm^{-1} and amorphous shoulder at ~285cm^{-1} are observed. Crystalline to amorphous ratio of 4:1 is obtained. The X-ray spectrum for the same film is in Figure 4.2(b), showing <111> peak at 28.5° with a grain size of 26nm and <220> peak at 45.5° with a grain size of 62nm. Higher grain size can be achieved either by higher pressure or high temperature.

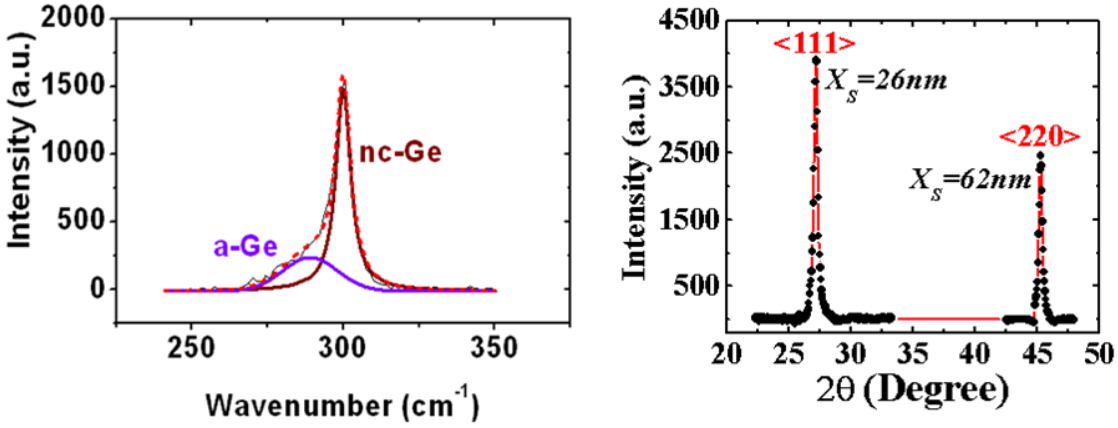

Figure 4.2 (a) Raman spectrum for PECVD nanocrstalline Ge:H film grown at 900 mT, 300°C (b) X-ray diffraction spectrum for the same film

The grain size versus deposition pressure for a nc-Ge:H films grown at 300°C shown in Figure 4.3(a). Both <111> and <220> grain size increases with the deposition pressure, but <220> grain size increases significantly suggesting <220> as preferred orientation for crystal growth. In Figure 4.3(b), grain size versus deposition temperature for nc-SiGe: H films grown at 900mT was shown. <111> grain size decreases slightly with temperature whereas <220>

grain size increases with the temperature. So the preferred orientation is still <220> in SiGe:H films as well.

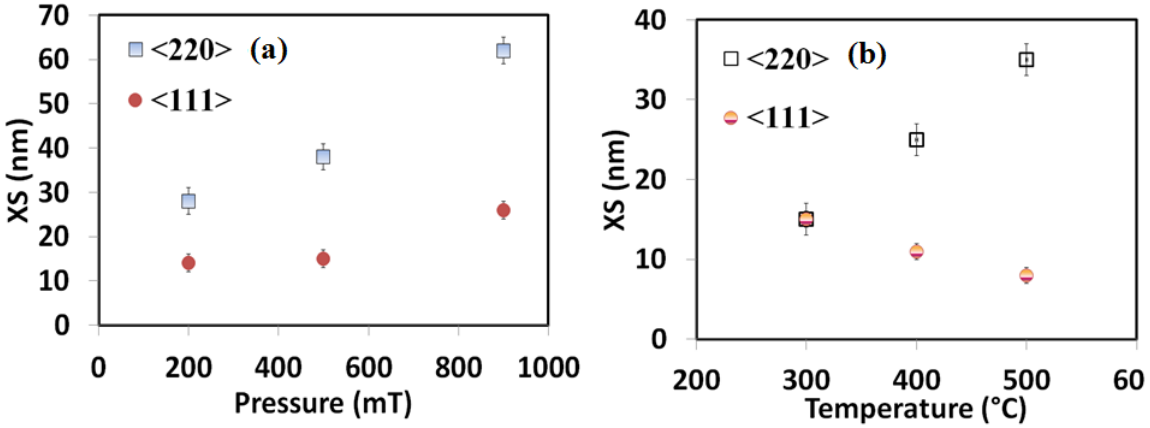

Figure 4.3. (a) Grain size of nc-Ge:H films grown at 300°C, (b) Grain size of nc-SiGe:H films grown at 900mT

4.1.2 Mobility Measurements

Figure 4.4(a) shows the current versus voltage curve for n^+-n-n^+ Ge:H device at a measurement temperature of 25°C. Corresponding Raman and X-ray spectrums were shown in earlier figures.

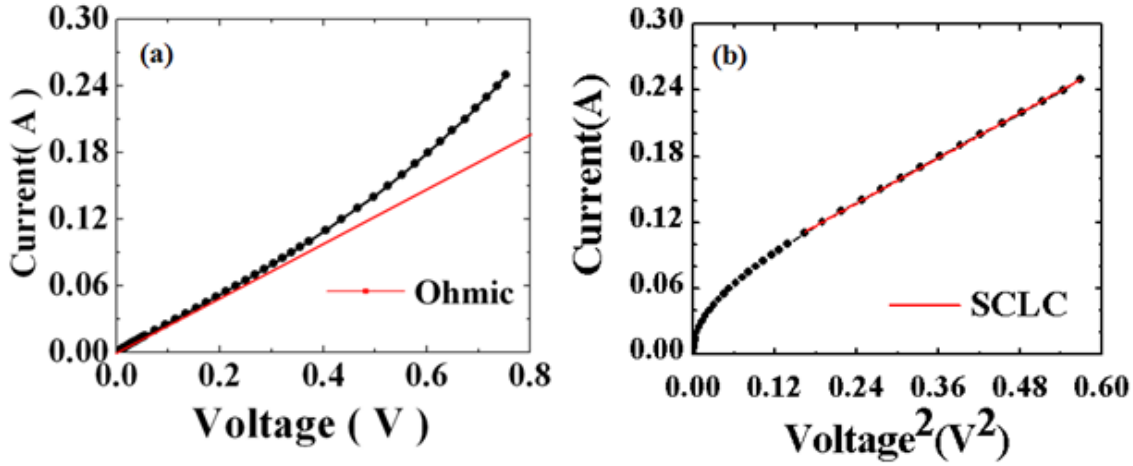

Figure 4.4. (a) Plot of current versus voltage showing Ohmic region, (b) Plot of current versus voltage^2 showing SCLC region

This figure shows two typical regions, initial linear region and then nonlinear region after $V_{SCLC.}$ Figure 4.4(b) shows I vs. V^2 curve at a measurement temperature of 25°C. It shows linear behavior in SCLC region. From the slope, the mobility measured to be 2.1 cm^2/V-s. Using this mobility value and the slope from Ohmic region of Figure 13a, carrier concentration was deduced to be 5E14 and Fermi level is ~0.25eV below conduction band. All the calculated values are shown in Table 1.

Table 4.1 Calculated values of different parameters using the graphs in Figure 4.4

Parameter	***Value***
Resistivity	5E3 Ω.cm
Mobility	2.1 cm^2/V-s
V_{SCLC}	0.28 V
Carrier Concentration	5E14 cm^{-3}
E_C - E_F	0.25 eV

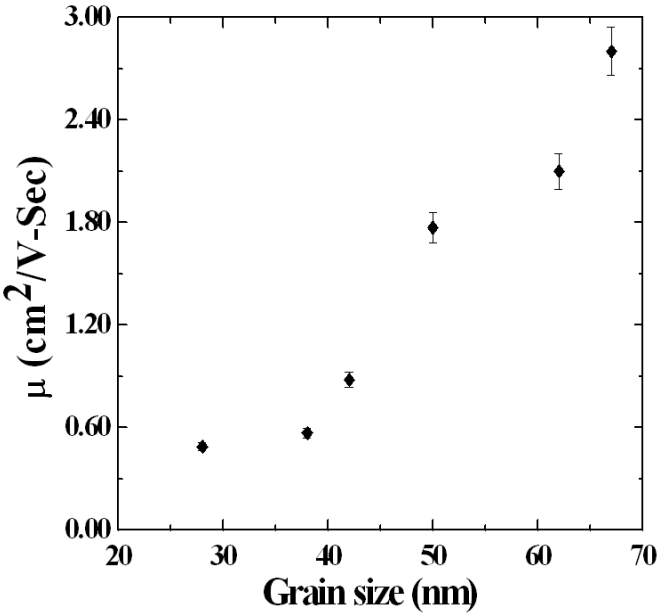

Figure 4.5. Electron Mobility vs. <220> Grain size

Figure 4.5 shows the mobility derived from SCLC versus the <220>grain size measured from X-ray diffraction. Mobility increases with the grain size, with the smaller mobility being deposited at lower pressures. As explained earlier lower pressure leads to smaller grains and lower mobility. For the largest grain size (~70nm) which is deposited at 900mT pressure, the measured mobility is 2.8 cm^2/V.sec.

4.1.3 Control of Crystallinity

Crystallinity of the samples is measured using Raman spectroscopy by 488nm Ar-ion laser. Crystallinity of the sample should be monitored as a function of thickness, to achieve better device properties. This is because in traditional devices, increasing the film thickness tends to get more crystalline, and the number of microvoids (by grain boundaries) increases, leading to deterioration in film properties. There are different ways to control the crystallinity as explained in section 3.1.2 such as Hydrogen profile, power grading or superlattice structures. Typical Raman spectroscopy of a nc-SiGe:H film is shown in Figure 4.6.

Films were grown with different thicknesses starting from 0.2µm to ~1µm while measuring the Raman spectroscopy at each stage. Desired crystallinity is achieved at each thickness by either changing the gas dilution or adjusting the power. Uniform crystallinity is achieved through Hydrogen profile, power grading as well as superlattice structures. Figure 4.7 shows the crystallinity as a function of i-layer thickness in different scenarios. The results show that the crystalline to amorphous ratio is maintained across a thickness of 1.4 µm with different techniques.

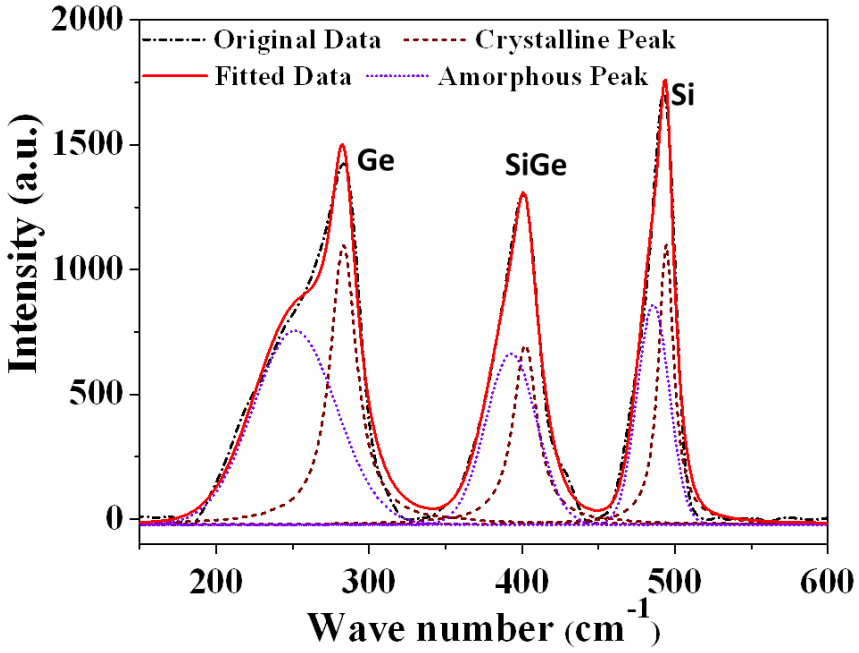

Figure 4.6 Raman spectrum for PECVD grown nc-SiGe:H film

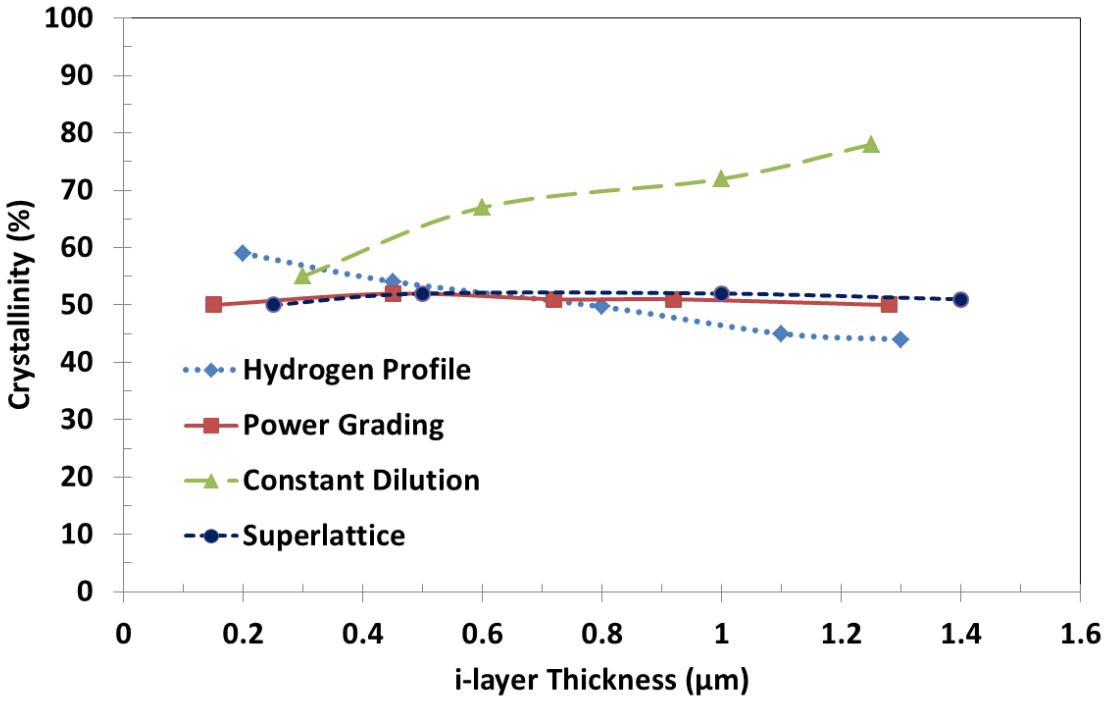

Figure 4.7 Crystallinity vs. i-layer thickness in nc-SiGe:H film

4.1.4 Elemental Analysis

EDS is used to do the elemental analysis of nc-SiGe:H films. Atomic percentage of Si and Ge are calculated for different SiH_4 and GeH_4 gas flows. At a constant flow of 2.1 sccm of SiH_4, as GeH_4 flow is increased from 0 to 1.1 sccm in steps, it is observed that more Germanium is incorporating into the material. From Figure 4.8, it is observed that Ge content in the solid state of the film is much higher than the gas phase ratio. This is due to lower dissociation energy of GeH_4, which implies that Ge can easily be deposited with higher deposition rate as compared to Si.

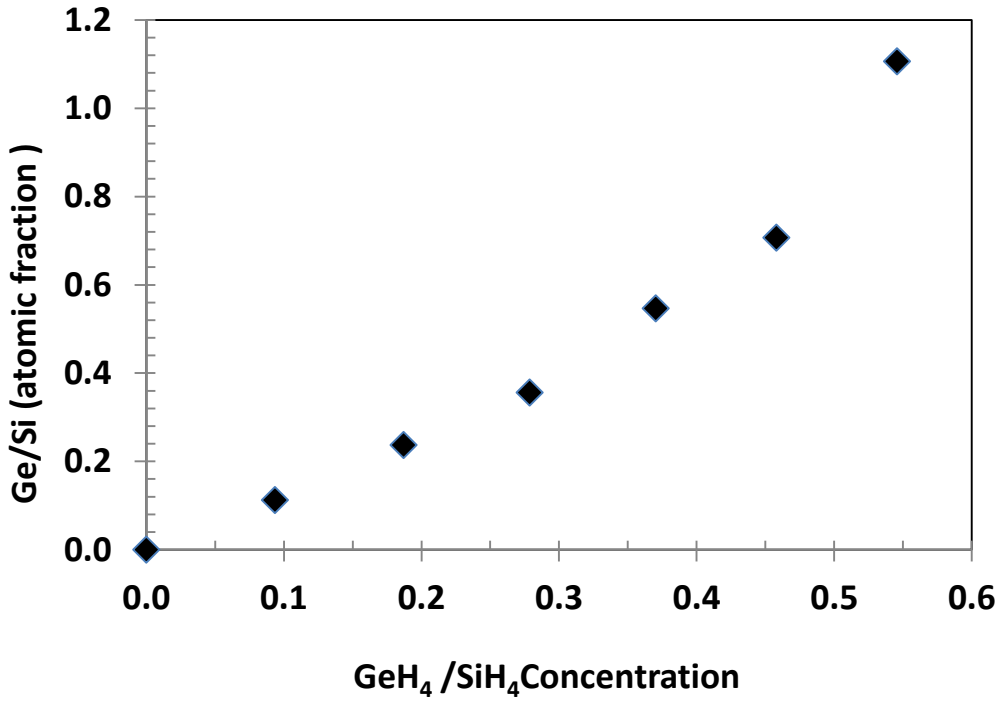

Figure 4.8 Germanium content for different gas flows in nc-SiGe:H devices

4.1.5 Absorption Spectra

Optical absorption is a direct indicator of photovoltaic nature of a materials and varying bandgap to achieve desired absorption is a common practice. In nc-SiGe:H bandgap can be engineered by changing the germanium content in the material. Figure 4.9 shows the variation

of the absorption coefficient of the material on increasing the germanium content. The composition of nc-SiGe:H strongly dependent on the deposition conditions such as SiH_4/GeH_4 ratio, power, temperature and pressure. As the Ge content increases in nc-SiGe:H, bandgap decreases which results in higher absorption.

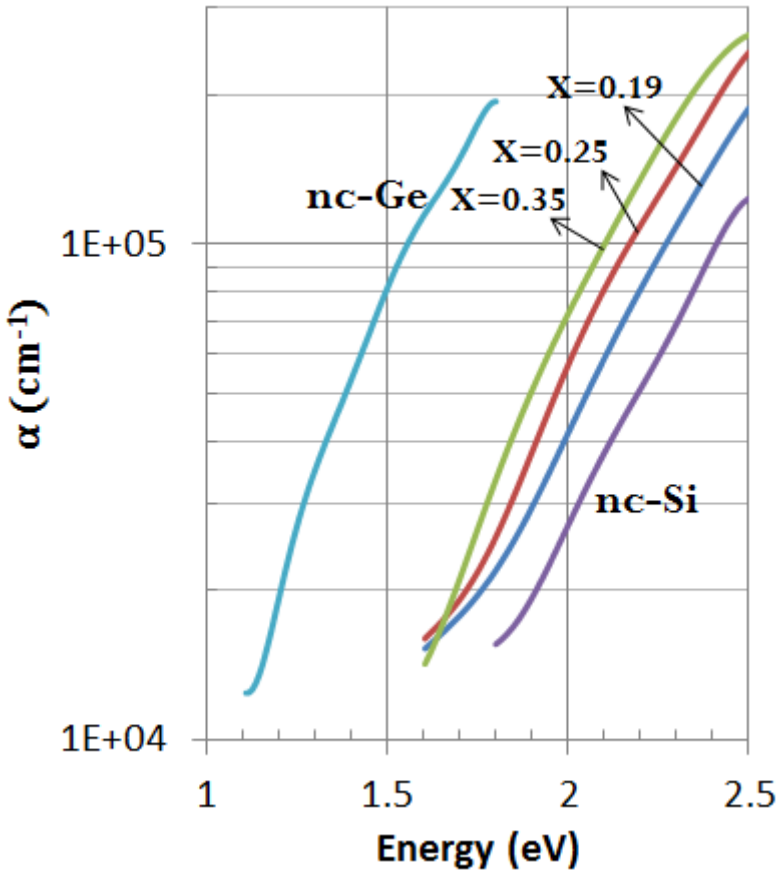

Figure 4.9 Increase in absorption coefficient on increasing the Germanium content in nc-$Si_{1-x}Ge_x$:H films

4.2 Device Structure and Characterization

Figure 4.10 shows a typical nc-SiGe:H solar cell device structure, in order to make nc-SiGe:H device, the first layer will be similar to nc-Si:H device i.e. 0.3µm thick a-Si n+ layer. A thin layer of a-Si is deposited as seed layer followed by thin layer of nc-Si and then gradually graded to nc-SiGe:H with required Germanium content. P+ layer consists of nc-SiGe:H with

the similar amount of Ge as i-layer in order to match the bandgap for smooth transition. The interface layers are very important. If the interface layers are not properly matched that might cause a kink or a barrier in the band diagram results in bad collection. Final p+ layer is followed by anti-reflecting coating of sputtered ITO. The final band diagram obtained for the device is shown in Figure 4.11.

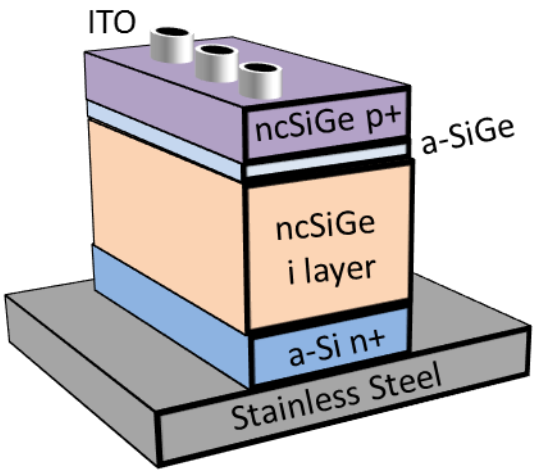

Figure 4.10 nc-SiGe:H solar cell Device Structure

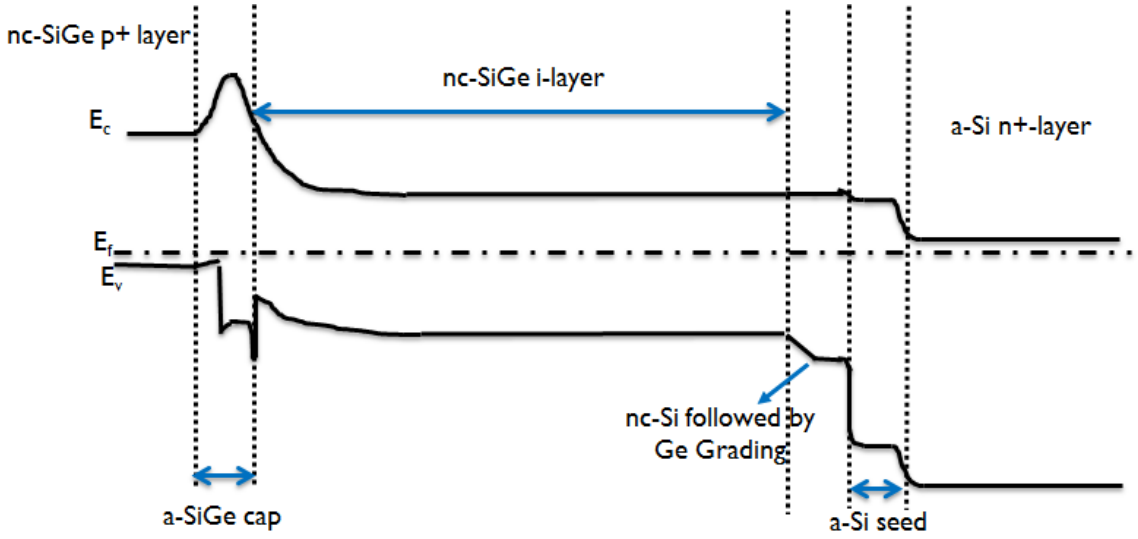

Figure 4.11 Band diagram of nc-SiGe:H device.

4.2.1 Hydrogen Profile

Hydrogen profile is one of the ways to fabricate device with constant crystallinity across the thickness. Hydrogen dilution is decreased as a function of deposition time. Initially high Hydrogen flow is used to achieve the nucleation and systematically decreased across i-layer. Devices were made at 100mT, 250°C with a gas mixture of Hydrogen, Silane and Germane. Hydrogen is graded from 75sccm to 55sccm, keeping the Silane (2.1sccm) and Germane (0.4sccm) at constant flow.

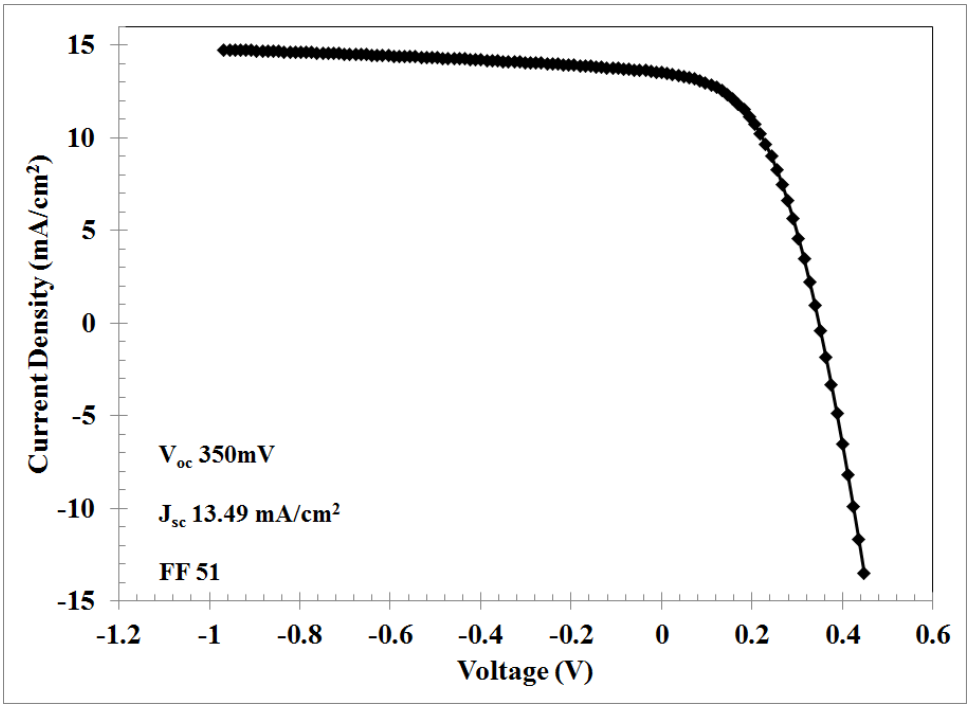

Figure 4.12 JV Characteristics of Hydrogen Profile nc-SiGe:H device

The JV characteristics of nc-SiGe:H solar cell with X_{Ge} of 20% can be seen in Figure 4.12. The device performance is improved from the previous work at our lab by Saripalli et. al [117]. Figure 4.13 compares the relative QE of a nc-SiGe device with and without external bias. It was observed that the QE ratio between -1V bias and 0V bias was less than 1.1 which

shows that the band gaps were well graded at both p-i and i-n interfaces and there are no potential barrier anywhere in the device.

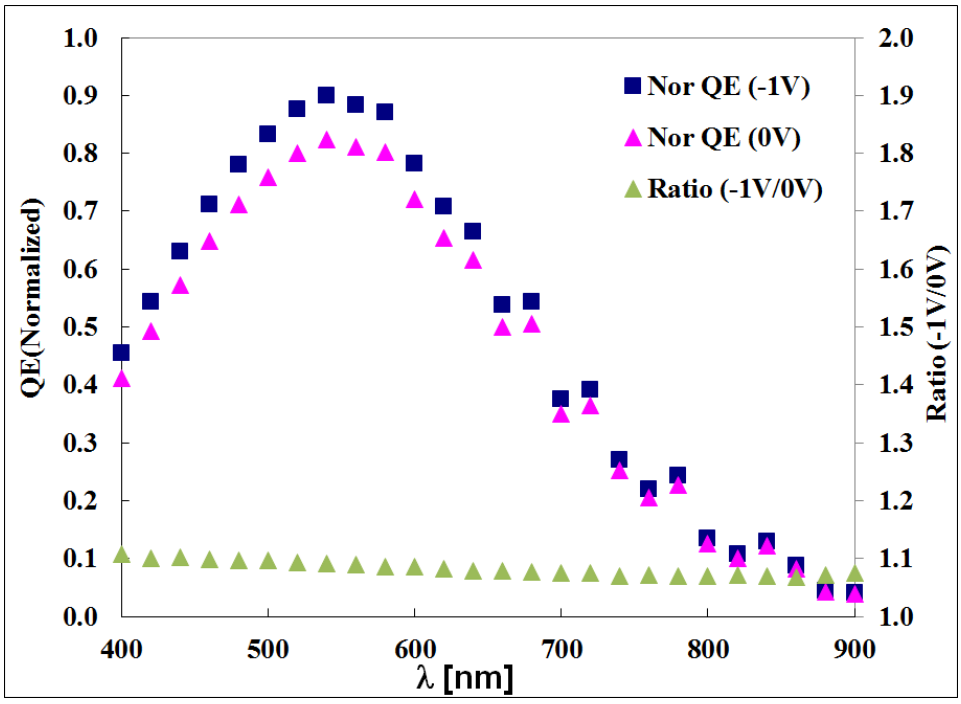

Figure 4.13 QE performance of Hydrogen Profile nc-SiGe:H device

4.2.2 Power Grading

It is also possible to control the crystallinity of the ncSiGe:H film by RF power. Nanocrystalline material becomes more crystalline on increasing the power so it can be controlled by decreasing the power as the film grows. This method not only helps to control the growth but to reduced ion-bombardment which further helps to improve the film quality. Initially high power is needed for nucleation and formation of grains, after that crystallinity should be maintained. It needs amorphous tissue for passivation and to decrease defects at grain boundaries. Power is graded from 20W to 15W gradually while keeping Hydrogen, Silane and Germane flow constant at 100mT, 250°C. Figure 4.14 is the IV curve of nc-SiGe:H solar cell (X_{Ge}=20%) and the performance is similar to Hydrogen profile device. The QE

performance of the same solar cell is shown in Figure 4.15, and QE ratio (-1V/0V) is observed to be less than 1.1 and flat.

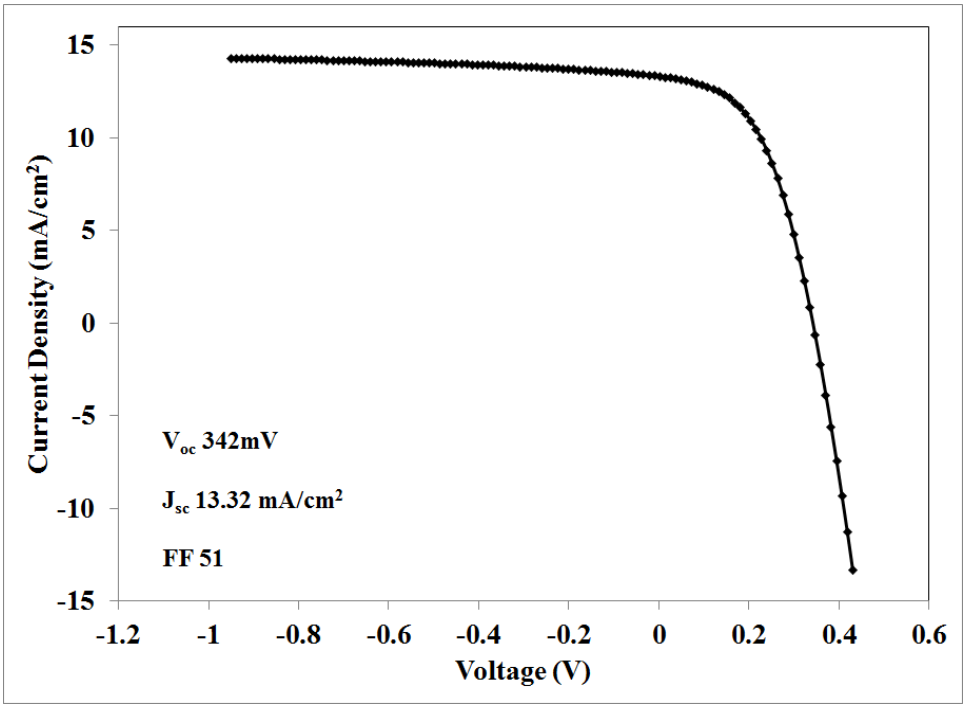

Figure 4.14 JV Characteristics of Power graded nc-SiGe:H device

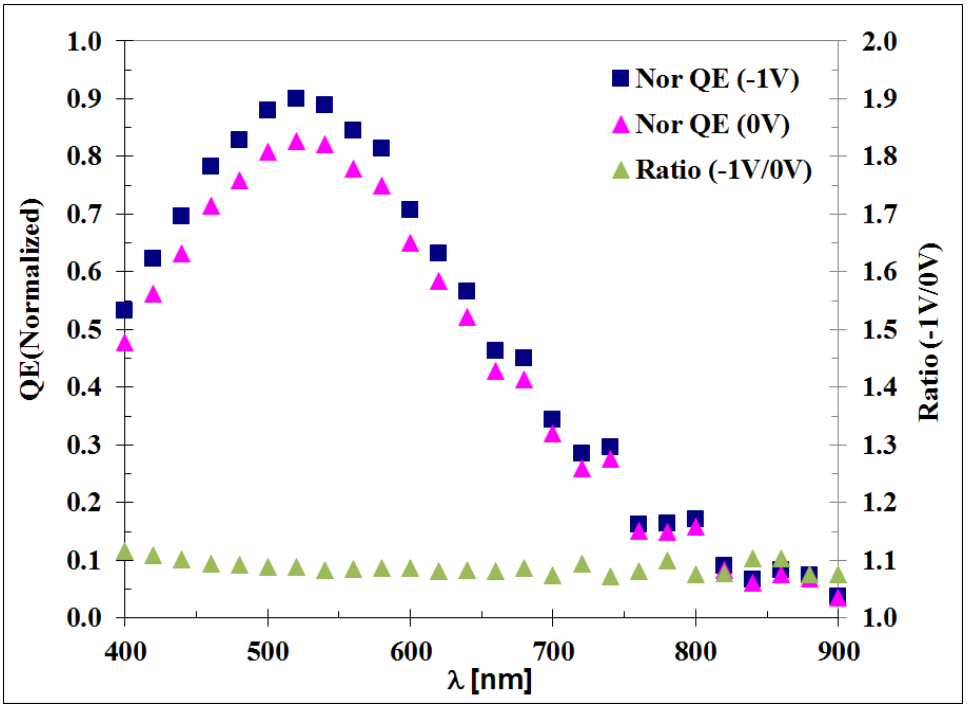

Figure 4.15 QE performance of Power graded nc-SiGe:H device

4.2.3 Device Performance

Further studies are done by changing Germane to Silane ratios to see the effect of Germane addition on fundamental properties of solar cell. Figure 4.16 shows the illuminated JV curves for samples prepared using varying germane:silane ratios and Ge atomic percentage is mentioned in the legend parenthesis. A surprising result is that the short-circuit current actually decreases as the germane content in the gas phase increases. This is in spite of the fact that the Ge to Si ratio in the solid phase is increasing, thereby implying a smaller bandgap material for higher germane flows.

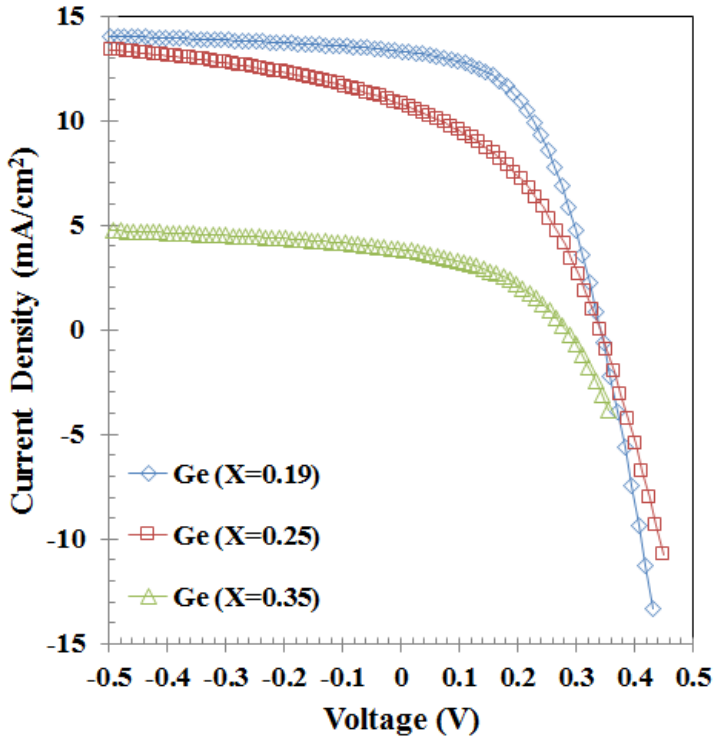

Figure 4.16 JV curves and for nc-SiGe:H solar cells with varying Ge content

The explanation for this behavior is provided by studying quantum efficiency data, shown in Figure 4.17. It is clear from the QE data that there is a drastic reduction in QE for short wavelengths when significant amounts of germane is added to the input gas mixture. This

can be ascribed to poor collection of electrons being generated near the p-n interface by light of shorter wavelengths, i.e. to a drastic reduction in electron diffusion length. This could be a result of the n-type intrinsic layer changing to a p-type, presumably due to Ge defects absorbing electrons from the oxygen induced donor states [85].

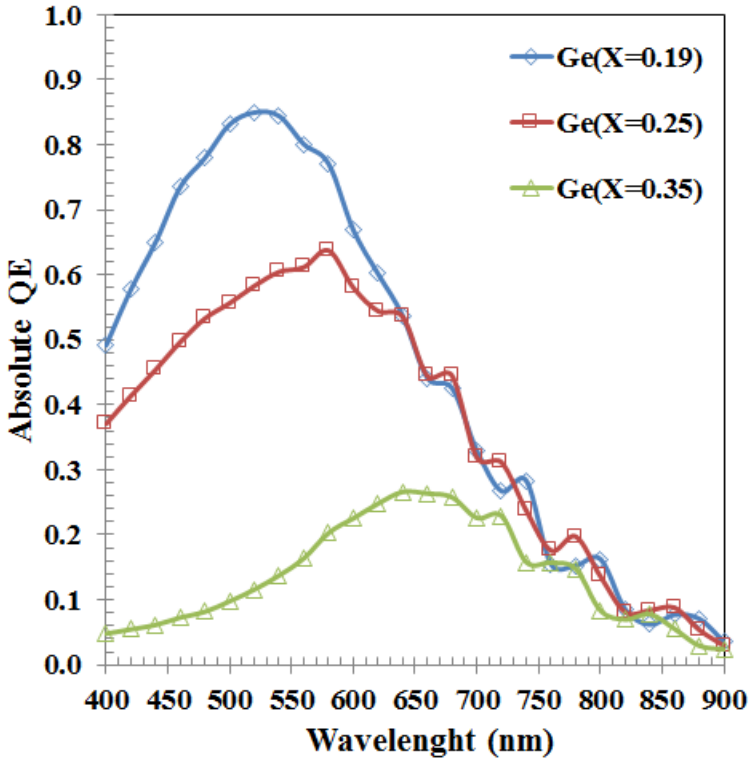

Figure 4.17 Abs. QE vs. Wavelength for nc-SiGe:H solar cells with varying Ge content

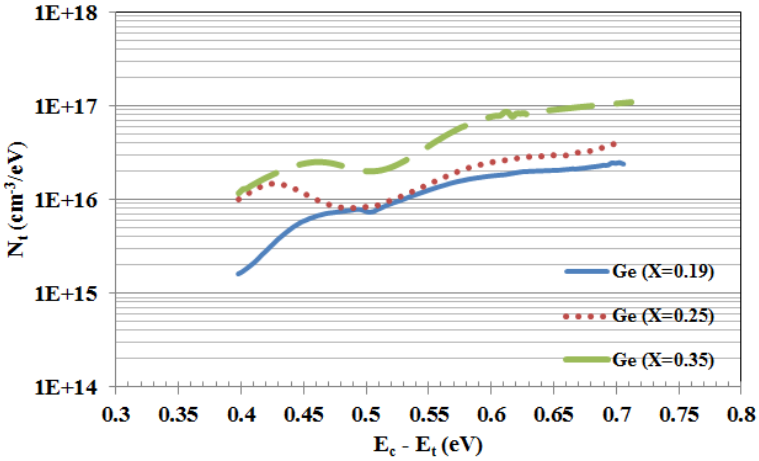

Figure 4.18 Calculated defect density vs. energy below the conduction band for varying Ge content

Indeed, there appears to be a significant increase in defect density when Ge content increases. See Figure 4.18 for data on defect density vs. energy for varying German:Silane flow rates. Data analysis is tabulated in Table 4.2.

Table 4.2. Device Parameters for nc-SiGe:H solar cells for different Ge content

Device	GeH_4/SiH_4 flow	Ge (atomic %)	Voc (mV)	Jsc (mA/cm^2)	FF	Defect Density (cm^{-3})	QE(900nm) (0.2V/0V)
1-8893	0.18	35	280	3.84	41	2.5E16	0.56
1-8898	0.28	25	341	10.8	41	1.7E16	0.62
1-8894	0.37	19	342	13.3	51	6.1E15	0.87

Higher Ge content results in higher absorption, which further should have improved the short circuit current. But instead short circuit current decreases with Ge content and defects are increasing with Ge content. To overcome the deleterious effects of additional Ge on both defect density and QE, defects should be compensated and carrier collection should be improved. In order to compensate for the apparent p-type doping by deliberately introducing ppm levels of phosphorus in the intrinsic layer by adding ppm levels of phosphine to the gas mixture during growth.

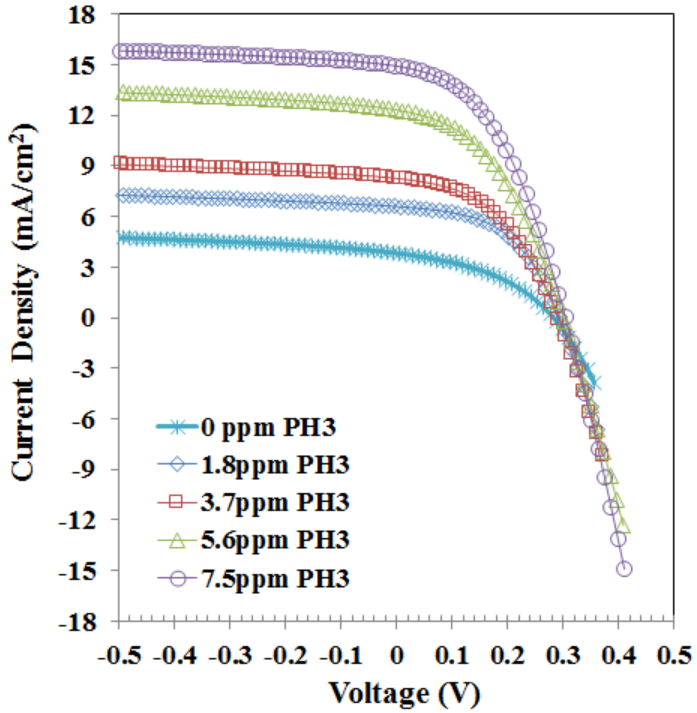

Figure 4.19 JV curves and for nc-SiGe:H solar cells with (X_{Ge}~0.35) for varying PH_3 flow rates

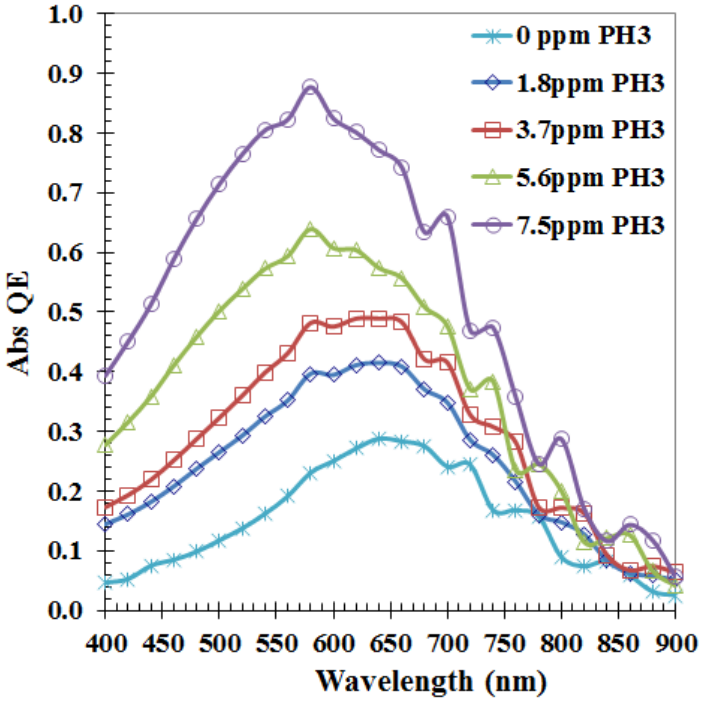

Figure 4.20 Absolute QE vs. Wavelength for nc-SiGe:H solar cells with (X_{Ge}~0.35) for varying PH_3 flow rates

The results for JV curve are shown in Figure 4.19 for various values of PH_3 for a fixed Ge/Si ratio of in the gas phase (X_{Ge}~0.35). Clearly, adding PH_3 significantly improves the short-circuit current in the solar cell. The corresponding QE curves are shown in Figure 4.20, and they clearly show an improvement in QE at short wavelengths, compared to the QE curves shown in Figure 4.17, thus showing that the poor electron collection efficiency for photons which are absorbed near the p-intrinsic layer interface has been overcome. The corresponding change in total defect density as a function of PH_3 flow is shown in Figure 4.21, thus confirming that addition of ppm levels of PH_3 serves to reduce the defect density in nc-SiGe:H intrinsic layers, probably by compensating the defects caused by Ge addition.

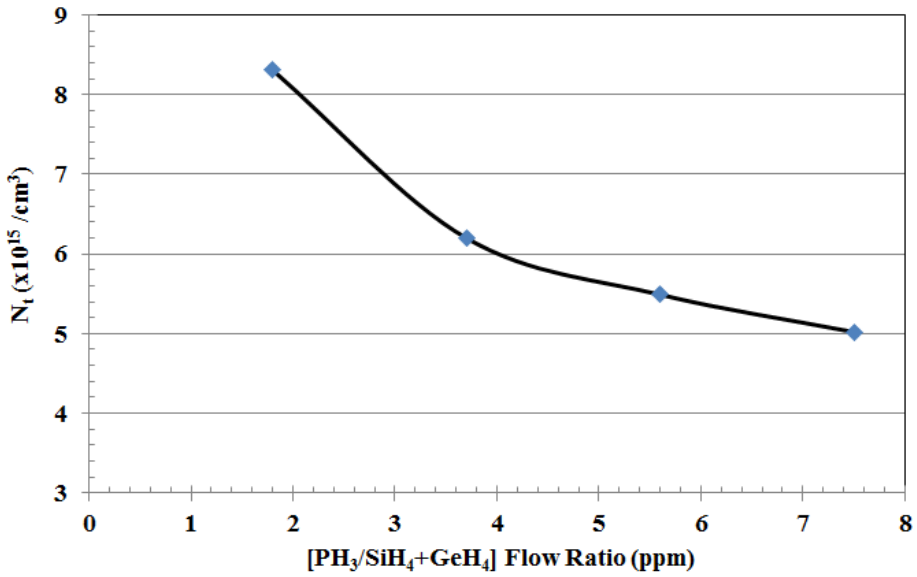

Figure 4.21 Total defect density as a function of PH_3 flow rate

From the above the results, it is observed that by adding appropriate PH_3 flow during growth defects can be compensated and electron collection can be improved. JV curves for the devices prepared using varying ratios of GeH_4/SiH_4 flow along with optimum ppm levels of PH_3 are plotted in Figure 4.22, which clearly shows that increasing Ge content leads to higher short-circuit currents. One consequence of increasing Ge content should be increasing the QE

in the infrared region of the spectrum because of decreasing bandgap. When the materials are properly compensated with P during growth, the QE does increase in the infrared region, as shown in Figure 4.23, in contrast with results from previous work by Matsui et al. [75].

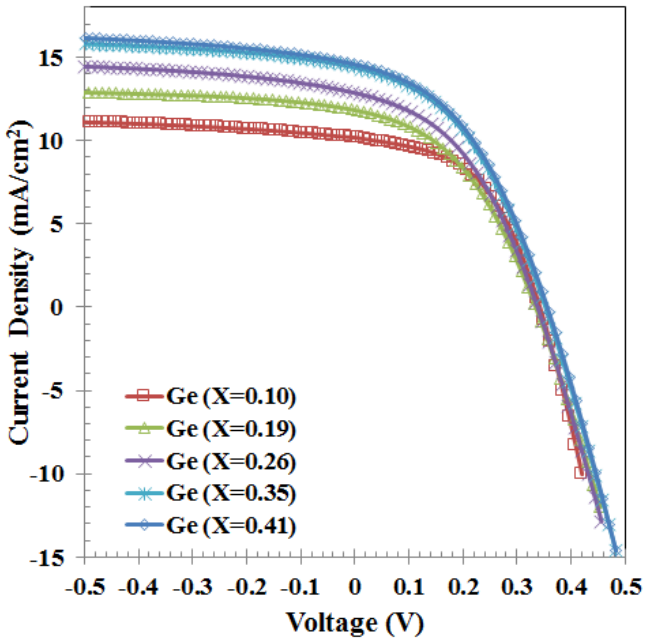

Figure 4.22 JV curves for nc-SiGe:H solar cells with varying Ge content with optimum PH_3 flow

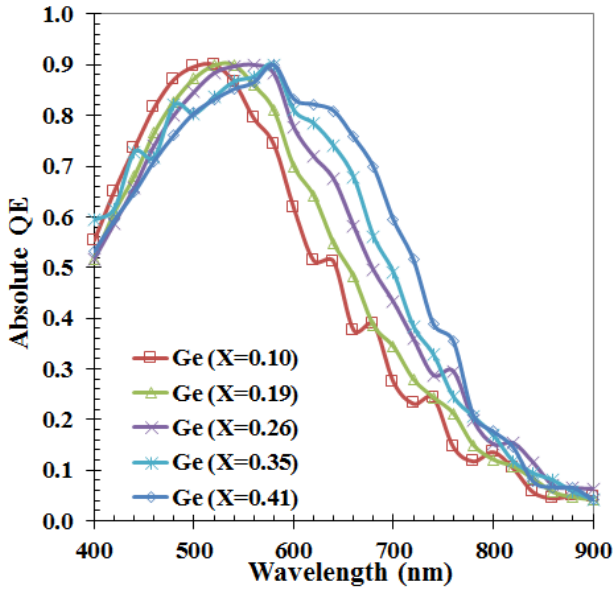

Figure 4.23 Abs.QE vs. Wavelength for nc-SiGe:H solar cells with varying Ge content with optimum PH_3 flow

Figure 4.24 shows the results for defect density in (Si,Ge) devices with uncompensated intrinsic layers as a function of Ge content , as well as the influence of adding compensating PH_3 to the intrinsic layer. Clearly, the defect density is also reducing upon compensation with ppm levels of PH_3.

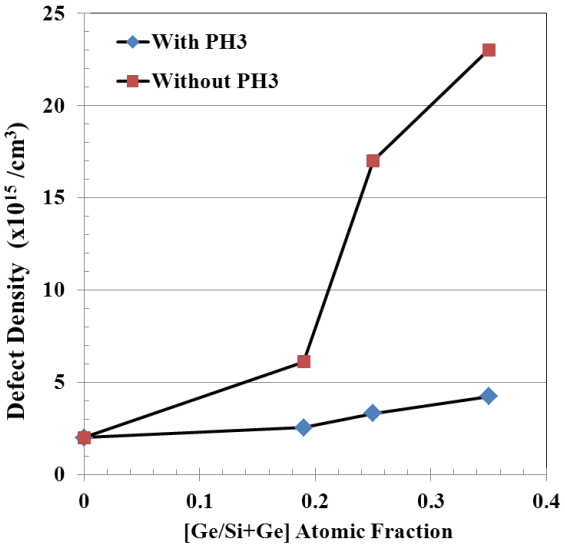

Figure 4.24 Total defect density as a function of Ge content

This is an important result because it shows how to get higher currents using nc-(Si,Ge) as the intrinsic layer in nanocrystalline solar cells. This result may be of some use in increasing the efficiency of thin film Si tandem junction solar cells.

4.3 Defects in Solar Cells

The performance of thin film solar cells is strongly dependent on defects present in the material. These defects create deep trap levels in the bandgap, which decreases the lifetime of the carriers and reduces the QE of solar cells. To understand the device physics of a solar cell, it is important to know the properties of defects such as defect density, defect profile and physical origin. The experimental techniques explained in section 2.2 are used extensively to estimate the defects in solar cells.

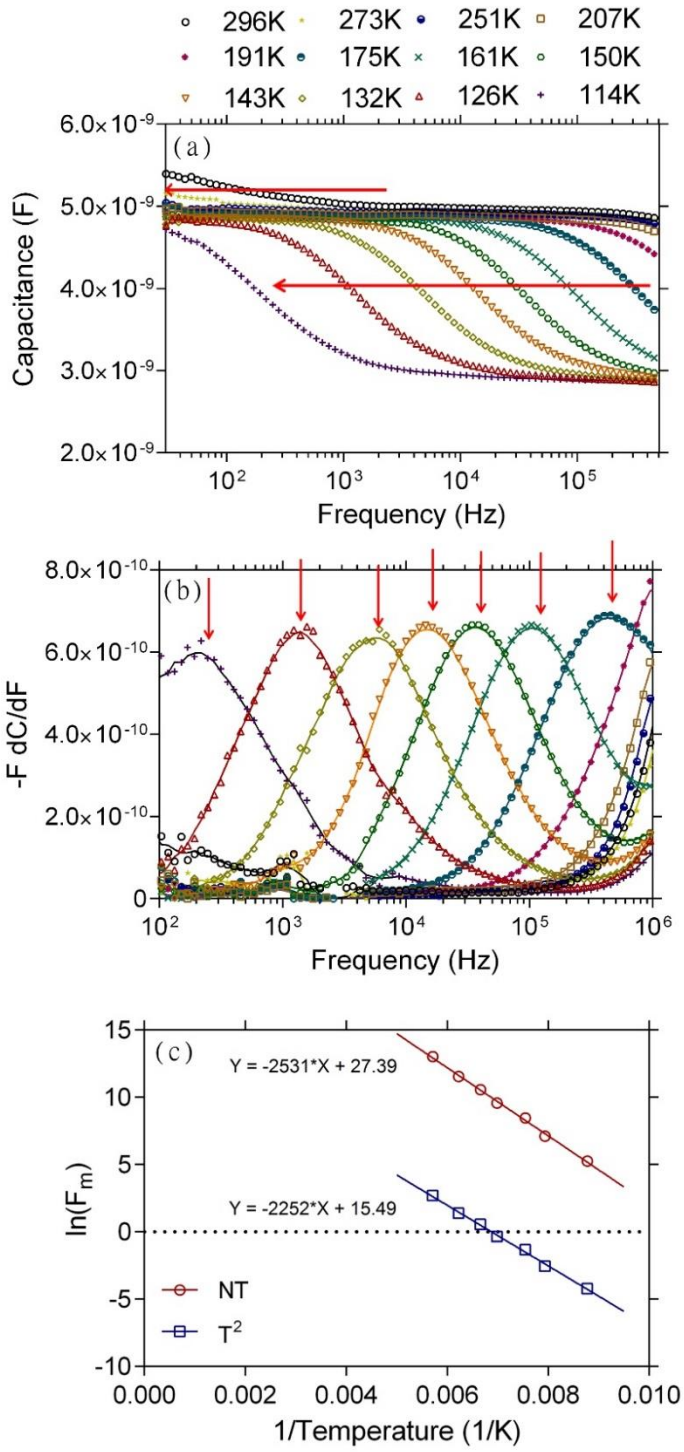

Figure 4.25 (a) CFT data for a-Si:H solar cell. The red arrows indicate the Arrhenius shift of the trap states with lowering temperatures. (b) Differential capacitance curves at different temperatures. Arrows indicate emission peaks. (c) Arrhenius plot of the differential capacitance peak frequencies.

4.3.1 Validation using a-Si:H Solar Cells

Amorphous silicon (a-Si) is a widely studied material for thin film solar applications. Even with high absorption coefficient and simple fabrication, main bottleneck is the high defect density. The a-Si:H soalr cells are known to have an ATE in the range of $1x10^{11}$-$1x10^{13}$ Hz [118-120], so the CFT setup was benchmarked using a-Si:H solar cells. CFT data, differential capacitance data and Arrhenius plot are shown in Figure 4.25. From the Arrhenius plot, average ATE value was found to be $1.6x10^{12}$ Hz which in the range mentioned above. This validates the experimental setup and the results used to calculate the defect profile in rest of the solar cells.

4.3.2 Defect Density Profile of nc-Si:H Solar Cells

Application of CFT technique to model defects in nc-Si:H solar cell is discussed in this section. Defect density is measured for standard nc-Si:H solar cells deposited on stainless steel substrates using PECVD. The crystallinity of the intrinsic layer is maintained by hydrogen profiling which gradually reduces the hydrogen dilution over the thickness. The typical growth temperature was 250°C and the pressure was 100 mT.

Figure 4.26a shows the CFT data for nc-Si:H solar cell. As the temperature is decreased from the room temperature (300K), a clear shift in the capacitance-frequency spectrum is seen. At lower temperatures, trap emission rates are slow and deep states only respond below 1 kHz. At low enough temperatures (≤130K) freeze-out is reached and the geometric capacitance is seen at higher frequencies. The completed CFT data shows three distinct regions of increasing capacitance. First step in capacitance is from geometric capacitance ~2.5nF at lower temperatures. This step represents the response of the free carrier density and a change in the capacitance from geometrical thickness to depletion width. Second step is seen from ~2.5nF

to ~2.75nF at moderate temperatures, representing the response of a deep defect band and a shift in capacitance. Third and final step beyond 2.75nF is seen in the lower frequencies for temperatures higher than 250K, representing the inclusion of deeper defect states near the midgap. Two clear sets of peaks are seen in the differential capacitance curve (Figure 4.26b) and shift accordingly with the changing temperature. The larger peaks correspond to the geometric capacitance step from the initial response of the free carrier density. This peak is expected to have a thermal activation energy of the Fermi-level (E_F). The smaller peaks correspond to the 2.5nF to 2.75nF shift, a deep defect band. A distinct peak for the yet deeper states beyond 2.75nF is not seen in this frequency range. The frequency at which these peaks occur is the emission rate of the trap at that energy level. These peak frequency versus 1/T is plotted in Figure 4.26c. Data assuming no temperature dependence as well as a T^2 temperature dependence of the pre-exponential factor are shown in this plot. As expected, a straight is revealed by the semi-log plot. Table 4.3 summarizes the derived parameters and the values are average of four devices. Thermal velocity (v_{th}) = 10^7 cm/sec and $N_c = 10^{19}$ cm^{-3} was assumed for these calculations.

Table 4.3 Summary of the calculated ATE and other parameters in nc-Si:H solar cell

Activation Energy, E_a	194 meV	352 meV
ATE, ν_0	1.1×10^{12} Hz	1.2×10^{12} Hz
Pre-factor, Υ	1.0×10^{7} Hz K^{-2}	4.5×10^{6} Hz K^{-2}
Capture cross-section, σ_n^*	1.1×10^{-14} cm^2	1.3×10^{-14} cm^2

The carrier response band is centered on 194 meV, which is good agreement with Fermi-level (196 meV) calculated from the CV measured dopant density (5.0×10^{15} cm^{-3}). Assuming no temperature dependence, the ATE was determined to be ~1.0×10^{12} Hz. The next band was found to have an a activation energy of ~350 meV and again, an ATE of ~1.0×10^{12} Hz. Information on the deeper states could not be determined using this method.

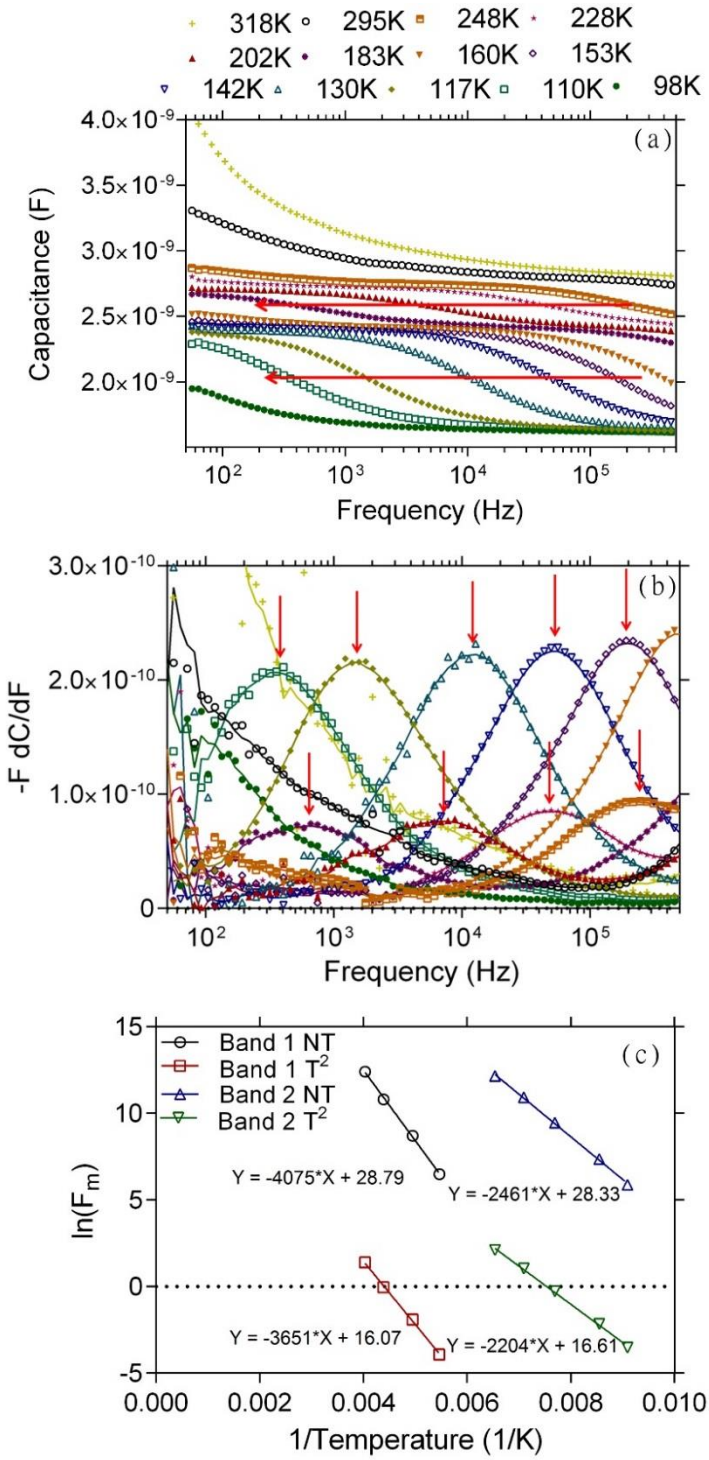

Figure 4.26 (a) CFT data for nc-Si:H solar cell. The red arrows indicate the Arrhenius shift with lowering temperatures. (b) Differential capacitance curves. Arrows indicate emission peaks. (c) Arrhenius plot of the differential capacitance peak frequencies versus 1/T. Both no temperature dependent (NT) and T^2 temperature dependent (T^2) data is shown for both sets of peaks.

However, as mentioned above, from the differential capacitance curves and calculated ATE (ν_0) value defect density profile can be modeled across the band-gap. The resulting defect profile is shown in Figure 4.27. The contributions from each of the three capacitance steps described above can be seen. Initial peak from the carrier response around 200 meV with density of $1.0x10^{16}$ cm^{-3} eV^{-1} leads into a sharp Gaussian defect around 350 meV with a density of $2.0x10^{15}$ cm^{-3} eV^{-1} as well as a broader distribution of deep defects extending towards the midgap around 550 meV with a density of $1.0x10^{15}$ cm^{-3} eV^{-1}. The temperature independent ATE of $1.0x10^{12}$ Hz gives good overlap in the defect profile measured by different temperatures which gives substantiation to the obtained value and indicating that the states near the midgap share this same value.

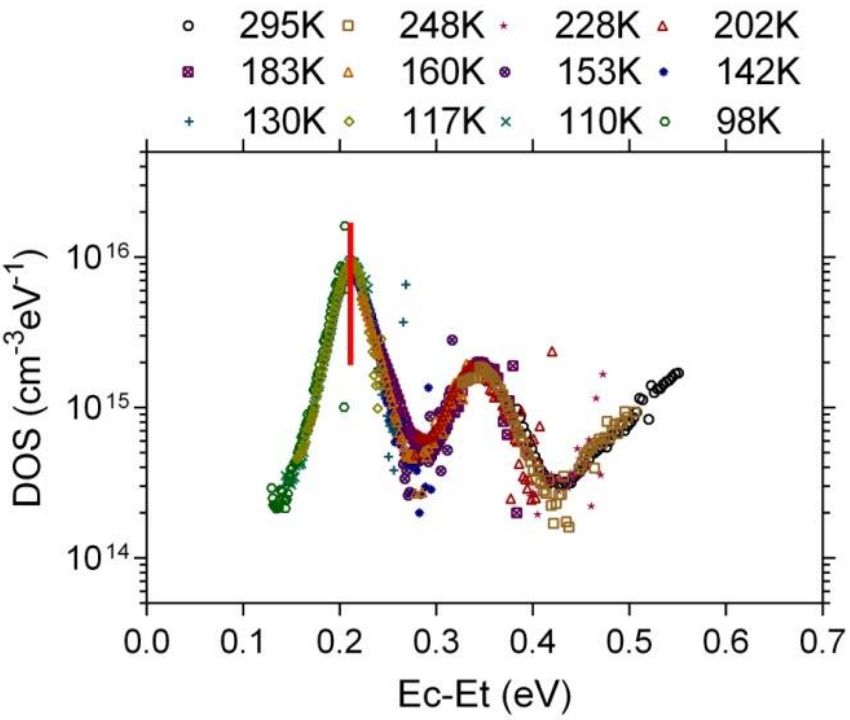

Figure 4.27 Estimated defect density profile of nc-Si:H solar cell below the conduction band. The solid line marks the Fermi-level.

4.3.3 Defect Density Profile of nc-SiGe:H Solar Cells

Defect density profile of nc-SiGe:H solar cells are discussed here in detail. As explained in section 4.2.3, defect density increases with Ge concentration in nc-SiGe:H solar cells. It is very important to know the energetic distribution of defects and ways to counter those defects. Effective evaluation of defects require thorough and careful investigation using CFT measurements. To accurately model the defects in nc-SiGe:H solar cells, ATE value is calculated first using the standard CFT setup.

CFT data for nc-SiGe:H solar cell with Ge content, $X_{Ge} = 0.35$ is shown in Figure 4.28a. Similar to nc-Si:H solar cell there is a clear shift in the capacitance-frequency spectrum as the temperature is decreased from the room temperature (300K). The capacitance response for temperatures below 200K is identical to nc-Si:H, however higher temperature response is entirely different. Steady increase in capacitance values at temperatures beyond 250K suggests Ge inclusion causes deep defects which is shown earlier in Figure 4.18. Two sets of peaks are observed in differential capacitance curves corresponds to the two bands in CFT data. The peaks are depicted with arrows in Figure 4.28b.

The smaller peaks correspond to the geometric capacitance step from the initial free carrier response with an activation energy of the Fermi-level (E_F). In nc-SiGe:H solar cells, the larger peaks correspond to deep defect trap due to Ge content. The frequency at which these peaks occur is plotted versus 1/T in Figure 4.29. Activation energy of both set of peaks are calculated from the slope of the Arrhenius plot and also ATE as well as pre-exponential factor with T^2 temperature dependence are computed from the intercept. Table 4.4 summarizes the derived parameters and the values are average of three devices.

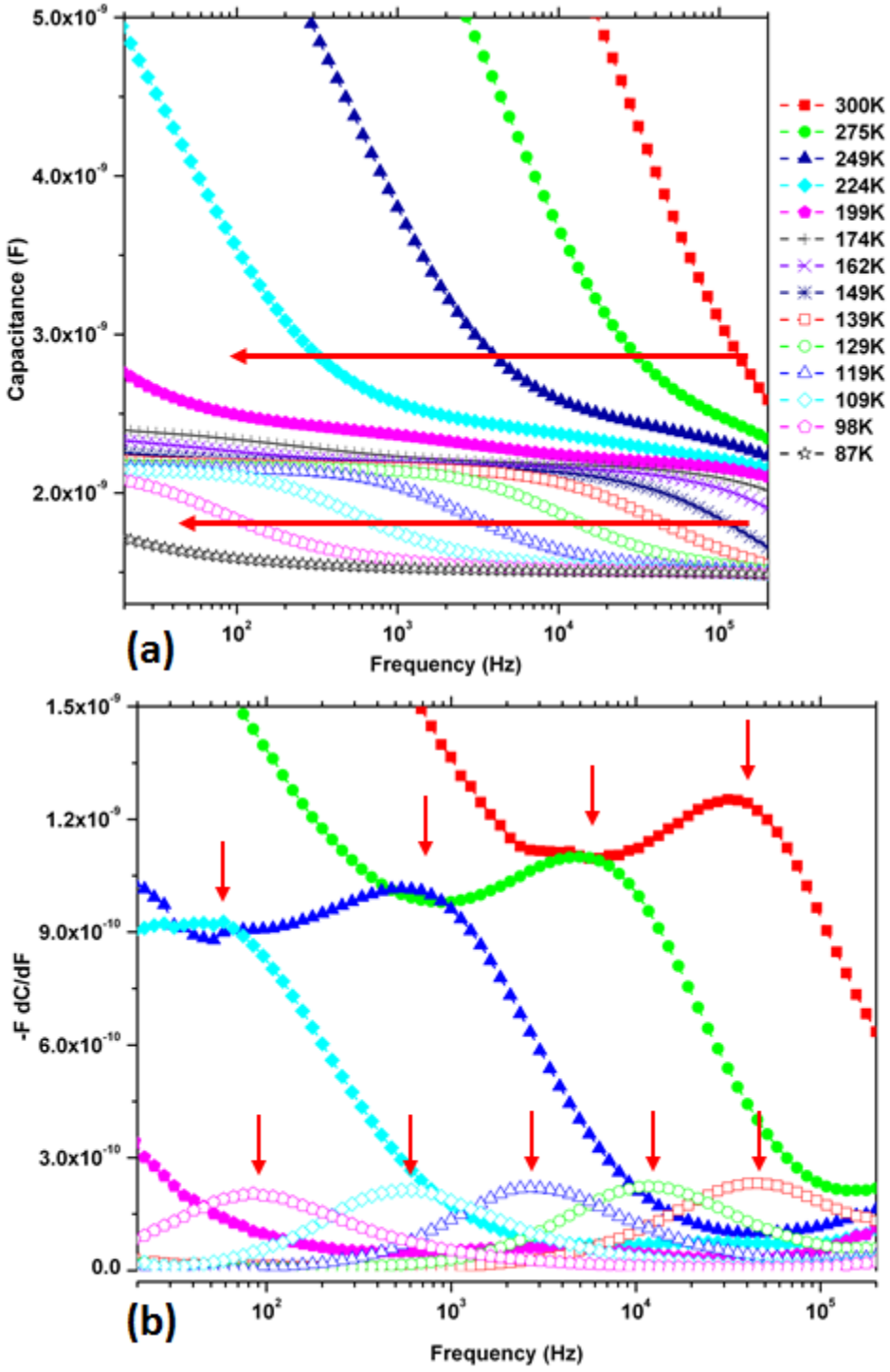

Figure 4.28 (a) CFT data for nc-SiGe:H solar cell (X_{Ge}=0.35). The red arrows indicate the capacitance shift due to two different trap levels. (b) Differential capacitance curves. Arrows indicate emission peaks.

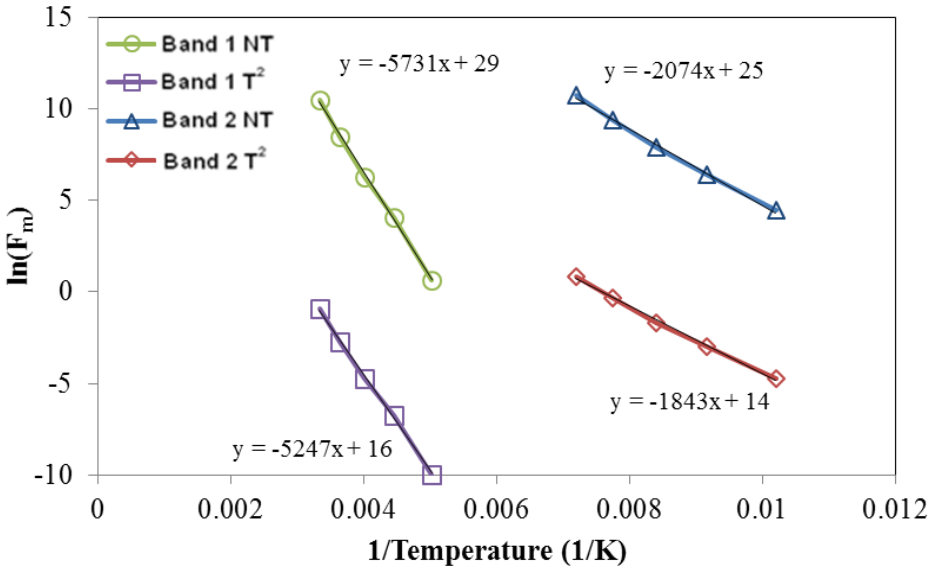

Figure 4.29 Arrhenius plot of the differential capacitance peak frequencies versus 1/T for nc-SiGe:H solar cell

The carrier response band is centered on 190 meV, similar to nc-Si:H solar cell. But the ATE value calculated to be ~5.0x10^{11} Hz which is lower than that of nc-Si:H soalr cell. The second band correspond to deep defect was found to be ~450 meV and with an ATE of ~3.0x10^{12} Hz.

Table 4.4 Summary of the parameters calculated from CFT data of nc-SiGe:H solar cell (X_{Ge}=0.35)

Activation Energy, E_a	190 meV	452 meV
ATE, ν_0	5x10^{11} Hz	3 x10^{12} Hz
Pre-factor, Υ	3.7x10^{7} Hz K^{-2}	1.4x10^{7} Hz K^{-2}
Capture cross-section, σ_n^*	5.1x10^{-15} cm^2	3 x10^{-14} cm^2

The defect density profile for nc-SiGe:H solar cell is estimated using the calculated ATE value and shown in Figure 4.30. The carrier response gives a peak around 190 meV with density of 1.0x10^{16} cm^{-3} eV^{-1} followed by a small peak around 350 meV, which is also seen in nc-Si:H defect profile (Figure 4.27). The small peak is eclipsed by a larger Gaussian peak around 450meV with a density of 2.0x10^{16} cm^{-3} eV^{-1} which might be due to Ge incorporation.

The defects around the midgap for nc-SiGe:H is much higher compared to that of nc-Si:H. It is discussed earlier in section 4.2.3 that ppm levels of PH_3 during the nc-SiGe:H growth will reduce the defects caused by Ge incorporation and enhance carrier collection.

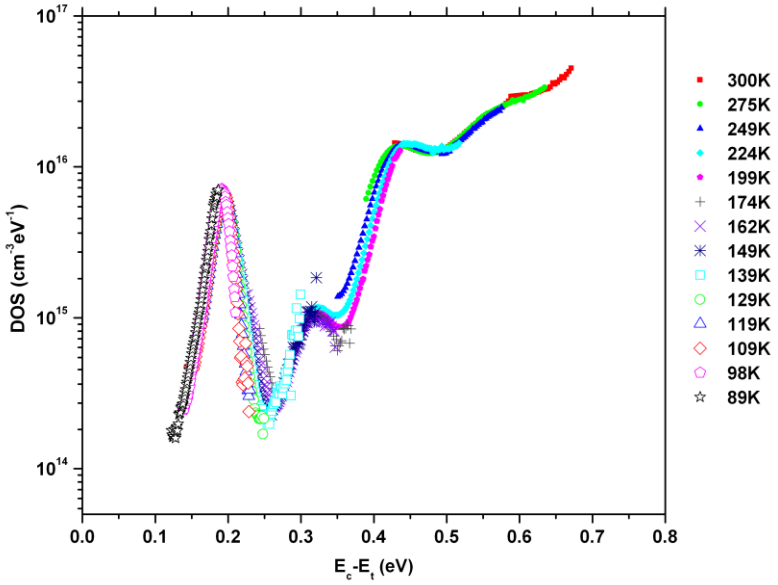

Figure 4.30 Calculated defect density profile of nc-SiGe:H solar cell (X_{Ge}=0.35)

To investigate broader distribution of deep defects extending towards the midgap due to Ge incorporation and the counter action of PH_3, systematic study of midgap defects is needed. Defect density profile for various values of PH_3 for a fixed Ge/Si ratio of in the gas phase (X_{Ge}~0.35) is shown in Figure 4.31. PH_3 helps in reducing the defects around 0.45eV as speculated earlier which is shown by arrow 1 in the figure. It is also noticed that as PH_3 level increased in the material there is slight increase in the defects beyond 0.5eV, but still less than no PH_3 case which is marked by arrow 2. It is previously reported that both deep defects and shallow defects increase due to incorporation of PH_3 during the growth of nc-Si:H solar cell [121]. As nc-SiGe:H growth is similar to nc-Si:H solar cell, it is fair interpretation to deduce that ppm levels of PH_3 helps in reducing defects but excessive PH_3 will have deleterious effects.

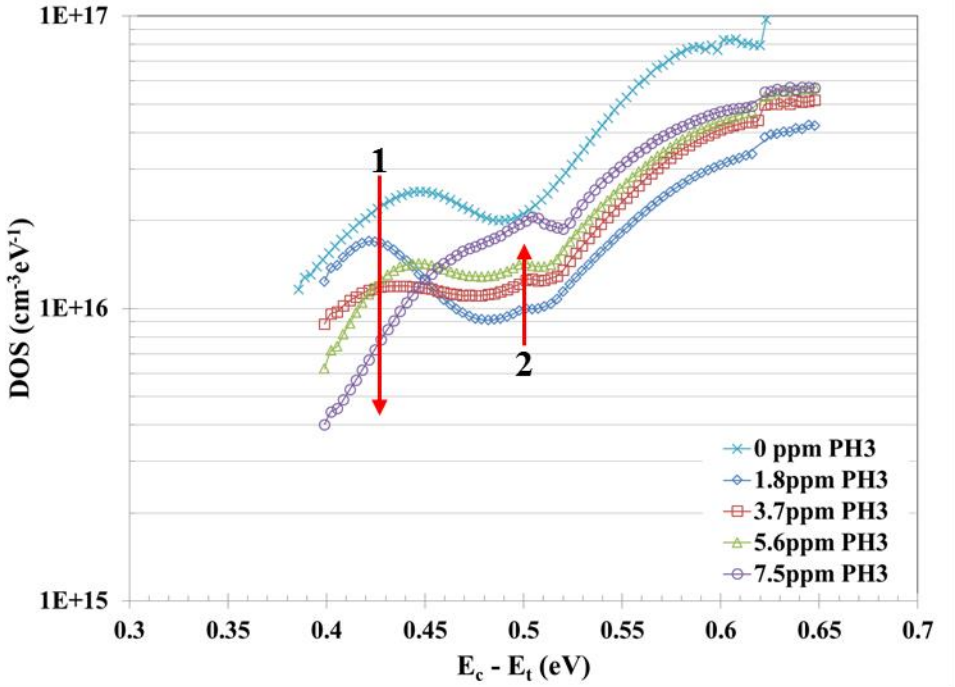

Figure 4.31 Calculated defect density vs. energy below the conduction band for nc-SiGe:H solar cells (X_{Ge}~0.35) for varying PH_3 flow rates

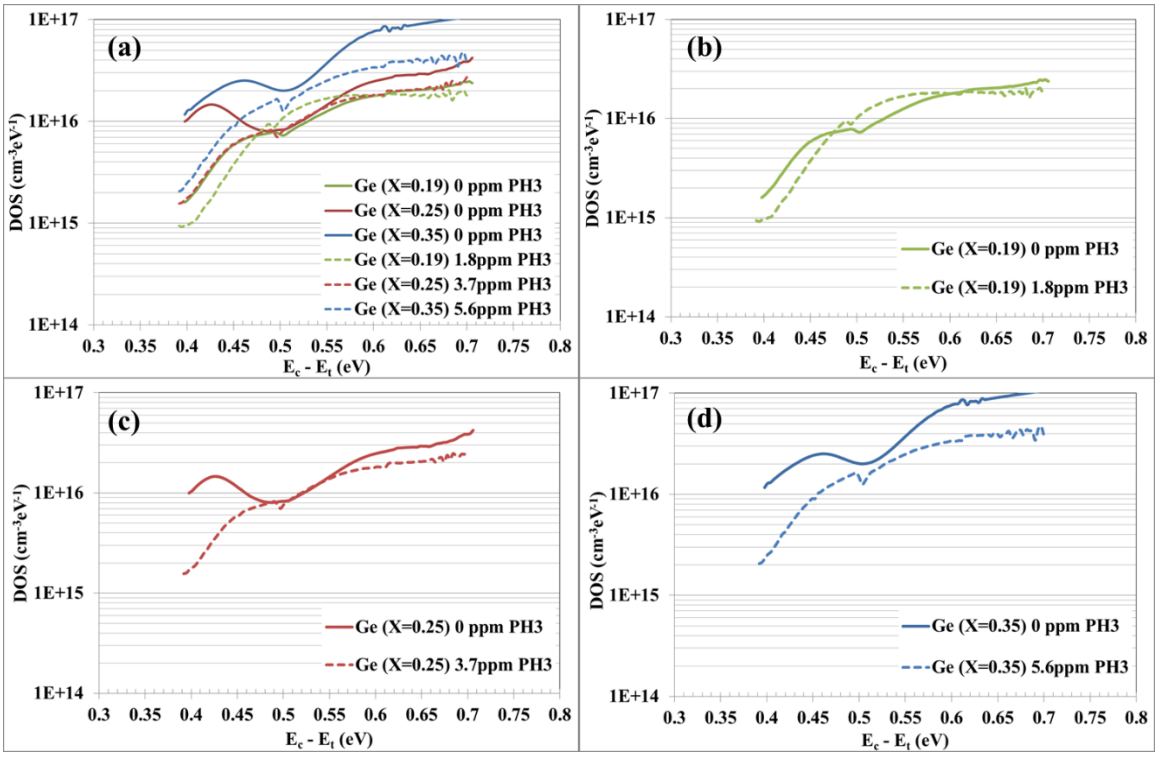

Figure 4.32 (a) Defect density profile in nc-SiGe:H devices with and without PH_3 compensation for varying Ge content, (b) for X_{Ge}= 0.19, (c) for X_{Ge}= 0.25, (d) X_{Ge}= 0.35

The comparison of defect density profile in nc-SiGe:H devices with and without compensating by adding ppm levels of PH_3 to the intrinsic layer is shown in Figure 4.32a. For better explanation, defect density profile for different Ge content are separated in Figure 4.32. As the Ge content increases more PH_3 is required to counter the defects caused by Germanium. For nc-SiGe:H solar cell with X_{Ge} = 0.35, defects can be controlled by adding 5.6 ppm PH_3 during the intrinsic layer growth. It is also observed that even 1.8 ppm PH_3 might increase the midgap defects for lower Ge content samples.

CHAPTER 5. CONCLUSION

In this chapter the results obtained in this work are summarized followed by a discussion of the ideas for future work.

5.1 Summary

The main objective of this work was to study the fundamental properties such as carrier mobility, mid-gap defect densities, tail state densities and diffusion lengths in nc-SiGe:H and their relationship to grain size and Ge content.

- We have successfully demonstrated the relationship between grain size and growth parameters in nc-Ge films fabricated using PECVD. SCLC technique is employed to measure carrier mobility for various grain sizes and it is shown that high grain size leads to higher mobility in the nanocrystalline materials.
- The crystallinity of the material is controlled by utilizing various techniques such as Hydrogen profile, power grading and superlattice. It is shown that the crystallinity can be controlled across the thickness of intrinsic layer.
- Ge atomic fraction was calculated in nc-SiGe:H films using EDS. It is observed that Ge content in solid phase is higher than gas phase GeH_4 concentration and explained by the fact that GeH_4 has lower dissociation energy.
- Absorption spectra for varying Ge content showed that higher the Ge content, higher is the absorption in infrared region.
- Strong dependence nc-SiGe:H composition on deposition parameters such as gas concentration, power, temperature and pressure is observed.

- Initial nc-SiGe:H devices showed promising results with higher current densities due to higher absorption. However as Ge content increases in nc-SiGe:H solar cell, there was a deleterious effect on the device performance. There is drastic drop in lower wavelength QE for higher Ge content devices.
- It is also shown that the defect density in the intrinsic layer of nc-SiGe:H increases significantly as Ge content increases. It appeared that adding Ge changes the doping type of the intrinsic layer form n-type to p-type and thus lead to a drastic reduction in QE for short wavelength photons at higher Ge concentrations.
- The defect densities are reduced by adding ppm levels of PH_3 to the gas phase and the p-type behavior changed back to n-type. The results showed that when appropriate compensation by Phosphorus is incorporated, QE at shorter wavelength can be recovered at the same time QE is extended into infrared regions for higher Ge content devices.
- Further it is observed that the defects decreased by adding appropriate PH_3 according to Ge content in nc-SiGe:H solar cell. It is an important result which shows that nc-SiGe:H solar cells can be used to improve the efficiency of tandem junction solar cells as infrared response increased.
- CFT measurements are employed to measure attempt to escape frequency (ATE) and defect density profile in the solar cell materials. The setup is capable of temperatures ranging from 100K to 400K and frequency ranging from 1Hz to 200kHz.
- CFT setup is validated using a-Si:H defect measurements, ATE is well known for a-Si:H material and the value obtained was within the range.

- Defect density profile of nc-Si:H, nc-SiGe:H solar cells are estimated using CFT data and calculated ATE. This gave good understanding of midgap states, tail states in the material. This study also helped in evaluating the defects caused by higher Ge content and counter doping by PH_3.
- It is shown from the defect profile of nc-SiGe:H with varying PH_3 content, there is an optimum P concentration to reduce the defects, excessive PH_3 creates a trap level at different energy below conduction band.
- Deep defect density and ATE is calculated for Perovskite based solar cells as well which helped in estimating the dielectric constant of the material. Further studies are required to understand the defect profile of Perovskite based solar cell.

5.2 Future Work

The following ideas can be implemented as a direction for future work

- Reverse recovery technique can be used to measure the lifetime in nc-SiGe:H films with different Ge content. Lifetime vs. defect density of the material can give insight into the device properties.
- Dark and photo conductivity measurements as a function of Ge content in nc-SiGe:H could explain the significant decrease in QEs at lower wavelength.
- Defect density profile in nc-SiGe:H, measured using CFT to understand the energetic distribution of defects caused by different impurities can be studied.
- Defect density profile for Perovskite based solar cells can be used in the stability studies to explain the rapid degradation due to moisture.

BIBLIOGRAPHY

1. http://www.ren21.net/REN21Activities/GlobalStatusReport.aspx

2. M. A. Green, "Recent developments in photovoltaics", Solar Energy, 76(1-3), 3-8, (2004)

3. http://greentechresearch.wordpress.com/2013/06/07/solar-cells-a-shining-technology-between-politics-and-science/

4. R. C. Chittick, J. H. Alexander and H. F. Sterling, "Preparation and properties of amorphous silicon", Journal of the Electrochemical Society, 116 (1), 77-81, (1969)

5. B. Abeles, G.D. Cody, Y. Goldstein, T. Tiedje, C.R. Wronski, "Hydrogenated amorphous silicon solar cells", Thin Solid Films, 90 (4), 441-449, (1982)

6. J. I. Pankove and D. E. Carlson, "Electrical and Optical Properties of Hydrogenated Amorphous Silicon", Annual Review of Materials Science, 10, 43 -63, (1980)

7. D. L. Staebler and C. R. Wronski, "Reversible conductivity changes in discharge-produced amorphous Si", Applied Physics Letters, 31, 292-294, (1977)

8. N. Wang and V. Dalal, "Improving stability of amorphous silicon using chemical annealing with helium", Journal of Non-Crystalline Solids, 352, 1937-1940, (2006)

9. H. Keppner, J. Meier, P. Torres, D. Fischer and A. Shah, "Microcrystalline silicon and micromorph tandem solar cells", Applied Physics A, 69 (2), 169-177, (1999)

10. A. Shah, J. Meier, A. Buechel, U. Kroll, J. Steinhauser, F. Meillaud, H. Schade and D. Dominé, "Towards very low-cost mass production of thin-film silicon photovoltaic (PV) solar modules on glass", Thin Solid Films, 502 (1–2), 292-299, (2006)

11. A. Shah, J. Meier, E, Vallat-Sauvain, N. Wyrsch, U. Kroll, C. Droz and U. Graf, "Material and Solar cell research in microcrystalline silicon", Solar Energy Materials and Solar Cells, 78, 469-491, (2003)

12. S. Klein, F. Finger, R. Carius, T. Dylla, B. Rech, M. Grimm, L. Houben and M. Stutzmann, "Intrinsic microcrystalline silicon prepared by hot-wire chemical vapour deposition for thin film solar cells", Thin Solid Films, 430 (1–2), 202-207, (2003)

13. R.W. Collins, A. S. Ferlauto, G. M. Ferreira, C. Chen, J. Koh, R. J. Koval, Y. Lee, J. M. Pearce and C. R. Wronski, "Evolution of microstructure and phase in amorphous, protocrystalline, and microcrystalline silicon studied by real time spectroscopic ellipsometry", Solar Energy Materials and Solar Cells 78, 143–180, (2003)

14. J. Bailat, E. Vallat-Sauvain, L. Feitknecht, C. Droz, and A. Shah , "Microstructure and open-circuit voltage of n−i−p microcrystalline silicon solar cells", Journal of Applied Physics, 93, 5727 (2003)

15. C. J. Brabec, N. S. Sariciftci and J. C. Hummelen, "Plastic solar cells," Advanced Functional Materials, 11, 1, (2001)

16. T. Aernouts, T. Aleksandrov, C. Girotto, J. Genoe and J. Poortmans, "Polymer based organic solar cells using ink-jet printed active layers", Applied Physics Letters, 92, 033306, (2008)

17. F. C. Krebs, "Fabrication and processing of polymer solar cells: A review of printing and coating techniques", Solar Energy Materials and Solar Cells, 93 (4), 394-412, (2009)

18. F. C. Krebs, "Polymer solar cell modules prepared using roll-to-roll methods: Knife-overedge coating, slot-die coating and screen printing", Solar Energy Materials and Solar Cells 93 (4), 465-475, (2009)

19. F. C. Krebs, S. A. Gevorgyan and J. Alstrup, "A roll-to-roll process to flexible polymer solar cells: model studies, manufacture and operational stability studies", Journal of Materials Chemistry 19, 5442-5451, (2009)

20. C. Girotto, D. Moia, B. P. Rand and P. Heremans, "High-Performance Organic Solar Cells with Spray-Coated Hole-Transport and Active Layers", Advanced Functional Materials, 21 (1), 64-72, (2011)

21. G. Li, R. Zhu and Y. Yang, "Polymer solar cells", Nature Photonics 6, 153-161, (2012)

22. Z. He, C. Zhong, S. Su, M. Xu, H. Wu and Y. Cao, "Enhanced power-conversion efficiency in polymer solar cells using an inverted device structure", Nature Photonics, 6, 591-595, (2012)

23. M. Jorgensen, K. Norrman and F. C. Krebs, "Stability/degradation of polymer solar cells", Solar Energy Materials and Solar Cells 92, 686-714, (2008)

24. K. Kawano, R. Pacios, D. Poplavskyy, J. Nelson, D. D. C. Bradley and J. R. Durrant, "Degradation of organic solar cells due to air exposure", Solar Energy Materials and Solar Cells 90, 3520-3530, (2006)

25. J. Bhattacharya, R. W. Mayer, M. Samiee and V. L. Dalal, "Photo-induced changes in fundamental properties of organic solar cells" Applied Physics Letters, 100, 193501 (2012)

26. O. A. Abdulrazzaq, V. Saini, S. Bourdo, E. Dervishi and A. S. Biris, "Organic Solar Cells: A Review of Materials, Limitations, and Possibilities for Improvement", Particulate Science and Technology, 31(5), 427-442, (2013)

27. J. Bhattacharya, "Understanding the physics of degradation of polymer solar cells", Iowa State University, PhD Thesis, (2013)

28. M. Liu, M. B. Johnston, and H. J. Snaith, "Efficient planar heterojunction perovskite solar cells by vapor deposition" Nature 501, 395 (2013).

29. J. Burschka, N. Pellet, S.-J. Moon, R. Humphry-Baker, P. Gao, M. K. Nazeeruddin, and M. Gratzel, "Sequential deposition as a route to high-performance perovskite-sensitized solar cells" Nature 499, 316 (2013).

30. V. Gonzalez-Pedro, E. J. Juarez-Perez, W. Arsyad, E. M. Barea, F.Fabregat-Santiago, I. Mora-Sero, and J. Bisquert, "General Working Principles of $CH_3NH_3PbX_3$ Perovskite Solar Cells" Nano Letters. 14, 888–893 (2014).

31. G. E. Eperon, V. M. Burlakov, A. Goriely, and H. J. Snaith, "Neutral Color Semitransparent Microstructured Perovskite Solar Cells" ACS Nano 8, 591–598 (2014).

32. J. Im, I. Jang, N. Pellet, M. Gratzel, and N. Park, "Growth of $CH_3NH_3PbI_3$ cuboids with controlled size for high-efficiency perovskite solar cells," Nature Nanotechnology 9, 927–932 (2014)

33. M. A. Green, A. Ho-Baillie and H. J. Snaith, "The emergence of perovskite solar cells", Nature Photonics 8, 506–514, (2014)

34. H. Zhou, Q. Chen, G. Li, S. Luo, T. Song, H. Duan, Z. Hong, J. You, Y. Liu, Y. Yang, "Interface engineering of highly efficient perovskite solar cells", Science 345, 542 (2014)

35. Solar PV Fact book, SBC, Energy Institute Publications (2013)

36. W. Germer, "Microcrystalline silicon thin films for sensor applications", Sensors and Actuators, 7 (2), 135-142 (1985)

37. D. Ghosh, R. Shinar, V. Dalal, Z. Zhou and J. Shinar, "Amorphous and nanocrystalline p–i–n Si and Si,Ge photodetectors for structurally integrated O^2 sensors", Journal of Non-Crystalline Solids, 354 (19–25), 2606-2609, (2008)

38. J. Meier, S. Dubail, R. Fluckiger, D. Fischer, H. Keppner, and A. Shah, "Intrinsic microcrystalline silicon (μc-Si:H)-a promising new thin film solar cell material", Twenty Fourth IEEE Photovoltaic Specialists Conference, 1, 409-412, (1994)

39. B Rech, O Kluth, T Repmann, T Roschek, J Springer, J Müller, F Finger, H Stiebig and H. Wagner, "New materials and deposition techniques for highly efficient silicon thin film solar cells", Solar Energy Materials and Solar Cells, 74 (1–4), 439-447, (2002)

40. D. Panda, M. Noack and V. Dalal "P-Channel MOSFET Devices in Nanocrystalline Silicon". MRS Proceedings, 910, 0910-A22-07, (2006)

41. C. H. Lee, A. Sazonov, A. Nathan and J. Robertson, "Directly deposited nanocrystalline silicon thin-film transistors with ultra-high mobilities", Applied Physics Letters 89, 252101, (2006)

42. S. Vepřek and V. Mareček, "The preparation of thin layers of Ge and Si by chemical hydrogen plasma transport", Solid-State Electronics, 11 (7), 683-684, (1968)

43. G. Lucovsky, C. Wang, M. J. Williams, Y. L. Chen and D. M. Mauer, "Transport and Microstructure of Microcrystalline Silicon Alloys" MRS Proceedings, 283, 443 (1992).

44. A. Matsuda, "Formation kinetics and control of microcrystallite in μc-Si:H from glow discharge plasma", Journal of Non-Crystalline Solids, 59-60, 767-774, (1983)

45. J Meier, R Flückiger, H Keppner and A Shah, ""Complete microcrystalline p-i-n solar cell—Crystalline or amorphous cell behavior?" Applied Physics Letters, 65, 860-862 (1994)

46. P. Torres, J. Meier, R. Fluckiger, U. Kroll, J. A. Anna Selvan, H. Keppner, A. Shah, S. D. littlewood, I. E. Kelly and P. Giannoules, "Device grade microcrystalline silicon owing to reduced oxygen contamination", Applied Physics Letters, 69, 1373-1375 (1996)

47. J. Meier, P. Torres, R. Platz, S. Dubail, U. Kroll, J. A. Anna Selvan, N. Pellaton Vaucher, Ch. Hof, D. Fischer, H. Keppner, A. Shah, K. -D. Ufert, P. Giannoulès and J Koehler, "On the Way Towards High Efficiency Thin Film Silicon Solar Cells by the "Micromorph" Concept", MRS Proceedings, 420, 3, (1996)

48. O. Vetterl, F. Finger, R. Carius, P. Hapke, L. Houben, O. Kluth, A. Lambertz, A. Mück, B. Rech and H. Wagner, "Intrinsic microcrystalline silicon: A new material for photovoltaics", Solar Energy Materials and Solar Cells, 62 (1–2), 97-108, (2000)

49. A. Matsuda "Microcrystalline silicon. Growth and device application", Journal of Non-Crystalline Solids, 338, 1-12, (2004)

50. Y. Mai, S. Llein, R. Carius, J. Wolff, A. Lambertz, F. Finger, and X. Geng, "Microcrystalline silicon solar cells deposited at high rates", Journal of Applied Physics, 97, 11493, (2003)

51. CC Tsai, GB Anderson, R. Thompson, and B. Wacker. "Control of silicon network structure in plasma deposition", Journal of Non-Crystalline Solids, 114, 151-153, (1989)

52. K. Nakamura, K. Yoshino, S. Takeoka, and I. Shimizu, "Roles of Atomic Hydrogen in Chemical Annealing", Japanese Journal of Applied Physics, 34 (1), 442-449, (1995)

53. V. Dalal "Fundamental considerations regarding the growth of amorphous and microcrystalline silicon and alloy films", Thin Solid Films, 395 (1-2), 173-177, (2001)

54. A. Matsuda. Growth mechanism of microcrystalline silicon obtained from reactive plasmas", Thin Solid Films, 337 (1-2), 1-6, (1999)

55. R. Biswas, B.C. Pan, and Y. Ye, "Metastability of amorphous silicon from silicon network rebonding", Physical Review Letters 88, 205502 (2002)

56. B.C. Pan and R. Biswas, "Structure and simulation of hydrogenated nanocrystalline silicon", Journal of Applied Physics, 96, 6247 (2004)

57. B. C. Pan and R. Biswas, "Simulation of hydrogen evolution from nano-crystalline silicon", Journal of Non-Crystalline Solids, 333 (1), 44-47, (2004)

58. J. Kočka, A. Fejfar, H. Stuchlíková, J. Stuchlík, P. Fojtík, T. Mates, B. Rezek, K. Luterová, V. Švrček, and I. Pelant, "Basic features of transport in microcrystalline silicon", Solar energy materials and solar cells, 78, 493 (2003)

59. B. Yan, G.Yue, J. Yang, S. Guha, D. L. Williamson, D. Han and C. Jiang, "Microstructure Evolution with Thickness and Hydrogen Dilution Profile in Microcrystalline Silicon Solar Cells", MRS Proceedings, 808, A8.5, (2004)

60. J. Gu, M. Zhu, L. Wang, F. Liu, B. Zhou, K. Ding and G. Li, "High quality microcrystalline Si films by hydrogen dilution profile", Thin Solid Films, 515 (2), 452-455, (2006)

61. X. Han, G. Hou, X. Zhang, C. Wei, G. Li, J. Zhang, X. Chen, D. Zhang, J. Sun, Y. Zhao and X. Geng, "Improvement of hydrogenated microcrystalline silicon solar cell performance by VHF power profiling technique", Solar Energy Materials and Solar Cells, 94, 254, (2010)

62. A. Madhavan, "Alternative design for solar cells", Iowa State University, Thesis, (2009)

63. T. Kilper, W. Beyer, G. Bräuer, T. Bronger, R. Carius, M. N. van den Donker, D. Hrunski, A. Lambertz, T. Merdzhanova, A. Mück, B. Rech, W. Reetz, R. Schmitz, U. Zastrow and A. Gordijn, "Oxygen and nitrogen impurities in microcrystalline silicon deposited under optimized conditions: Influence on material properties and solar cell performance", Journal of Applied Physics, 105, 074509, (2009)

64. P. G. Hugger, J. D. Cohen, B. Yan, G. Yue, J. Yang and S. Guha, "Relationship of deep defects to oxygen and hydrogen content in nanocrystalline silicon photovoltaic materials", Applied Physics Letters, 97, 252103 (2010)

65. J. T. Heath, J. D. Cohen and W. N. Shafarman, "Bulk and metastable defects in CuInGaSe thin films using drive-level capacitance profiling" Journal of Applied Physics 95, 1000, (2004)

66. P. Sharma "Study of nano-crystalline silicon deposited by VHF-PE CVD for solar cell devices", PhD Thesis, Iowa State University, (2005)

67. S. Saripalli "Transport Properties in Nanocrystalline Silicon and Silicon Germanium", PhD Thesis, Iowa State University, (2008)

68. S. Kajjam "Influence of Oxygen on Electronic properties of Nanocrystalline Silicon", PhD Thesis, Iowa State University, (2013)

69. D. Congreve, S. Kajjam, N. Chakravarty and V. Dalal, "Influence of oxygen on defect densities in nanocrystalline Si", Journal of Non-Crystalline Solids, 358 (17), 2071, (2012)

70. A. Shah, J. Meier, E. Vallat-Sauvain, C. Droz, U. Kroll, N. Wyrsch, J. Guillet and U. Graf, "Microcrystalline silicon and 'micromorph' tandem solar cells", Thin Solid Films, 403–404, 179-187, (2002)

71. J. Meier, S. Dubail, S. Golay, U. Kroll, S. Faÿ, E. Vallat-Sauvain, L. Feitknecht, J. Dubail and A. Shah, "Microcrystalline silicon and the impact on micromorph tandem solar cells", Solar Energy Materials and Solar Cells, 74 (1–4), 457-467 (2002)

72. K. Yamamoto, A. Nakajima, M. Yoshimi, T. Sawada, S. Fukuda, T. Suezaki, M. Ichikawa, Y. Koi, M. Goto, T. Meguro, T. Matsuda, M. Kondo, T. Sasaki and Y. Tawada, "A high efficiency thin film silicon solar cell and module", Solar Energy, 77 (6), 939-949, (2004)

73. G. Yue, B. Yan, L. Sivec, T. Su, Y. Zhou, J. Yang and S. Guha, "Hydrogenated Nanocrystalline Silicon based Solar Cell with 13.6% Stable Efficiency", MRS Proceedings, 1426, 33-38, (2012)

74. J.A.Tsai, A. J. Tang, T. Noguchi and R. Reif, "Effects of Ge on Material and Electrical Properties of Polycrystalline $Si_{1-x}Ge_x$ for Thin-Film Transistors", Journal of The Electrochemical Society, 142, 3220, (1995)

75. T. Matsui, M. Kondo, K. Ogata, T. Ozawa and M. Isomura, "Influence of alloy composition on carrier transport and solar cell properties of hydrogenated microcrystalline silicon-germanium thin films", Applied Physics Letters, 89, 142115 (2006)

76. G. Ganguly, M. Fukawa, T. Ikeda and A. Matsuda, "A study of the growth-mechanism and properties of microcrystalline silicon–germanium", Journal of Non-Crystalline Solids, 227–230 (2), 1069-1073, (1998)

77. X. Niu and V. Dalal, "Growth and properties of nanocrystalline germanium films", Journal of Applied Physics, 98, 096103, (2005)

78. L. Houben, R. Carius , D. Lundszien, J. Folsch , F. Finger, M. Luysberg and H. Wagner "Structural properties of microcrystalline silicon-germanium films", Philosophical Magazine Letters, 79 (2), 71-78, (1999)

79. S. Miyazaki, H. Takahashi, H. Yamashita, M. Narasaki and M. Hirose, "Growth and characterization of microcrystalline silicon–germanium films", Journal of Non-Crystalline Solids, 299–302 (1), 148-152, (2002)

80. T. Matsui, K. Ogata, M. Isomura and M. Kondo, "Microcrystalline silicon–germanium alloys for solar cell application: Growth and material properties", Journal of Non-Crystalline Solids, 352 (9–20), 1255-1258, (2006)

81. J. K. Rath, F. D. Tichelaar and R. E. I. Schropp, "Heterogeneous growth of microcrystalline silicon germanium", Solar Energy Materials and Solar Cells, 74 (1–4), 553-560, (2002)

82. M. Isomura, M. Shima, S. Taira, K. Wakisaka, S. Okamoto and S. Kiyama, "Microcrystalline silicon-germanium as a low-gap material for solar cells," Twenty-Eight IEEE Photovoltaic Specialists Conference, 776-779, (2000)

83. M. Isomura, K. Nakahata, M. Shima, S. Taira, K. Wakisaka, M. Tanaka and S. Kiyama, "Microcrystalline silicon–germanium solar cells for multi-junction structures", Solar Energy Materials and Solar Cells, 74 (1–4), 519-524, (2002)

84. T. Matsui, H. Jia and M. Kondo, "Thin film solar cells incorporating microcrystalline $Si_{1-x}Ge_x$ as efficient infrared absorber: an application to double junction tandem solar cells", Progress in Photovoltaics Research and Applications, 18, 48–53, (2010)

85. T. Matsui, CW. Chang, K. Mizuno, Y. Takeuchi and M. Kondo, "Compensation of Native Defect Acceptors in Microcrystalline Ge and $Si_{1-x}Ge_x$ Thin Films by Oxygen Incorporation: Electrical Properties and Solar Cell Performance", Japanese Journal of Applied Physics, 51, 091302, (2012)

86. A. Bidiville, T. Matsui and M. Kondo, "Effect of oxygen doping in microcrystalline SiGe p-i-n solar cells", Journal of Applied Physics, 116, 053701 (2014)

87. J. R. Weber, A. Janotti, P. Rinke and C. G. Van de Walle, "Dangling-bond defects and hydrogen passivation in germanium", Applied Physics Letters, 91, 142101 (2007)

88. Y. Cao, J. Zhang, C. Li, T. Li, Z. Huang, J. Ni, Z. Hu, X. Geng and Y. Zhao, "Hydrogenated microcrystalline silicon germanium as bottom sub-cell absorber for triple junction solar cell", Solar Energy Materials and Solar Cells, 114, 161-164, (2013)

89. YT. Huang, HJ. Hsu, SW. Liang, CH. Hsu and CC Tsai, "Development of Hydrogenated Microcrystalline Silicon-Germanium Alloys for Improving Long-Wavelength Absorption in Si-Based Thin-Film Solar Cells", International Journal of Photoenergy, 579176, (2014)

90. K. V. Maydell, K. Grunewald, M. Kellermann, O. Sergeev, P. Klement, N. Reininghaus and T. Kilper, "Microcrystalline SiGe Absorber Layers in Thin-film Silicon Solar Cells", Energy Procedia, 44, 209-215, (2014)

91. J. Ni, Q. Liu, JJ. Zhang, J. Ma, H. Wang, XD. Zhang and Y. Zhao, "Microcrystalline silicon–germanium solar cells with spectral sensitivities extending into 1300nm", Solar Energy Materials and Solar Cells, 126, 6-10, (2014)

92. J. Robertson, "Growth mechanism of hydrogenated amorphous silicon", Journal of Non-Crystalline Solids, 266, 79-83, (2000)

93. J. Dutta, U. Kroll, P. Chabloz, A. Shah, A. A. Howling, J. L. Dorier and Ch. Hollenstein, "Dependence of intrinsic stress in hydrogenated amorphous silicon on excitation frequency in a plasma-enhanced chemical vapor deposition process" Journal of Applied Physics, 72, 3220-3222 (1992)

94. E. Amanatides, D. Mataras and D. E. Rapakoulias, "Effect of frequency in the deposition of microcrystalline silicon from silane discharges" Journal of Applied Physics, 90, 5799-5807 (2001)

95. V. Dalal, K. Muthukrishnan, S. Saripalli, D. Stieler and M. Noack "Growth and Electronic Properties of Nanocrystalline Si". MRS Proceedings, 910, 0910-A13-01 (2006).

96. R. Swanepoel "Determination of surface roughness and optical constants of inhomogeneous amorphous silicon films." Journal of Physics E: Scientific Instruments 17.10, 896 (1984)

97. Z. Iqbal and S. Veprek. “Raman Scattering From Hydrogenated Microcrystalline and Amorphous Silicon”, Journal of Physics C (Solid State Physics), 15(2), 377-392, (1982)

98. E. Bustarret, M. A. Hachicha, and M. Brunel. "Experimental determination of the nanocrystalline volume fraction in silicon thin films from Raman spectroscopy." Applied Physics Letters 52.20, 1675-1677, (1988)

99. W. H. Zachariasen, “A general theory of X-ray diffraction in crystals” Acta Crystallographica, 23, 558, (1967)

100. B. D. Cullity and J. W. Weymouth. “Elements of X-Ray Diffraction”, American Journal of Physics, 25, 394, (1957)

101. Y. Sun, T. Miyasato, and J. K. Wigmore, “Possible origin for (110)-oriented growth of grains in hydrogenated microcrystalline silicon films”, Applied Physics Letters, 70, 508, (1997)

102. V. Dalal, K. Muthukrishnan, X. Niu and D. Stieler, “Growth chemistry of nanocrystalline silicon and germanium films”, Journal of Non-Crystalline Solids, 352, 892-895, (2006)

103. J. I. Goldstein, D. E. Newbury, P. Echlin, D. C. Joy, C. E. Lyman, E. Lifshin, L. Sawyer, J. R. Michael “Scanning Electron Microscopy and X-ray Microanalysis” 3rd ed. Springer (2003)

104. D. Stieler “ Measurement of mobility in nanocrystalline semiconductor materials using space charge limited current” Master Thesis, Iowa State University, (2005).

105. M. Lampert and P. Mark, “Current Injection in Solids”, New York and London: Academic Press, (1970)

106. V. Dalal, M. Leonard, J. Booker and A. Vaseashta, “Quantum efficiency of aSi:H alloy solar cells”, IEEE, 837, (1985)

107.http://pveducation.org/pvcdrom/solar-cell-operation/quantum-efficiency

108.L.C. Kimerling, “Influence of deep traps on the measurement of free-carrier distributions in semiconductors by junction capacitance techniques”, Journal of Applied Physics, 45, 1839, (1974)

109.T. Walter, R. Herberholz, C. Muller and H. Schock, “Determination of defect distributions from admittance measurements and application to Cu(In,Ga)Se2 based heterojunctions”, Journal of Applied Physics 80, 4411-4420, (1996)

110.S. Kajjam, S. Konduri, M. Noack, G. Shamshimov, N. Ussembayev and V. Dalal, “Defect Densities and Carrier Lifetimes in Oxygen doped Nanocrystalline Si”, MRS Proceedings, 1536, 169-173, (2013)

111.S. Kajjam, S. Konduri and V. Dalal “Influence of oxygen contamination on minority carrier lifetime and defect density in nanocrystalline Si”, Applied Physics Letters, 103, 093506, (2013)

112.H. J. Scofield, "Effects of series resistance and inductance on solar cell admittance measurements." Solar energy materials and solar cells 37.2, 217-233, (1995)

113.S. S. Hegedus and E. Fagen, “Midgap states in a-Si:H and a-SiGe:H pin solar cells and Schottky junctions by capacitance techniques” Journal of applied physics 71, 5941-5951 (1992)

114.J. A. Carr, “The identification and characterization of electronic defect bands in organic photovoltaic devices”, Iowa State University, PhD Thesis, (2014)

115.J. D. Cohen and D. V. Lang, “Calculation of the dynamic response of Schottky barriers with a continuous distribution of gap states” Physical Review B 25 (8), 5321 (1982)

116.J. Heath and P. Zabierowski, “Capacitance Spectroscopy of Thin-Film Solar Cells” Advanced Characterization Techniques for Thin Film Solar Cells (Wiley-VCH), 81-105 (2011)

117.S. Saripalli and V. Dalal, "Microcrystalline silicon-germanium solar cells fabricated using VHF PECVD", IEEE EIT Proceedings, 414-418, (2008)

118.T. Tiedje, J. Cebulka, D. Morel and B. Abeles, “Evidence for Exponential Band Tails in Amorphous Silicon Hydride” Physical Review Letters 46, 1425-1428 (1981).

119.E. Schiff, “Trap-Controlled Dispersive Transport and Exponential Band Tails in Amorphous Silicon”, Physical Review B 24 (10), 6189-6192 (1981).

120.D. V. Lang, J. D. Cohen and J. P. Harbison, “Measurement of the density of gap states in hydrogenated amorphous silicon by space charge spectroscopy” Physical Review B 25 (8), 5285 (1982).

121.V. Dalal and P. Sharma, "Defect density and diffusion length of holes in nanocrystalline silicon devices" Applied Physics Letters 86.10 (2005): 103510-103510

APPENDIX A

Grain Growth and Mobility in Nanocrystalline Ge Films

This work was published in MRS proceedings 2012

Siva Konduri*, Max Noack**, Vikram Dalal*
*Dept. of Electrical and Computer Engineering, Iowa State University, Ames, IA 50011
**Microelectronic Research Center, Iowa State University, Ames, IA 50011

ABSTRACT

In this paper, we report on deposition and properties of nanocrystalline Ge:H films . The films were grown from germane and hydrogen mixtures using Radio frequency Plasma-enhanced chemical vapor deposition (RF-PECVD) process using ~45 MHz frequency. The crystallinity of the films was measured using Raman measurements and from x-ray diffraction techniques, it was found that the grain size was a strong function of deposition pressure, temperature and hydrogen/germane ratios. High hydrogen ratios and high powers led to films with smaller grains. Higher pressures and smaller hydrogen/germane ratio led to films with larger grain sizes, as did higher growth temperatures. The mobility of electrons and holes was measured using space charge limited current (SCLC) techniques in n^+-n-n^+ devices. It was found that nominally undoped films were generally n type with carrier concentrations in the 1E14/cm^3 range. Mobility was found to increase with grain size, with 60 nm grains showing mobility in the 2-3 cm^2/V-s range.

INTRODUCTION

Nanocrystalline Si, Ge and SiGe alloys are the promising materials for many microelectronic devices such as solar cells, thin film transistors and photodetectors [1-4]. There

are extensive studies on growth chemistry and mobility of nanocrystalline Si:H films [5-6] but there is no thorough study on the grain growth and mobility of nanocrystalline Ge:H films. Narrow band gap nanocrstalline materials can be made by alloying Si with Ge and those alloys can be used to extend the photovoltaic response further into infrared region [7]. In this paper we discussed about the grain growth and mobility of nanocrstalline Ge:H films grown using high frequency(~45MHz) PECVD.

EXPERIMENTAL DETAILS

Nanocrystalline Ge;H, (Si,Ge):H films and n^+-n-n^+ devices were grown using PECVD process using ~45MHz frequency. These depositions were performed at different pressure, temperature and dilution ratio to study the grain growth and mobility. Intrinsic films are grown on stainless steel for measuring crystallinity and grain size, for devices nanocrystalline n^+ was grown on each side of i-layer. The device structure is shown in Figure 1a. Aluminum contacts were made using thermal evaporation. It is observed that the undoped films grown were turned n type due to oxygen in the reactor.

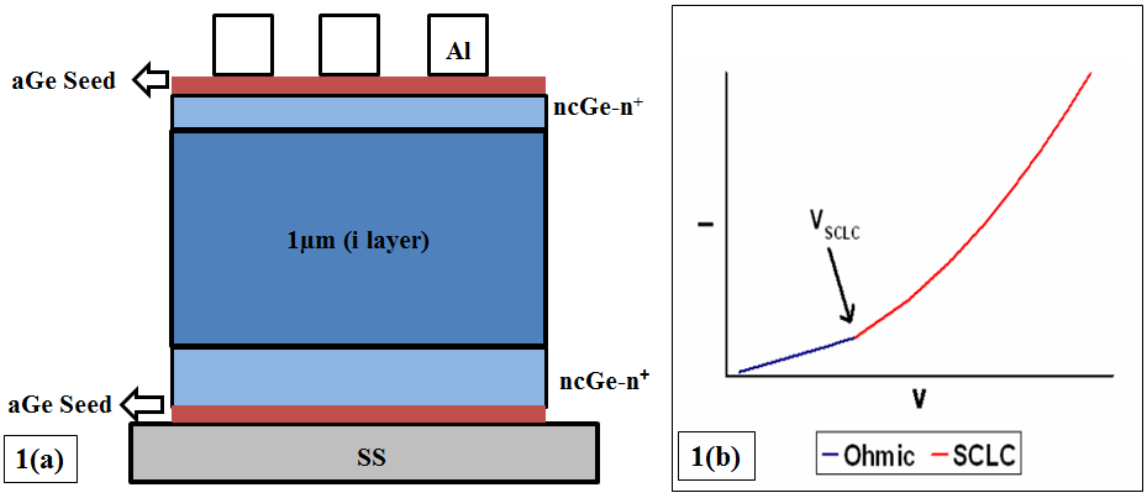

Figure 1. (a) Detailed n^+-n-n^+ device structure, (b) Typical current versus voltage curve in a semiconductor

Crystallinity of films was measured using a micro-Raman spectrometer. Grain size was determined using X-ray diffractometer. The grain size was estimated using Scherer's formula. The mobility was measured using SCLC technique[8]. The voltage at which all the traps in the material are filled i.e. the injected carriers are comparable to resident charges is called V_{SCLC}, it can be calculated using Equation 1. In the equation q is charge of electron, n_0 is the carrier concentration, t is the thickness of i-layer and ε is the permittivity of the material.

$$V_{SCLC} = \frac{q * n_0 * t^2}{\varepsilon} \tag{1}$$

The current versus voltage curve of semiconductor have two regions one below V_{SCLC} is Ohmic region and one above is SCLC region (Figure 1b). The current follows Equation 2 in SCLC region, A is the area of contact and μ is the mobility of the material.

$$I = \frac{9 * \varepsilon * A * \mu}{8 * t^3} * V^2 \tag{2}$$

The devices were annealed at 150C for 45-60 minutes to allow Aluminum to punch through any thin oxide layer formed on the top n^+ layer. Further the samples are electrically annealed by passing 500mA of current for 10-15 minutes for reducing the contact resistance and thereby improving the Ohmic contact of Aluminum.

RESULTS

Grain Growth of nanocrystalline Ge:H and (Si,Ge) films

Figure 2a shows the result from Raman spectroscopy of a typical PECVD nanocrstalline Ge:H film grown at 900mT pressure using Hydrogen, Germane mixture. Figure shows a sharp crystalline peak at ~300cm^{-1} and amorphous shoulder at ~285cm^{-1}. The X-ray spectrum for the same film is in Figure 2b, showing <111> peak at 28.5° with a grain size of 26nm and <220> peak at 45.5° with a grain size of 62nm.

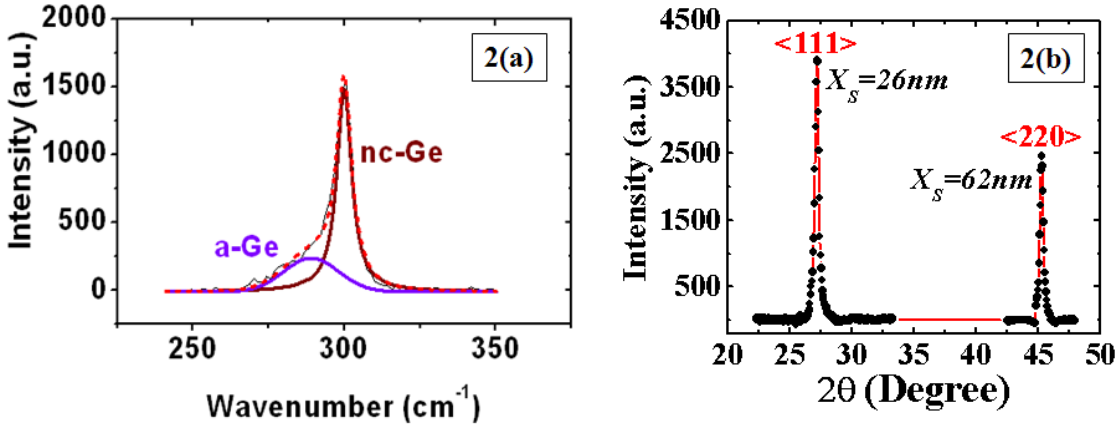

Figure 2. (a) Raman spectrum for PECVD nanocrstalline Ge:H film grown at 900 mT, (b) X-ray diffraction spectrumfor the same film

The grain size versus deposition pressure for a nanocrystalline Ge:H film grown at 300°C shown in Figure 3a. Both <111> and <220> grain size increases with the deposition pressure, but <220> grain size increases significantly suggesting <220> as preferred orientation for crystal growth. In Figure 3b, grain size versus deposition temperature for nanocrystalline (Si.Ge): H film grpwn at 900mT was shown. <111> grain size decreases with temperature whereas <220> grain size increases with the temperature. So the preferred orientation is changing from <111> to <220> as the temperature increases in (Si,Ge):H films.

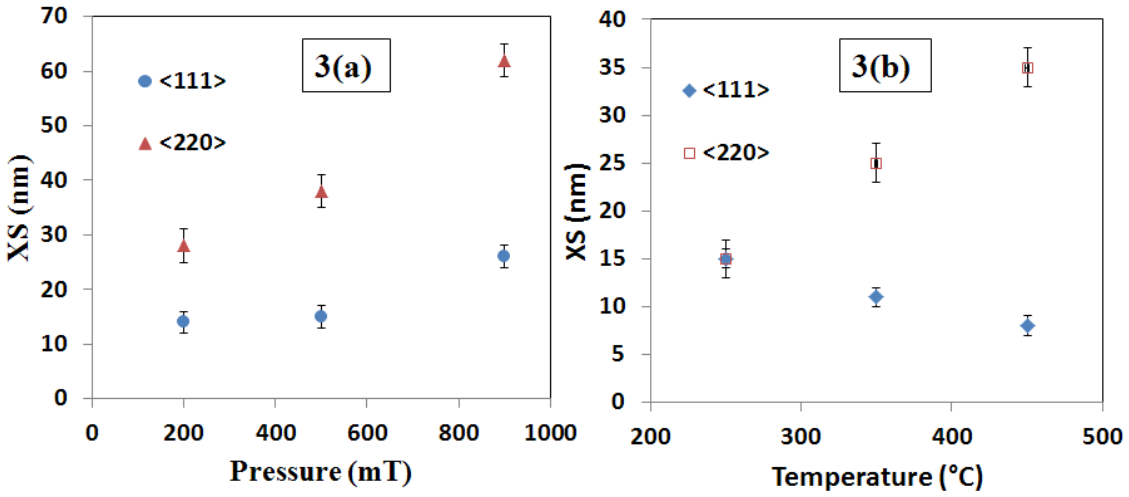

Figure 3. (a) Grain size of nanocrystalline Ge:H films grown at 300C, (b) Grain size of nanocrystalline (Si,Ge):H films grown at 900 mT (Si:Ge ~ 1:1)

Mobility of nanocrystalline Ge:H films

Figure 4a shows the current versus voltage curve for n^+-n-n^+ Ge:H device at a measurement temperature of 25°C. Corresponding Raman and X-ray spectrums were shown in earlier figures.

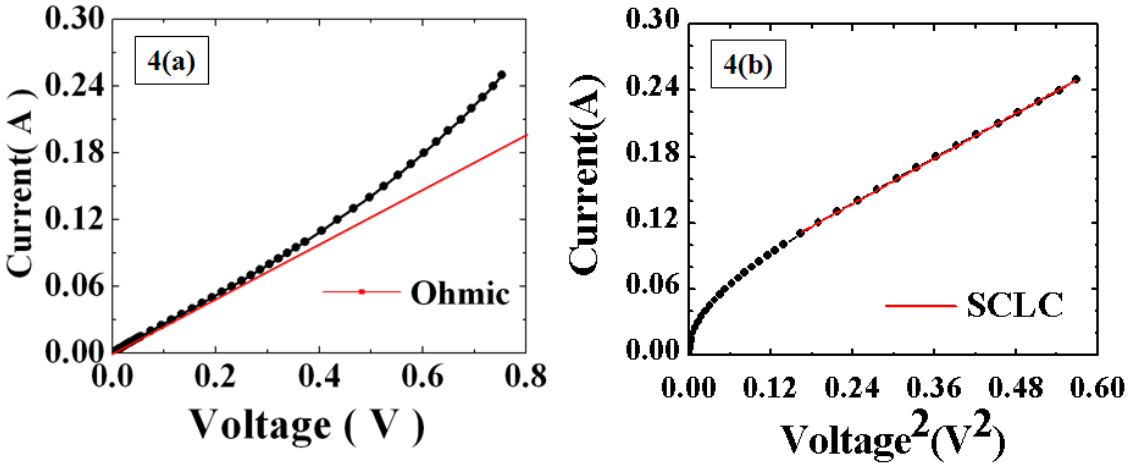

Figure 4. (a) Plot of current versus voltage showing Ohmic region, (b) Plot of current versus voltage^2 showing SCLC region

This figure shows two typical regions, initial linear region and then nonlinear region after V_{SCLC}. Figure 4b shows I vs. V^2 curve at a measurement temperature of 25°C. It shows linear behavior in SCLC region. From the slope, the mobility measured to be 2.1 cm^2/V-s. Using this mobility value and the slope from Ohmic region of Figure 4a, carrier concentration was deduced to be 5E14 and Fermi level is ~0.25eV below conduction band. All the calculated values are shown in Table 1.

Table 1. Calculated values of different parameters using the graphs in Figure 4

Parameter	***Value***
Resistivity	5E3 Ω.cm
Mobility	2.1 cm^2/V-s
V_{SCLC}	0.28 V
Carrier Concentration	5E14 cm^{-3}
E_C - E_F	0.25 eV

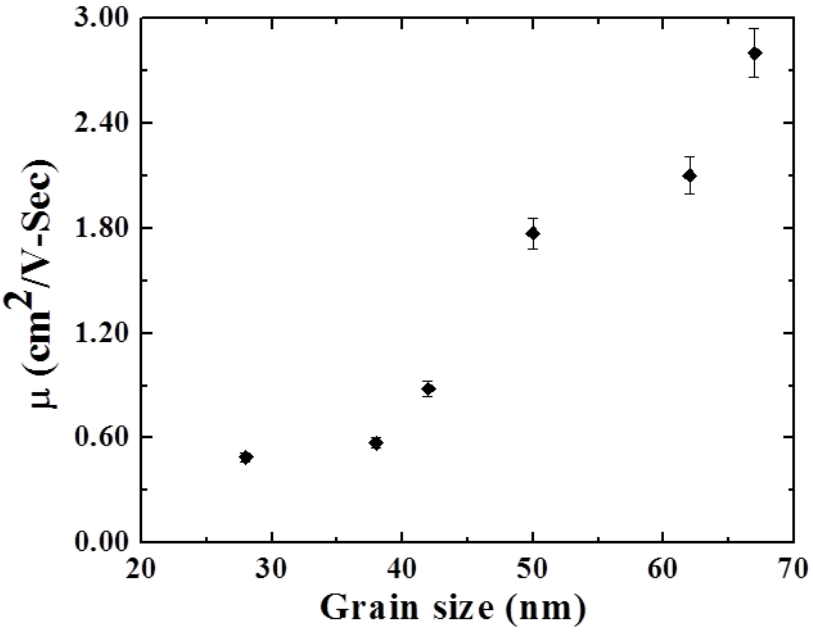

Figure 5. Electron Mobility vs. <220> Grain size

Figure 5 shows the mobility derived from SCLC versus the <220>grain size measured from X-ray diffraction. Mobility increases with the grain size, with the smaller mobility being deposited at lower pressures. As explained earlier lower pressure leads to smaller grains there by smaller mobility. For the largest grain size (~70nm) which is deposited at 900mT pressure, the measured mobility is 2.8 cm^2/V-s.

CONCLUSIONS

In summary, it is shown that <220> is the preferred orientation for both the films and it can be assumed that <111> orientation arises due to random nucleation and hydrogen bonding at the grain boundaries. Preliminary study has been done on the mobility measurement using SCLC technique and a mobility of 2.1 cm^2/V-s was obtained for a nanocrstalline Ge:H device. It is also observed that the electron mobility increase with the grain size in nanocrstalline Ge:H devices.

ACKNOWLEDGMENTS

We thank NSF and Iowa Power Fund for support of this work and Shantan Kajjam for his help.

REFERENCES

[1] Shah A.V., Meier J.; Vallat-Sauvain E.; Wyrsch N.; Kroll U.; Droz C. and Graf U, Solar Energy Materials and Solar Cells, Vol.**78**, pp. 469-491(2003)

[2] Vikram L. Dalal, Kamal Muthukrishnan, Xuejun Niu, Daniel Stieler, Journal of Non-Crystalline Solids, Vol.**352**, pp.892-895 (2006)

[3] Saripalli, S., Dalal, V., IEEE International Conference on Electro/Information Technology 2008, EIT 2008 pp.414-418 (2008)

[4] M. Krause, H. Stiebig, R. Carius and H. Wagner., MRS Proceedings, 664 , A26.5.1 (2001)

[5]Dalal, Vikram, Jeff Leib, Kamal Muthukrisnan, D. Stieler, and Max Noack, IEEE Photovoltaic Specialists Conference 2005. pp.1448- 1451 (2005).

[6] Vikram L. Dalal, Kamal Muthukrishnan, Daniel Stieler and Max Noack, MRS Proceedings, 862 , A21.4 (2005)

[7] T. Matsui, C.W. Chang, T. Takada, M. Isomura, H. Fujiwara, M. Kondo, Solar Energy Materials and Solar Cells, Vol. **93**, pp.1100-1102 (2009)

[8] Lampert, Murray and Peter Mark, New York and London: Academic Press, 1970

Influence of Oxygen Contamination on Minority Carrier Lifetime and Defect Density in Nanocrystalline Si

This work was published in Applied Physics Letters 2013

Shantan Kajjam, Siva Konduri, and Vikram L. Dalal[a)]
Department of Electrical and Computer Engineering, Iowa State University, Ames, Iowa 50011, USA

(Received 24 April 2013; accepted 9 August 2013; published online 30 August 2013)

We report on the energetic locations of the defects created by oxygen in nanocrystalline Si and the relationship between defects and minority carrier lifetime. The energy of the defects was determined using capacitance-frequency measurements, and the minority carrier lifetime was determined using reverse recovery measurements. We show that oxygen increases deep defect densities, with the defect densities being measured between 0.35 eV and 0.55 eV below the conduction band. It is found that oxygen-induced defects can be reduced and lifetime increased by compensating with B. The minority carrier lifetime is found to be inversely proportional to defect density and the capture-cross section of holes is estimated to be $\sim 4 \times 10^{-17}$ cm^2. ©*2013 AIP Publishing LLC.*
[http://dx.doi.org/10.1063/1.4819204]

It is well known that increasing oxygen content in nanocrystalline Si:H (nano Si) leads to increasing defect density[1–3] and a loss of device performance,[2] with significant losses in quantum efficiency, current, voltage, and fill factor as oxygen content increases.[2] There is also some evidence that doping density in the materials increases as the oxygen content increases.[2] Oxygen is an ever-present impurity because most films and devices are grown using plasma-assisted chemical vapor deposition (PECVD) techniques and the plasma also decomposes oxygen molecules into O, which then readily gets into the Si lattice. In crystalline Si, O is known to introduce energy states at ~0.38 and 0.55 eV below the conduction band.[4] There has been some debate about whether oxygen in nano Si is in the amorphous matrix which surrounds nano Si, or within the grain itself. To resolve this issue, it is necessary to find out the energetic location of O centers in this material. In this paper, we report on such a measurement. We also measure minority carrier (hole) lifetime in nano Si samples and show that the lifetime is inversely related to the total defect density. From the relationship between lifetime and defect density, we can estimate the capture cross-section of O induced centers. We also show that compensation with B leads to passivation of O induced defects in this material.

The samples were p^+-n-n^+ devices, deposited on planar stainless steel foil, using PECVD from a mixture of silane and hydrogen.[5–7] To avoid cross-contamination, the middle n-layer was deposited in a reactor which was not contaminated with either P or B. Typical growth temperatures were ~250 °C, and growth pressure ~100 mT.[5] The crystallinity of the material was measured using Raman spectroscopy[8] and was kept approximately constant independent of thickness by using a graded hydrogen dilution profile.[9] The ratio of crystalline to amorphous phase was approximately 1:1. The oxygen content of the samples was varied by introducing ppm levels of oxygen from an 108 ppm oxygen diluted in helium mixture and controlling the flow rate of this mixture. Care was taken to maintain the same crystallinity in the devices when the flow of He was varied to introduce different levels of oxygen.

The energetic location of the defect density was measured using a capacitance-frequency (C-f) technique.[10] The samples were measured from 20 Hz to 300 kHz at 25 °C. The samples were also measured using the standard C-V techniques at 20 Hz and 100 °C so as to detect all defects in the midgap region. To accurately define the area, the devices were mesa-etched using a HNO_3:HF solution. In Fig. 1, we show the C-f curves for a typical device with and without intentional O doping. From such a curve, the defect density (in # /cm^3-eV) vs. trap energy in eV can be estimated using the following equations:[10]

$$N_t(E_\omega) = -\frac{U_d}{qw}\left(\frac{dC}{d\omega}\right)\frac{\omega}{kT}, \tag{1}$$

$$E_\omega = kT\ln\left(\frac{\upsilon_o}{\omega}\right). \tag{2}$$

In this equation, C is the capacitance, ω is the angular frequency, E_ω is the energy of the trap below conduction band, U_d is the built-in voltage at −1 V reverse bias, w is the depletion width, υ_o is the attempt to escape frequency from midgap states (assumed to be in the range 1×10^{12}/s),[1,11–13]

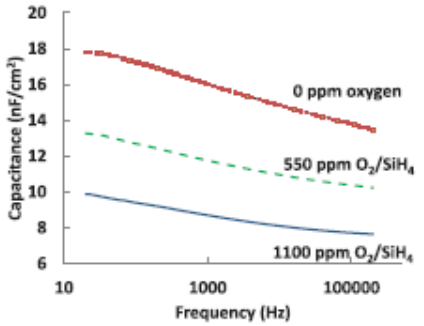

FIG. 1. Capacitance–frequency curves of various oxygen doped samples.

a)Author to whom correspondence should be addressed. Electronic mail: vdalal@iastate.edu

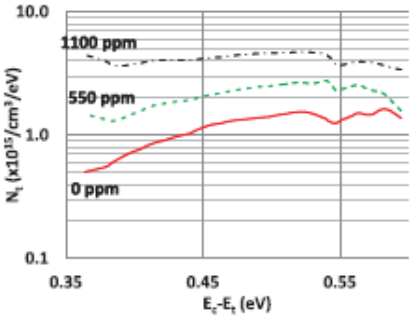

FIG. 2. Calculated density of defects in oxygen doped devices vs. energy below the conduction band for different oxygen/silane flow ratios.

and the other symbols have the usual meanings. Changes in υ_o by a factor of 10 will affect the energetic locations by ~0.06 eV. Note that we are dealing with emission from midgap states, and not tail states, where υ_o is estimated to be $\sim 1 \times 10^9$/s.[14]

The defect density of the traps vs. trap energy, deduced from the curve of Fig. 1, is shown in Fig. 2. There is a distinct peak at ~0.55 eV below the conduction band along with a distributed spectrum between 0.35 and 0.55 eV. It is useful to note that 0.35 and 0.55 eV correspond to the locations for traps due to oxygen incorporation in crystalline Si.[4] This correspondence indicates that at least some of the defects are being created within the nanocrystalline grain itself and not in the a-Si tissue surrounding it. As the oxygen content is increased, the entire defect curve shifts upwards with both the 0.55 eV peak value and value at 0.38 eV increasing.

The total defect plus very shallow dopant density (which does not show up in Fig. 2 because the highest frequency is not high enough to inhibit emission from the shallow doping levels) can also be estimated from measuring C-V curve at 20 Hz and 100 °C. At this temperature, almost all the states in the gap (except for the ones very close to the valence band) respond at the measurement frequency. (The states very near the valence band are not effective hole recombination centers because they are below the demarcation level for holes[15] and thus are not of interest). Such a C-V curve for a non-oxygenated sample is shown in Fig. 3, showing a total

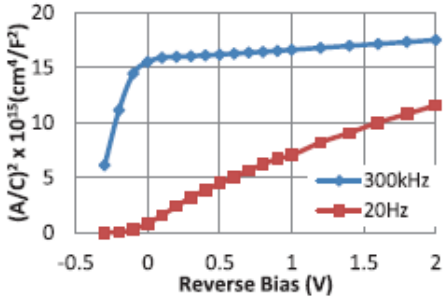

FIG. 3. Typical CV curve for a standard device at two frequencies and temperatures. The 20 Hz data were taken at 100 °C so that all defects and dopants can respond, whereas the high frequency curve taken at 25 °C only reveals shallow defects.

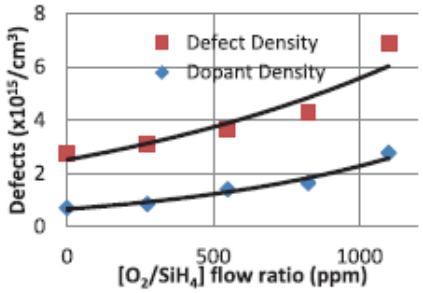

FIG. 4. Dopant and defect density values obtained from capacitance-voltage measurements versus oxygen flow during growth.

dopant plus defect density of $\sim 2.5 \times 10^{15}$/cm^3 in reasonable agreement with the integrated defect densities measured using C-f techniques. The figure also shows a C-V curve taken at 300 kHz and 25 °C, showing a much lower density of shallow states with energies within ~0.25–0.3 eV of the conduction band(primarily dopant states). The deep 0.35–0.55 eV states are the primary states responsible for recombination.

Next, we show, in Fig. 4, the dopant and defect density determined from C-V measurements for various values of oxygen doping. It is apparent that both defect and doping densities increase with oxygen flow.

We next calculated minority carrier (hole) lifetime by measuring the reverse recovery transient curve.[16,17] A typical reverse recovery curve is shown in Fig. 5, showing a distinct storage time T_{sd}. The storage time is related to lifetime by equation[16,17]

$$T_{sd} = \tau_p \times \left[erf^{-1}\left(\frac{I_f}{I_f + I_r}\right)\right]^2, \qquad (3)$$

where τ_p is the lifetime, I_f the forward current, and I_r the reverse current, and erf^{-1} is the inverse error function. The measured storage time can then be plotted vs. the inverse error function and the slope gives a value for the lifetime of holes in the material. Note that the reverse recovery technique estimates an average lifetime, and in general, states in the midgap contribute the greatest amount to recombination and hence primarily determine the lifetime.[15]

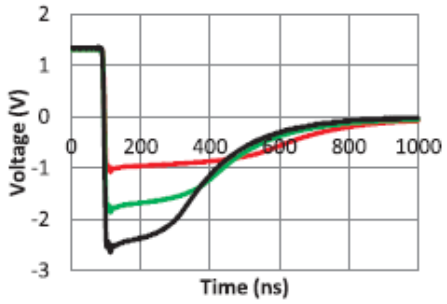

FIG. 5. Typical reverse recovery transient curves, showing a distinct storage time. The storage time decreases as the ratio of reverse to forward current increases.

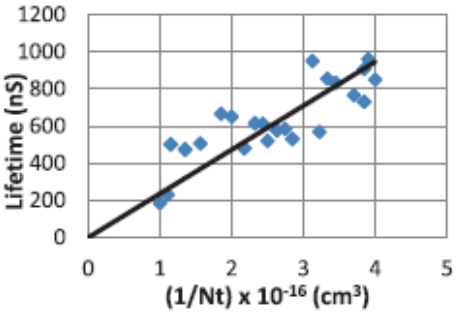

FIG. 6. Measured minority carrier lifetime vs. inverse of defect density (Nt). An approximate straight line indicates that holes recombine through the trap controlled recombination process.

A plot of the lifetime vs. inverse of the total defect density measured using C-V at 100 °C and 20 Hz is shown in Fig. 6. The defect density in each device is changed by changing the oxygen flow. There is an approximate linear relationship between the inverse of defect density and lifetime, indicating that recombination is through trap controlled statistics.[18] The slope of this curve gives a value for the capture cross-section for the traps (assumed equal for traps between 0.35 and 0.55 eV) of $\sim 4 \times 10^{-17}$ cm^2. Note that this estimate is for capture cross-section for *holes*; the *electron* capture cross-section can be much different from this value.[15] The attempt-to escape frequency ν_0 used earlier to calculate the demarcation level for capture of holes corresponds to the emission of *electrons* from the traps,[15] and the capture cross-section which corresponds to emission would be the *electron* capture cross-section which we cannot determine from our experiments.

It was shown by earlier authors[3] that B can compensate for the O induced defects. We deliberately introduced ppm levels of B into the material during growth using a mixture of tri-methyl Boron (TMB) diluted in hydrogen. In Fig. 7, we show how adding B reduces the defect density (measured using capacitance) which was created by adding 100 ppm of oxygen. Fig. 8 shows that addition of B increases minority carrier lifetime, thus showing the beneficial effects of B on the device performance.

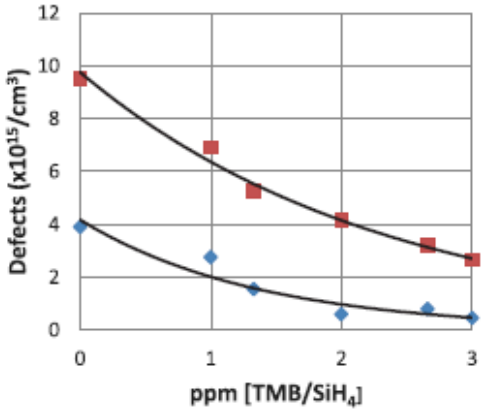

FIG. 7. Influence of ppm levels of B compensation on defect and dopant densities obtained from capacitance-voltage data. TMB stands for tri-methyl Boron.

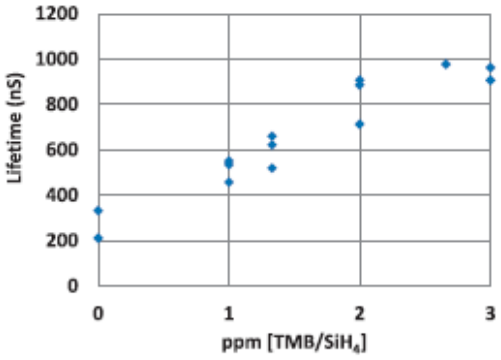

FIG. 8. Influence of adding B on minority carrier lifetime. Compensation by B increases the minority carrier lifetime.

In summary, we have shown that oxygen induces increase in midgap defects in nanocrystalline Si. The energetic positions of the defect levels are in agreement with the results found in crystalline Si. We also show that the minority carrier lifetime is inversely proportional to defect density. We further show that addition of B systematically reduces the defect density and increases minority carrier lifetime.

This work was partially supported by a grant from NSF and Iowa Power Fund. We thank Max Noack, Brian Modtland, Wai Leung, Spencer McAtee, and Andrew Gulstad for their technical help. The work was done at the Microelectronics Research Center of Iowa State University.

[1]P. G. Hugger, J. D. Cohen, B. Yan, G. Yue, J. Yang, and S. Guha, Appl. Phys. Lett. **97**, 252103 (2010).
[2]T. Kilper, W. Beyer, G. Brauer, T. Bronger, R. Carius, M. van den Donker, D. Hrunski, A. Lambertz, T. Merdzhanova, and A. Muck, J. Appl. Phys. **105**, 074509 (2009).
[3]V. Dalal and P. Sharma, Appl. Phys. Lett. **86**, 103510 (2005).
[4]See, for example, S. Sze, *Physics of Semiconductors* (Wiley, New York, 2007).
[5]V. L. Dalal, J. Graves, and J. Leih, Appl. Phys. Lett. **85**, 1413 (2004).
[6]A. Shah, J. Meier, E. Vallat-Sauvain, N. Wyrsch, U. Kroll, C. Droz, and U. Graf, Sol. Energy Mater. Solar Cells **78**, 469 (2003).
[7]J. Müller, O. Kluth, S. Wieder, H. Siekmann, G. Schöpe, W. Reetz, O. Vetterl, D. Lundszien, A. Lambertz, F. Finger, B. Rech, and H. Wagner, Sol. Energy Mater. Solar Cells **66**, 275 (2001).
[8]C. Smit, R. A. C. C. M. van Swaaij, H. Donker, A. M. H. N. Petit, W. M. M. Kessels, and M. C. M. van de Sanden, J. Appl. Phys. **94**, 3582 (2003).
[9]B. J. Yan, G. Z. Yue, J. Yang, and S. Guha, Appl. Phys. Lett. **85**, 1955 (2004).
[10]T. Walter, R. Herberholz, C. Muller, and H. Schock, J. Appl. Phys. **80**, 4411 (1996).
[11]S. Reynolds, J. Optoelectron. Adv. Mater. **11**, 1086 (2009).
[12]A. Fejfar, N. Beck, H. Stuchlikova, N. Wyrsch, P. Torres, J. Meier, A. Shah, and J. Kocka, J. Non-Cryst. Solids **227**, 1006 (1998).
[13]R. B. Wehrspohn, M. J. Powell, S. C. Dean, I. D. French, and P. I. Cabaroccas, Appl. Phys. Lett. **77**, 750 (2000).
[14]T. Dylla, F. Finger, and E. A. Schiff, Appl. Phys. Lett. **87**, 032103 (2005).
[15]J. G. Simmons and P. W. Taylor, Phys. Rev. B **4**, 502 (1971).
[16]See, for example, B. Streetman and S. Banerjee, *Solid State Electronic Devices*, 6th. ed (Prentice Hall, New York, 2005), Chap. 5.
[17]S. Saripalli, P. Reusswig, P. Sharma, and V. L. Dalal, J. Non-Cryst. Solids **354**, 2426–2429 (2008).
[18]See, for example, R. Pierret, *Advanced Semiconductor Fundamentals*, 2nd ed. (Prentice Hall, Englewood Cliffs, NJ, 2003), Chap. 5.

Defects and Doping in Nanocrystalline Silicon-Germanium Devices

This work was published in MRS proceedings 2014

Siva Konduri, Watson Mulder and Vikram L. Dalal

Department of Electrical and Computer Engineering, Iowa State University, Ames, Iowa

ABSTRACT

Nanocrystalline Silicon-Germanium (Si,Ge) is a potentially useful material for photovoltaic devices and photo-detectors. Its bandgap can be controlled across the entire bandgap region from that of Si to that of Ge by changing the alloy composition during growth. In this work, we study the fabrication and electronic properties of nanocrystalline devices grown using PECVD techniques. We discovered that upon adding Ge to Si during growth, the intrinsic layer changes from n-type to p-type. We can change it back to n-type by using ppm levels of phosphorus, and make reasonable quality devices when phosphine gas was added to the deposition mix. We also measured the defect density spectrum using capacitance frequency techniques, and find that defect density decreases systematically as more phosphine is added to the gas phase. We also find that the ratio of Germanium to Silicon in the solid phase is higher than the ratio in the gas phase.

INTRODUCTION

Nanocrystalline Si (nc-Si) is an important and useful material for solar cells and photo-detectors. Significant progress has been made in the solar conversion of efficiency of nc-Si with efficiencies exceeding 10% in single junction cells, and exceeding 15% in multiple junction cells[1-5]. However, there has been little progress in increasing the efficiencies of

nanocrystalline (Si,Ge) alloys[6-10], which can potentially achieve high quantum efficiencies in the infrared range out to 0.68 eV i.e. the bandgap of crystalline Ge. It is usually found that as one adds Ge to Si, the device performance becomes worse, and it has been speculated that this decrease in performance is due to additional Ge-associated defects in the material [10, 11]. In this paper, we show that addition of Ge to Si leads to significant increases in defect density, and may even make the intrinsic n layer material to p-type. We also show that addition of ppm levels of phosphorus, using phosphine, to the intrinsic layer reduces the defect density and makes the material n type again, and allows one to achieve reasonable devices with quantum efficiencies extending further into the infrared regions.

EXPERIMENTS

The materials and devices were fabricated using PECVD techniques using a VHF plasma at ~47 MHz. The substrate temperature was in the range of ~250 °C and pressure was ~ 100mT. The precursor gases were hydrogen, silane and 10% germane diluted in hydrogen. Varying levels of Ge:Si could be produced by varying the ratio of germane to silane flow ratio. Ppm levels of dopants such as phosphorus and boron could be introduced in the base (intrinsic) layer using dopants such as phosphine and diborane diluted in hydrogen. The devices were standard p+in+ devices, deposited on pre-cleaned stainless steel substrates with the i layer generally being n type for nc-Si. ITO dots are deposited as top contacts and contact area is 0.12cm2. SiGe is used as p-layer to avoid kinks in bandgap and a smooth transition at p-i interface and Ge concentration in p-layer is around 20%. The basic device structure of nc-SiGe:H solar cell is shown in Fig. 1. Thickness of i-layer is about 0.70 μm.

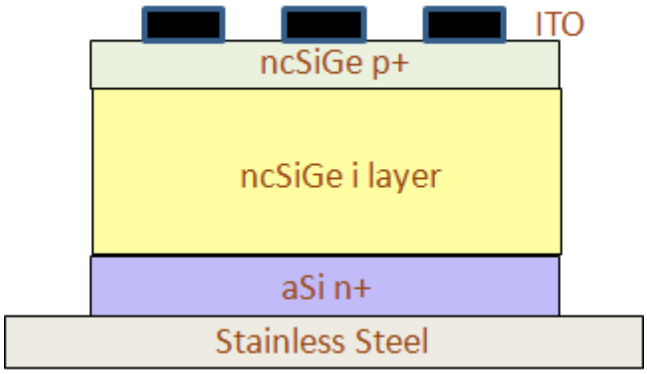

Figure 1. Typical device structure of nc-SiGe:H solar cell

For measuring defect densities, we used the capacitance-frequency techniques described previously [12]. Device quantum efficiency (QE) was also measured using standard techniques. The ratio of Ge:Si in the solid phase was determined using energy dispersive x-ray spectroscopy.

RESULTS

In Fig. 2, we show the ratio of Ge:Si in the solid phase for various germane:silane flow rates. It is clear from this figure that much more Ge is incorporated in the solid phase as than is present in the gas phase.

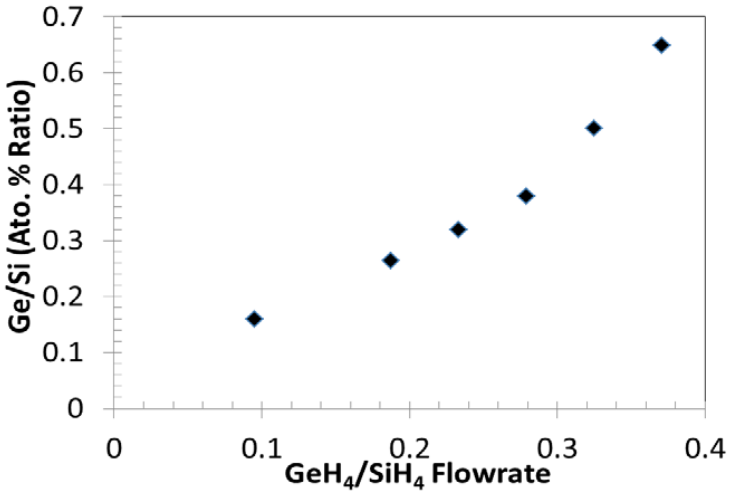

Figure 2. Germanium content for different gas flows in nc-SiGe:H devices

In Fig. 3a, we show the illuminated I-V curves for samples prepared using varying germane:silane ratios. A surprising result is that the short-circuit current actually decreases as the germane content in the gas phase increases. This is in spite of the fact that the germane:silane ratio in the solid phase is increasing, thereby implying a smaller bandgap material for higher germane flows. The explanation for this behavior is provided by studying quantum efficiency data, shown in Fig. 3b. It is clear from the QE data that there is a drastic reduction in QE for short wavelengths when significant amounts of germane is added to the input gas mixture. This can be ascribed to poor collection of electrons being generated near the p-n interface by light of shorter wavelengths, i.e. to a drastic reduction in electron diffusion length. This could be a result of the n-type intrinsic layer changing to a p-type, presumably due to Ge defects absorbing electrons from the oxygen induced donor states [13]. Indeed, there appears to be a significant increase in defect density when Ge content increases. See Fig. 4 for data on defect density vs. energy for varying German:Silane flow rates.

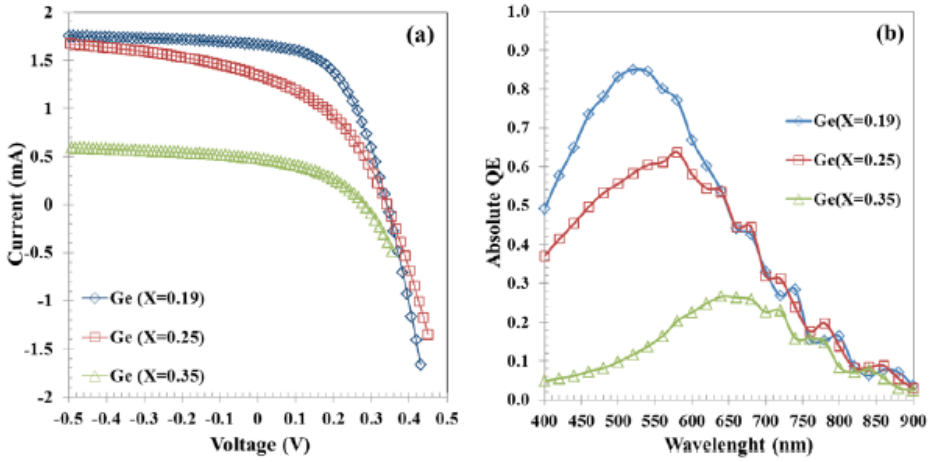

Figure 3. (a) IV curves and (b) Absolute QE vs. Wavelength for nc-SiGe:H solar cells with varying Ge content

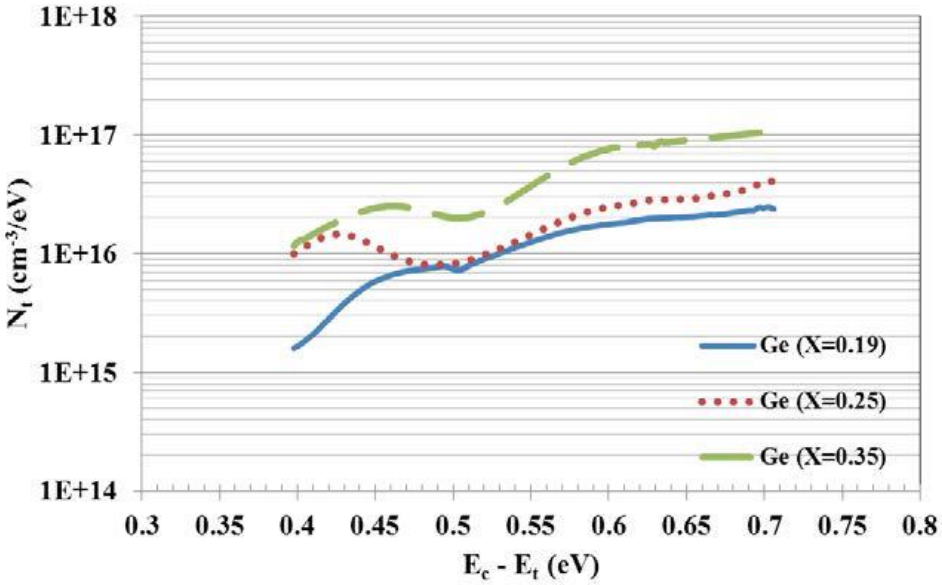

Figure 4. Calculated defect density vs. energy below the conduction band for varying Ge content

To overcome the deleterious effects of additional Ge on both defect density and QE, we tried to compensate for the apparent p-type doping by adding ppm levels of PH3 to the gas mixture. The results for I-V curve are shown in Fig. 5a for various values of PH3 for a fixed germane:silane ratio of in the gas phase. Clearly, adding PH3 significantly improves the short-circuit current in the solar cell. The corresponding QE curves are shown in Fig. 5b, and they clearly show an improvement in QE at short wavelengths, compared to the QE curves shown in Fig. 3, thus showing that the poor electron collection efficiency for photons which are absorbed near the p-intrinsic layer interface has been overcome. The corresponding change in total defect density as a function of PH3 flow is shown in Fig.6, thus confirming that addition of ppm levels of PH3 serves to reduce the defect density in nanocrystalline (Si,Ge) intrinsic layers, probably by compensating the defects caused by Ge addition.

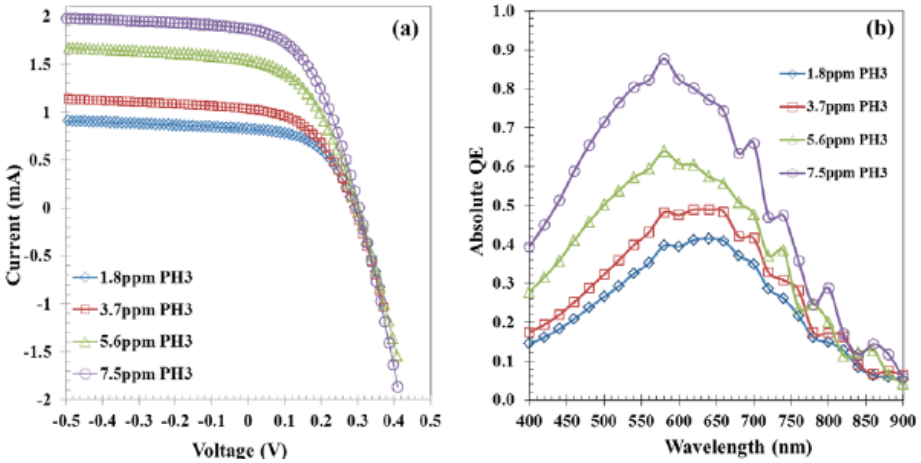

Figure 5. (a) IV curves and (b) Absolute QE vs. Wavelength for nc-SiGe:H solar cells with (XGe~0.35) for varying PH3 flow rates

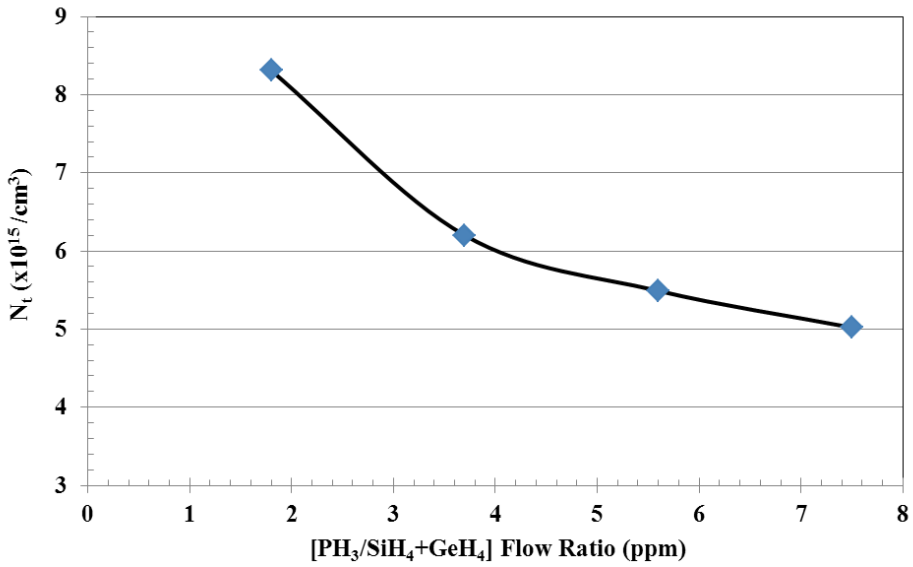

Figure 6. Total defect density as a function of PH3 flow rate

I-V curves for the devices prepared using varying ratios of germane:silane flow along with optimum ppm levels of PH_3 are plotted in Fig.7a, which clearly shows that increasing Ge content leads to higher short-circuit currents but approximately the same open-circuit voltage. In general, Voc depends on quality of i-layer, type of p-layer and transition layers. Further experiments are being conducted to examine the relationship of Voc with Ge content. The

corresponding QE data in Fig. 7b shows that increasing Ge content shifts the curves to longer wavelengths, as expected.

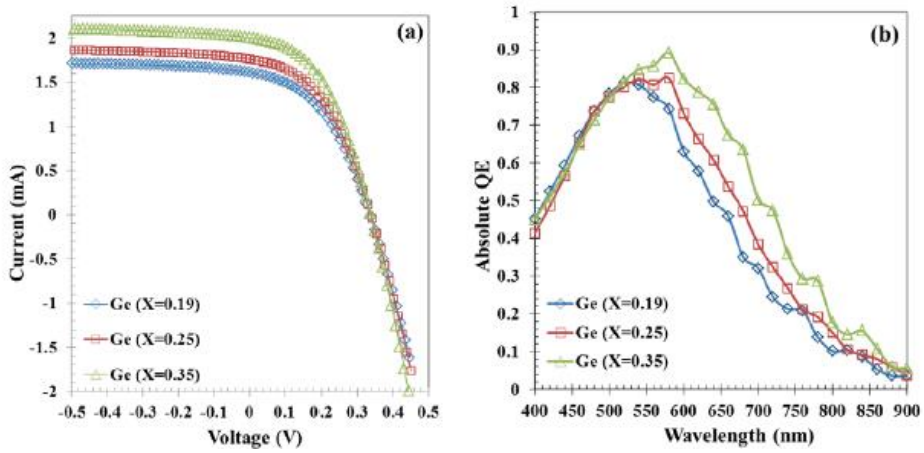

Figure 7. (a) IV curves and (b) Absolute QE vs. Wavelength for nc-SiGe:H solar cells with varying Ge content with optimum PH3 flow (i-layer Thickness ~ 0.7μm)

CONCLUSIONS

In conclusion, we have shown that the defect density in the intrinsic layer of nanocrystalline p-i-n solar cells material increases significantly as Ge content increases. It appears that adding Ge changes the doping type of the intrinsic layer form n-type to p-type. This shift leads to a drastic reduction in quantum efficiency for short wavelength photons at higher Ge concentrations. The defect density can be reduced, and the p-type behavior changed back to n-type by adding ppm levels of PH3 to the gas phase. The results show that when appropriate compensation by Phosphorus has been achieved, the quantum efficiency for solar cells extends further out towards longer wavelengths as the Ge content of the solar cell intrinsic layer increases, as expected, resulting in larger currents. This is an important result which shows that nanocrystalline (Si,Ge) cells can be used to improve the efficiency of tandem junction solar cells, as also the infrared response when these materials are used as photo-detectors.

ACKNOWLEDGMENTS

It is a pleasure to acknowledge the technical help of Andrew Gulstad and Max Noack. This work was partially supported by a grant from NSF.

REFERENCES

1. J. Meier, R. Flückiger, H. Keppner and A. Shah, Applied Physics Letters, **65**, 860-862 (1994)

2. A. Shah, J. Meier, E. Vallat-Sauvain, C. Droz, U. Kroll, N. Wyrsch, J. Guillet and U. Graf, Thin Solid Films, **403–404**, 179-187, (2002)

3. A. Shah, J. Meier, E. Vallat-Sauvain, N. Wyrsch, U. Kroll, C. Droz and U. Graf, Solar Energy Materials and Solar Cells, **78**, 469-491, (2003)

4. V. Dalal, J. Leib, K. Muthukrisnan, D. Stieler, and M. Noack, 2005 IEEE Photovoltaic Specialists Conference, 1448- 1451, (2005)

5. G. Yue, B. Yan, L. Sivec, T. Su, Y. Zhou, J. Yang and S. Guha, 2012 MRS Proceedings, **1426**, 33-38, (2012)

6. M. Isomura, K. Nakahata, M. Shima, S. Taira, K. Wakisaka, M. Tanaka and S. Kiyama, Solar Energy Materials and Solar Cells, **74** (1–4), 519-524 (2002)

7. J. K.Rath, F.D. Tichelaar and R. E.I Schropp, Solar energy materials and solar cells, **74,** 553-560 (2002)

8. S. Saripalli and V. Dalal, EIT 2008 IEEE International Conference Proceedings, 414-418, (2008)

9. T. Matsui, M. Kondo, K. Ogata, T. Ozawa and M. Isomura, Applied Physics Letters, **89**, 142115, (2006)

10. T. Matsui, K. Ogata, C.W. Chang, M. Isomura and M. Kondo, Journal of Non-Crystalline Solids, **354** (19–25), 2468-2471, (2008)

11. T. Matsui, C.W. Chang, T. Takada, M. Isomura, H. Fujiwara and M. Kondo, Solar Energy Materials and Solar Cells, **93**, 1100-1102, (2009)

12. K. Shantan, K. Siva and V. Dalal, Applied Physics Letters, **103**, 093506 (2013)

13. T. Matsui, C.W. Chang, K. Mizuno, Y. Takeuchi and M. Kondo, Japanese Journal of Applied Physics, **51,** 091302, (2012)

APPENDIX B

Defect Density Profile of Perovskite Solar Cells

Modified from paper submitted to Applied Physics Letters 2014 [11]

Mehran Samiee,[1] Siva Konduri,[1] Balaji Ganapathy,[2] Ranjith Kottokkaran,[2] Hisham A. Abbas,[1] Andrew Kitahara,[3] Pranav Joshi,[1] Liang Zhang,[1] Max Noack,[2] and Vikram Dalal,[1]
[1]Dept. of Electrical and Computer Engineering, Iowa State University, Ames, IA 50011
[2]Microelectronics Research Center, Iowa State University, Ames, Iowa 50011, USA
[3]Dept. of Materials Science and Engineering, Iowa State University, Ames, Iowa 50011, USA

ABSTRACT

We report on measurement of dielectric constant, mid-gap defect density, Urbach energy of tail states in $CH_3NH_3PbI_XCl_{1-X}$ perovskite solar cells. Midgap defect densities were estimated by measuring capacitance vs. frequency at different temperatures and show two peaks, one at 0.66 eV below the conduction band and one at 0.24 eV below the conduction band. The attempt to escape frequency is in the range of $2x10^{11}$/s. Quantum efficiency data indicate a bandgap of 1.58 eV. Urbach energies of valence and conduction band are estimated to be ~16 and ~18 meV. Measurement of saturation capacitance indicates that the relative dielectric constant is ~18.

INTRODUCTION

In this section, Perovskite solar cells are briefly explained followed by detailed discussion on their defect density. Perovskite solar cells are exciting technology with conversion efficiencies exceeding 19% [1–6]. It is shown that, this material is poly-crystalline, high absorption coefficients with relatively small exciton binding energy [7] and diffusion lengths approaching 1 μm for both carriers [8]. For better understanding of device physics of Perovskite solar cells, it is important to study the defect density and spatial distribution of traps.

EXPERIMENTAL DETAILS

A typical Perovskite based solar cell device structure is shown in Figure 1. The n-i-p structure consists of TiO2/perovskite/p-heterojunction/gold structure. Compact layer of TiO_2 is deposited on a FTO (Fluorine-doped Tin Oxide) substrate, followed by deposition of Lead Iodide (PbI_2) and to form Perovksite, these PbI_2 films were annealed in Methyl Ammonium Iodide (CH_3NH_3I) vapor at 150 °C in N_2 atmosphere [9]. The hole-transporting layer of P3HT (Poly-3-Hexyl Thiophene) was formed using spincoating, and finally 80 nm of Gold contacts were thermally evaporated.

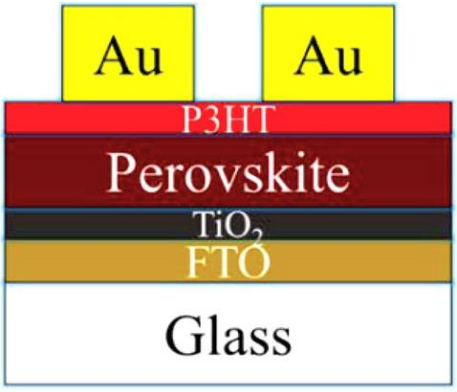

Figure 1. Device structure of Perovskite based solar cell

RESULTS

JV characteristics and EQE curve are shown in Figure 2 with a power conversion efficiency of around 15% and Jsc of about 22mA/cm^2. The thickness of the i-layer is 460 nm and the bandgap of the material is 1.6 eV. Even with very high efficiencies and inherent carrier properties, Perovskite lags in stability. The main focus should be degradation studies as Perovskite is sensitive to moisture [10]. It is very important to study about the fundamental defects in Perovksite for better understating of device physics.

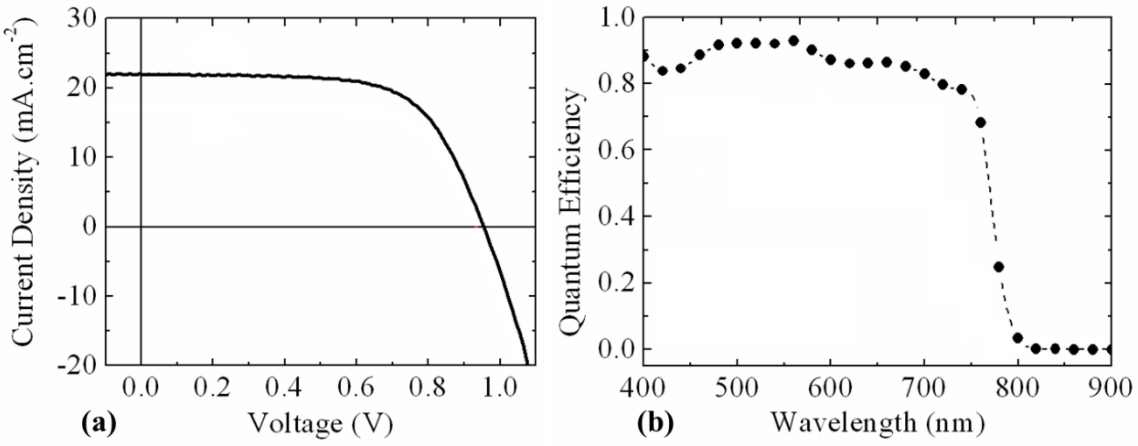

Figure 2. (a) Illuminated JV curves measured using solar simulator and (b) QE vs. Wavelength for Pb-halide based Perovskite solar cells

In Figure 3, the experimental data for CF and differential capacitance at various temperatures is plotted. In this material also, capacitance shift is observed at two distinctive bands. As the Perovskite is a higher bandgap material, temperature >300K is required to reach the midgap states. The inset in the Figure 3 exhibits that existence of secondary peak related to a trap level in addition to midgap defect state.

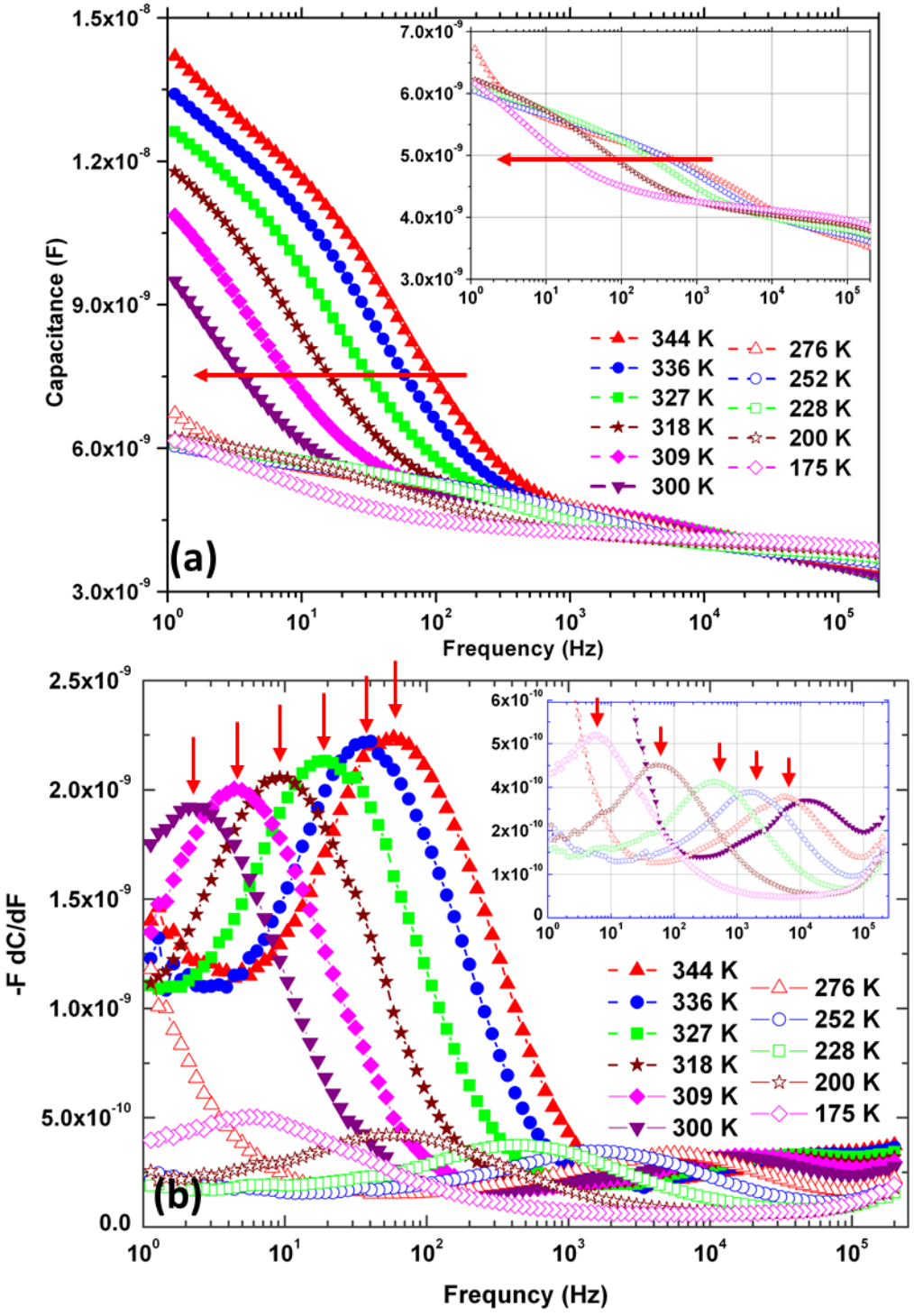

Figure 3. (a) CF at various Temperatures for Perovksite based solar cell. The red arrows indicate the shift in capacitance. (b) Differential capacitance curves. Arrows indicate emission peaks.

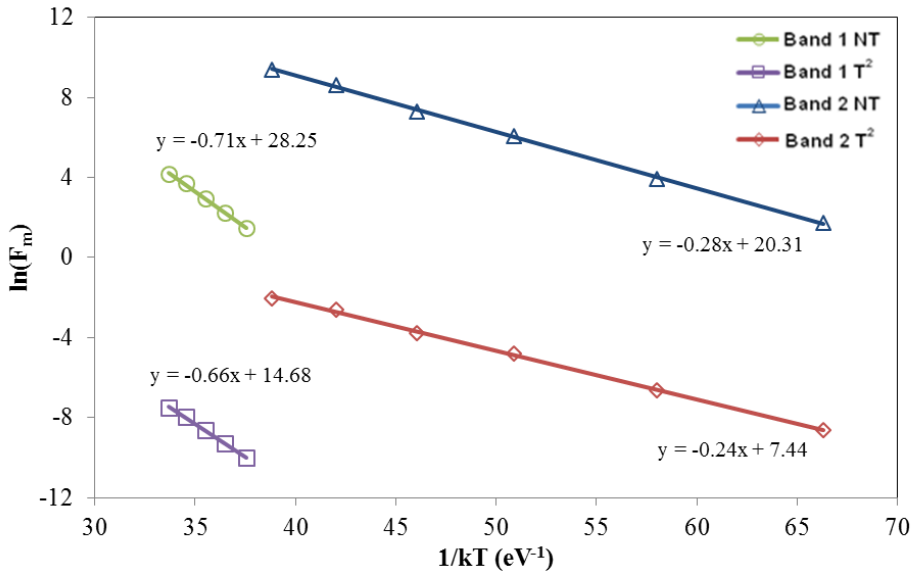

Figure 4. Arrhenius plot of the differential capacitance peak frequencies vs. 1/kT for Perovkite solar cell

The Arrhenius plot deduced from the differential capacitance curve of Figure 3 is shown in Figure 4, and the slope indicates trap energy levels at ~0.66 eV and ~0.24 eV below the conduction band. The ATE calculated from the intercept of dominant midgap trap is ~$2x10^{11}$Hz. The defect density plot using CF data at room temperature (300K) is shown in Figure 5 and a major peak corresponding to midlevel trap is observed at around 0.65 eV below conduction band, with a peak value of $3x10^{16}$ $cm^{-3}eV^{-1}$. The defect density curve on a linear plot shown an excellent Gaussian fit and centered at ~0.65 eV, which is in agreement with the activation energy found in Arrhenius plot. Table 1 summarizes the averaged parameters derived from CFT data.

Table 1. Summary of the averaged parameters from CFT data of Perovskite solar cell

Activation Energy, E_a	260 meV	680 meV
ATE, ν_0	$6x10^8$ Hz	$2\ x10^{11}$ Hz
Pre-factor, Υ	$6.7x10^3$ Hz K^{-2}	$2.4x10^6$ Hz K^{-2}
Capture cross-section, σ_n^*	$6x10^{-18}$ cm^2	$2\ x10^{-14}$ cm^2

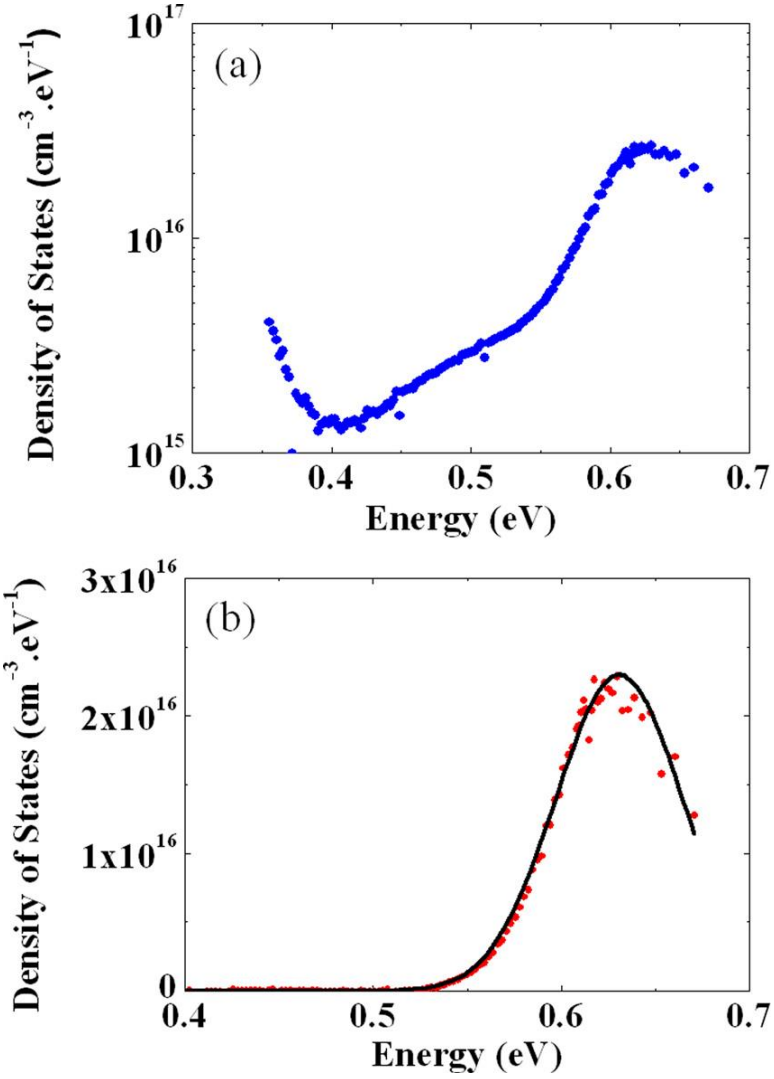

Figure 5 (a) Calculated defect density from CF data at 300K for a Perovkite solar cell and (b) Fitted Gaussian curve for the same data on a linear plot

From the differential capacitance curves (Figure 3b) and calculated ATE value from Arrhenius plot, defect density profile is estimated and shown in Figure 6. Two distinctive trap energy levels are observed as expected from the capacitance steps. Initial peak around 350 meV with density of $6x10^{15}$ cm^{-3} eV^{-1} followed by dominant midgap peak around 650 meV with a density of $2.0x10^{16}$ cm^{-3} eV^{-1} which is a Gaussian distribution of deep defects around the midgap. To get a good overlap in the defect profile, temperature independent ATE is used

for midgap defect state and temperature dependent pre-factor is used for the secondary peak. This result concludes that the emission rate of the two trap levels is different and the carrier response from trap level close to the band edge is more temperature driven. Further in-depth study is required to comprehend the different carrier response from the trap levels.

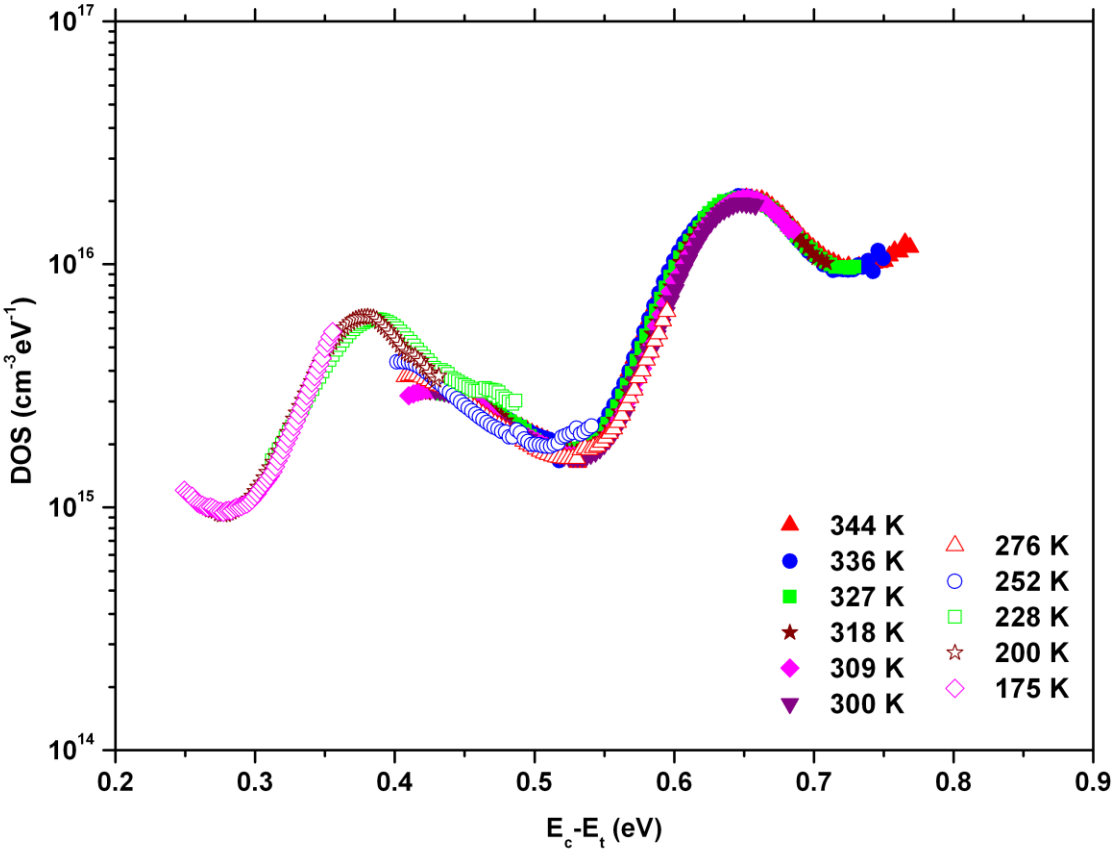

Figure 6 Estimated defect density profile of Perovskite solar cell using CFT data

REFERENCES

1. M. Liu, M. B. Johnston, and H. J. Snaith, “Efficient planar heterojunction perovskite solar cells by vapor deposition” Nature 501, 395 (2013).
2. J. Burschka, N. Pellet, S.-J. Moon, R. Humphry-Baker, P. Gao, M. K. Nazeeruddin, and M. Gratzel, “Sequential deposition as a route to high-performance perovskite-sensitized solar cells” Nature 499, 316 (2013).

3. V. Gonzalez-Pedro, E. J. Juarez-Perez, W. Arsyad, E. M. Barea, F.Fabregat-Santiago, I. Mora-Sero, and J. Bisquert, "General Working Principles of $CH_3NH_3PbX_3$ Perovskite Solar Cells" Nano Letters. 14, 888–893 (2014).
4. G. E. Eperon, V. M. Burlakov, A. Goriely, and H. J. Snaith, "Neutral Color Semitransparent Microstructured Perovskite Solar Cells" ACS Nano 8, 591–598 (2014).
5. J. Im, I. Jang, N. Pellet, M. Gratzel, and N. Park, "Growth of $CH_3NH_3PbI_3$ cuboids with controlled size for high-efficiency perovskite solar cells," Nature Nanotechnology 9, 927–932 (2014)
6. H. Zhou, Q. Chen, G. Li, S. Luo, T. Song, H. Duan, Z. Hong, J. You, Y. Liu, Y. Yang, "Interface engineering of highly efficient perovskite solar cells", Science 345, 542 (2014)
7. V. D'Innocenzo, G. Grancini, M. J. P. Alcocer, A. R. S. Kandada, S. D. Stranks, M. M. Lee, G. Lanzani, H. J. Snaith, and A. Petrozza, "Excitons versus free charges in organo-lead tri-halide perovskites" Nature Communications 5, 3586 (2014).
8. S. D. Stranks, G. E. Eperon, G. Grancini, C. Menelaou, M. J. P. Alcocer, T. Leijtens, L. M. Herz, A. Petrozza, and H. J. Snaith, "Electron-Hole Diffusion Lengths Exceeding 1 Micrometer in an Organometal Trihalide Perovskite Absorber" Science 342, 341–344 (2013).
9. Q. Chen, H. Zhou, Z. Hong, S. Luo, H. Duan, H. Wang, Y. Liu, G. Li, and Y. Yang, "Planar Heterojunction Perovskite Solar Cells via Vapor-Assisted Solution Process" Journal of American Chemical Society 136, 622–625 (2014)
10. G. Niu, W. Li, F. Meng, L. Wang, H. Dong and Y. Qiu, "Study on the stability of $CH_3NH_3PbI_3$ films and the effect of post-modification by aluminum oxide in all-solid-state hybrid solar cells" Journal of Material Chemistry A, 2, 705–710 (2014)
11. M. Samiee, S. Konduri, B. Ganapathy, R. Kottokkaran, H. A. Abbas, A. Kitahara, P. Joshi, L. Zhang, M. Noack and V. Dalal, "Defect density and dielectric constant in perovskite solar cells" Applied Physics Letters, 105, 153502 (2014)